Acknowledgements

I took this opportunity to express my deepest appreciation and gratitude to my advisor, Prof. T. C. Ward, for his support and encouragement. It has been truly memorable and educative being a member of his research group. I owe special thanks to my committee, Prof. G. L. Wilkes, Prof. J. E. Wightman, Prof. J. C. Schug, and Prof. H. Marand for their guidance and suggestions. I also owe sincere thanks to Prof. A. R. Shultz for his several valuable ideas and discussion that has been truly learning experience. I should also express appreciation to Prof. J. G. Dillard for directing CASS, from which I have financially supported and valuable chances to meet many people. I thank him for writing me several letters that cheer me to work more pleasantly.

I acknowledge Mr. Steve McCartney, Mr. Frank Cromer, and Dr. Qing Ji for their technical assistance for my research. Special thanks go to secretaries in CASS (Ms. Linda Haney, Ms. Katy Hatfield, Ms. Kim Mills, and Ms. Tammy Hiner) and in NSF center (Ms. Joyce Moser, Ms. Esther Brann, and Ms. Millie) for their help over the years.

I wish to thank all of PolyPkem group (both present and past) for their cooperative friendship. It has been really enjoyable and memorable to work together. I specially appreciate Dr. Mark Muggli not only for scientific discussions we had but also for his friendship. I also want to express appreciation to his family for their hospitality while I have been alone in Blacksburg. Kermit Kwan and Dave porter should not be the second to get my gratitude for their help on my research as well as friendship. All members in our group must be appreciated for helping me to survive and to enjoy in a foreign country. I wish them all to accomplish their goals successfully.

Friendship developed with Korean senior fellows, Dr. Tae Ho Yoon, Dr. Sanghun Lee, and Dr. Taigyoo Park as well as junior fellows, Dr. Yong Joon Lee, and Mr. Seungman Sohn has been another memorable part of my life in Virginia Tech. I thank them for having a great time and valuable discussions that we had professionally and socially.

I want to express sincere appreciation to my family for their affection, patience, support and encouragement for years. I appreciate my sister, Oh Hee Kwon Cho, and brother, Osang Kwon, for their encouragement and support. Appropriate words could not be found to express appreciation to my wife, Dr. Hyesuk Lee Kwon and my precious twin daughters, Jennie Kwon and Annie Kwon for their endless patience, support, and encouragement. I thank from the bottom of my heart my parents, Mr. Youngcheol Kwon and Mrs. Byungcheol Han, as well as parents-in-law, Mr. Sunho Lee and Mrs. Bongsun Kim. This work is dedicated to my beloved parents.

TABLE OF CONTENTS

LIST OF FIGURES

LIST OF TABLES

Chapter 1: INTRODUCTION

Epoxy thermosets have been widely used as high performance adhesives and matrix resins for composites due to their outstanding mechanical and thermal properties. These properties include high modulus and tensile strength, high glass transition temperature, high thermal stability, and moisture resistance[1]. When cured, epoxy resins form a highly crosslinked three-dimensional infinite network whose microstructure leads to desirable engineering properties. However, the highly crosslinked microstructure also produces a brittle neat epoxy resin. This undesirable property restricts epoxy thermosets from applications requiring high impact and fracture strengths. One of the most successful and widely used methods to improve the fracture toughness of thermoset materials is to incorporate a rubber into the glassy epoxy matrix.[2] The rubber used for this purpose is generally a butadiene-acrylonitrile copolymer with reactive functional end groups such as carboxyl, amine or epoxy, i.e., CTBN, ATBN, or ETBN[3,4]. The functional groups of the rubber then form chemical bonds with the epoxy matrix to provide interfacial bonds between the matrix and the dispersed phase. The initial rubber composition should not exceed about 20 % by weight to be most effective[3-5]. This assures an increase in toughness without sacrificing the good properties of the epoxy resin.

The liquid reactive rubber is chosen to be initially miscible with the epoxy resin and the curing agent. As polymerization starts at a designed temperature or along a temperature ramp, polymer chains grow and the weight average molecular weight of the epoxy approaches infinity as the reaction approaches the gel point. The rubber components become incompatible with the epoxy resin at a certain degree of polymerization. This is due to an increase in free energy of mixing resulting from the decrease in the absolute value of the configurational entropy change. Therefore, phase separation from an initial homogeneous solution takes place to form a rubber-rich dispersed particle phase and an epoxy-rich matrix phase. This phase separation occurs at the degree of polymerization that can be experimentally observed as a cloud point. The phase separation process is completed well before gelation or vitrification due to kinetic limitations in most rubber-modified epoxy systems. The morphology of the rubber phase developed by this process depends on the relative rates of polymerization and of phase separation, which are controlled by the initial composition and also the cure temperature. The mechanical and physical properties of the final product depend on the crosslink density, rubber compositions and glass transition temperatures in both dispersed and continuous phases, and the volume fraction, as well as the number and size, of the dispersed particle phase. Cure conditions for a single formulation can vary all of these parameters.

It is desirable to predict and regulate how the morphology is developed at different cure temperatures in order to model how the resulting morphological parameters affect the fracture toughness of the modified thermoset. Understanding the evolution of rubber rich particles by a phase separation process is crucially important in the control of morphology

and thus in elucidating the toughening mechanism[3-7]. Williams and coworkers proposed a theoretical model based on the Flory-Huggins equation along with constitutive equations for polymerization and phase-separation rates to predict composition, volume fraction, number density, and the average size of dispersed particles[8,9]. This model only works for phase separation in the metastable region. These researchers proposed that the rubber-modified epoxy thermosets employed in their model evolved the rubber-rich particles by a nucleation and growth mechanism with the initial rubber composition being less than the critical composition. On the other hand, Yamanaka et al. suggested that phase separation proceeds via spinodal decomposition and that the spherical domain structure results from the fixation of the morphology at a late stage of spinodal decomposition[10]. Careful examination and enhancement of these models will provide a guide to producing desirable morphology as well as theoretical justification of experimentally observed facts.

This dissertation is focused on analyzing quantitatively the effects of the morphological parameters on toughness of the rubber-modified epoxy thermoset. Because these parameters along with crosslink density are varied with cure temperature, it is difficult to control them independently to determine which is the most controlling factor of the toughness improvement. Furthermore, direct use of particle size distribution measured from TEM micrographs turned out to be unreliable due to inherent experimental error and uncertainties in the methodology[11,12]. Therefore, this study involved making an appropriate model to predict the morphological parameters of the epoxy system to be studied based on Williams' work and developing a methodology to measure morphological parameters. Comparison of the predicted morphology with experimental observation will confirm a proposed mechanism for the formation of phase separated particles. Furthermore, measurements of fracture toughness for the samples of different morphologies produced by systematic variation of cure temperature will allow one to correlate each morphological parameter to the fracture toughness.

It was of interest to study a diglycidyl ether of bisphenol A (DGEBA) type of epoxy cured with stoichiometric amount of diaminodiphenyl sulfone (DDS) in the presence of ETBN rubber. Since this system has been extensively studied for a long time by other researchers, considerable amounts of useful data are available. Thus it is easy to compare our results to others in some respects.

Chapter 2 provides literature reviews related to this study. Chapter 3 discusses the methodology development to quantitatively describe the morphology of spherical particles dispersed in a matrix. It is explained in Chapter 4 how a model for phase separation during the step-growth polymerization works with an example. In Chapter 5, the reaction kinetics as well as construction of a time-temperature-transformation diagram of this system is presented. Chapter 6 deals with the theoretical predictions for DGEBA/DDS/ETBN system and compares the final morphologies predicted by the model with those measured experimentally. Chapter 7 shows how the fracture toughness is influenced by the morphological parameters. Finally, Chapter 8 makes overall conclusions of this study and suggests future work.

1.1. REFERENCES

1. "**Epoxy Resin Chemistry and Technology**", C. A. May, Y. Tanaka, Eds.; Marcel Dekker, New York, (1973)**.**
2. J. N. Sultan, F. J. McGarry, *J. Polym. Eng. Sci.*, **13**, 29 (1973).
3. S. Kunz-Douglass, W. R. Beaumont, M. F. Ashby, *J. Mater. Sci.*, **15**, 1109 (1980).
4. E. Butta, G. Levita, A. Marchetti, A. Lazzeri, *Polym. Eng. Sci.*, **26**, 63, (1986).
5. W. D. Bascom, D. L. Hunston, In ***Rubber-Toughened Plastics***; Riew, C. K., Eds.; Advances in Chemistry 222; American Chemical Society: Washington D.C., 1989; p 135.
6. a) A. J. Kinloch, In ***Rubber-Toughened Plastics***; Riew, C. K., Eds.; Advances in Chemistry 222; American Chemical Society: Washington D.C., 1989; p 68 .

   b) A. J. Kinloch, D. L. Hunston, *J. Mat. Sci. Lett*., **6**, 131 (1987).
7. S. C. Kunz, J. A. Sayre, R. A. Assink, *Polymer*, **23**, 1897 (1982).
8. R. J. J. Williams, J. Borrajo, H. E. Adabbo, A. J. Rojas, In ***Rubber-Modified Thermoset Resins***; Riew, C. K.; Gillham, J. K., Eds.; Advances in Chemistry 208; American Chemical Society: Washington D.C., 1984; pp 195-213.
9. A. Vazquez, A. J. Rojas, H. E. Adabbo, J. Borrajo, R. J. J. Williams, *polymer*, **28**, 1156 (1987).
10. K. Yamanaka, Y. Takagi, T. Inoue, *Polymer*, **60**, 1839 (1989).
11. D. Verchere, J. P. Pascault, H. Sautereau, S. M. Moschiar, C. C. Ricaardi, R. J. J. Williams, *Appl. Polym. Sci.* **43**, 293 (1991).
12. O. Kwon, T. C. Ward, *J. Comp. Theor. Polym. Sci.*, (1998), in press.

Chapter 2: BACKGROUND AND LITERATURE REVIEW

2.1. THERMOSETTING NETWORKS

A thermosetting network may be defined as an enormous macromolecule that has irreversibly formed a three-dimensionally crosslinked structure by chemical bonding or other reactions between active species. During the crosslinking reaction (cure), the reactive monomers grow in molecular weight (MW) to form branching structures and eventually interlink to form the three-dimensional network[1,2]. In the limit that all fusible and soluble reactants are linked together, the "complete" crosslinked macromolecules then cannot be dissolved in a solvent. Prior to that point a certain "sol-fraction" exists. The "pure", sol-free, network is not fusible even at elevated temperatures unless chemical bonds are broken. In order to form such a three-dimensional network, some of the reactant molecules must have more than two functional groups per molecule in order to initiate branching in the polymerization. The variation of chemical structure during the cure is represented in Figure 2-1.

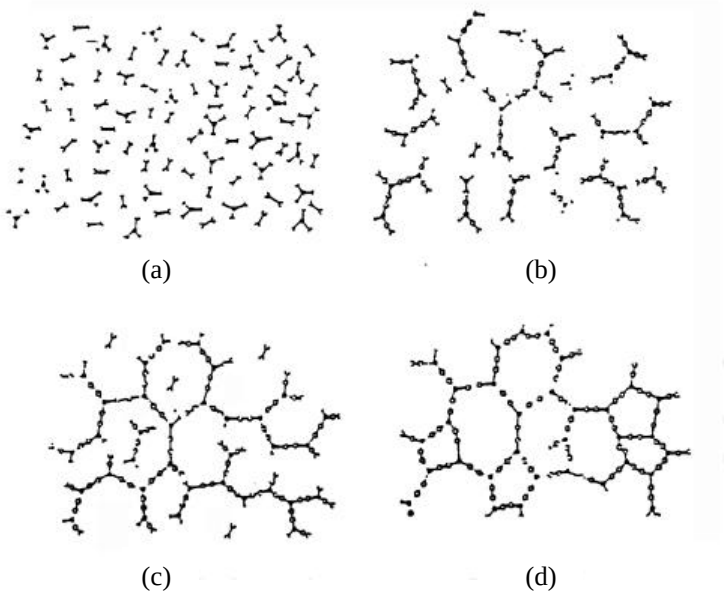

Figure 2-1. Schematic 2-D representation of thermoset formation: a) A-stage, partially polyfunctional monomer; b) B-stage, linear and branched materials below gel point; c) Incipient state of gel, gelled but incompletely crosslinked network with significant sol fraction; d) Fully cured C-stage thermoset.[2]

Some of the reasons that thermosets are often used as composite structural materials derive from their abilities to consolidate the different components due to their initial low viscosity, and also their high glass transition temperatures and good dimensional stability under stress due to their network structure after being cured. All these latter properties are due to their network structure. Crosslinked polymer networks do not dissolve to form a true solution; but they may swell in good solvents to form a gel. Also they do not flow at elevated temperatures in contrast to thermoplastics. Crosslinked polymers generally behave like soft but elastic solids when heated above the glass transition temperature. This "rubbery plateau" is illustrated in Figure 2-2.

One of the important parameters used to characterize a crosslinked polymer other than those that are used for the thermoplastic polymers is the crosslink density, or, equivalently, the molecular weight between chemical crosslinks, $<M_C>$. This parameter is strongly related to their physical and mechanical properties. Generally, high crosslink density, or low $<M_C>$, yields high rigidity, strength, solvent resistance and possibly improved thermo-oxidative stability. However, highly crosslinked networks exhibit restricted molecular mobility, which often translates into undesirable brittleness, low strains to failure, poor impact properties and poor fracture toughness.

The initial reacting resins for thermosets are not necessarily low MW monomers. Macromonomers, which consist of oligomeric species with reactive terminal groups, can be used as a starting monomer for networks that grows, branches and crosslinks by the usual formation of chemical bonds between the reactive groups, if an effective average functionality per molecule greater than two is provided. This curing reaction may take place through either step-growth (condensation) or chain-growth (addition) polymerization. The useful crosslinking systems from a historical standpoint and for industrial applications include phenol-formaldehyde networks (resols and novolacs),

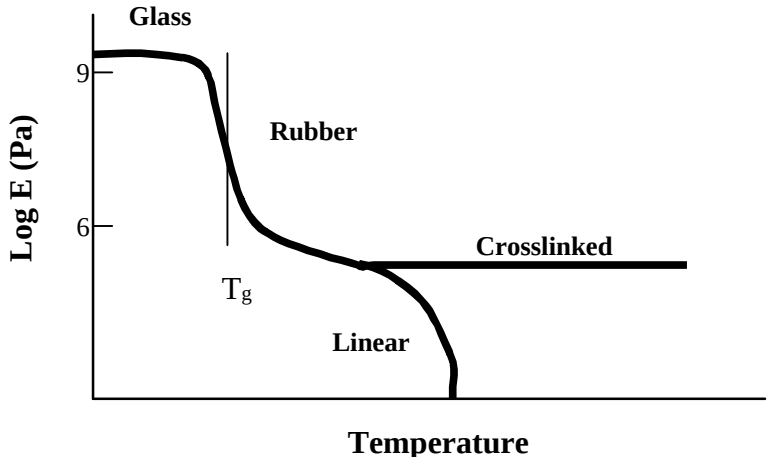

Figure 2-2. Typical variation of Young's modulus (E) with temperature for a polymer showing the effect of crosslinking to produce the rubbery state.

unsaturated polyesters, epoxy networks cured with diamines, acids, or anhydrides, polyurethane, polyurea, amino resins (formaldehyde with urea, melamine or acrylic), acetylene derivatives, silicones, polyimides, cyanates and vulcanization of unsaturated hydrocarbons[3].

2.2. NON-LINEAR STEP-GROWTH POLYMERIZATION

Regardless of the molecular size of the monomers, reactive functional groups greater than two per chain assure branching geometries. If the polymerization proceeds further, there will be an extent of conversion called as the gel point where a three dimensional network structure incipiently forms and the weight average molecular weight goes to infinity. This network formed is called the gel. Depending on stoichiometry and functionality, a portion of molecules will not be chemically connected to the three dimensional network and they can usually be extracted by certain solvents (sol fraction).

As the polymerization proceeds beyond the gel point, the amount of gel increases at the expense of the sol. The mixture of the sol and gel rapidly transforms from the sol/gel rubbery state to eventually the gelled glassy state if the cure temperature is lower than the glass transition temperature of the fully cured material. This second transition process is called vitrification. The time or extent of conversion required for vitrification in an isothermal cure can be defined by the requirement that the glass transition temperature reaches the temperature of cure. The time to gelation is an important parameter for industrial considerations in that it defines the processible (working) time range or shelf life. Because the material beyond the gel becomes insoluble and infusible, it cannot be molded for desired shapes once that point is reached. On the other hand the vitrification is important not only because there material transforms to a glassy solid, but because the chemical reaction is essentially frozen at a temperature of cure below the maximum glass transition temperature that the material can exhibit. Therefore, it is quite useful to know the relationships between gelation, vitrification, and the sol/gel fraction to the degree of conversion, which is a function of temperature and time. From the statistical parameters of a crosslinking reaction system, the gel point can be predicted. Since this dissertation deals with the step polymerization of epoxy with a diamine, prediction of the gel point and molecular weight distribution as a function of the extent of conversion for the step polymerization is essential and will be introduced in the next sections.

2.2.1. Flory-Stockmayer Approach

Flory[4] and Stockmayer[5] derived expressions for the size distribution of finite molecules as a function of the extent of conversion, assuming that all the functional groups are equally reactive, independent of molecular weight or viscosity. All the reactions were assumed to occur between functional groups on different molecules (no ring formation). Their derivations were based on combinatorial arguments and thus the distribution functions for nonlinear multi-functional polymers become quite complex[6]. The distribution functions depend upon the functionality and relative amounts of all the units

(x-mers) involved. In the case of homopolymerization of monomers with *f* functionality, the weight fraction of x-mers at a certain extent of conversion, *p*, can be described by

$$W_x = \frac{(fx - x)!\, f}{(x-1)!\,(fx - 2x + 2)!}\, p^{x-1}(1-p)^{fx-2x+2} \qquad (2\text{-}1)$$

Figure 2-3 represents the variation of the weight fraction of *x*-mer species as step-growth polymerization progresses. The number average molecular weight, $\overline{M_n}$, at a certain *p* is given by

$$\overline{M_n} = M_0 \frac{2}{2 - fp} \qquad (2\text{-}2)$$

where M_0 is the molecular weight of the monomer. The weight average molecular weight, $\overline{M_w}$, at a certain *p* is expressed as

$$\overline{M_w} = M_0 \frac{1+p}{1-(f-1)p} \qquad (2\text{-}3)$$

2.2.2. Macosko Approach

The Flory and Stockmayer approach is quite impressive in that it describes the evolution of MW distribution as the reaction proceeds. However, it is very tedious and complex to generalize the distribution functions for a different system. Such an example

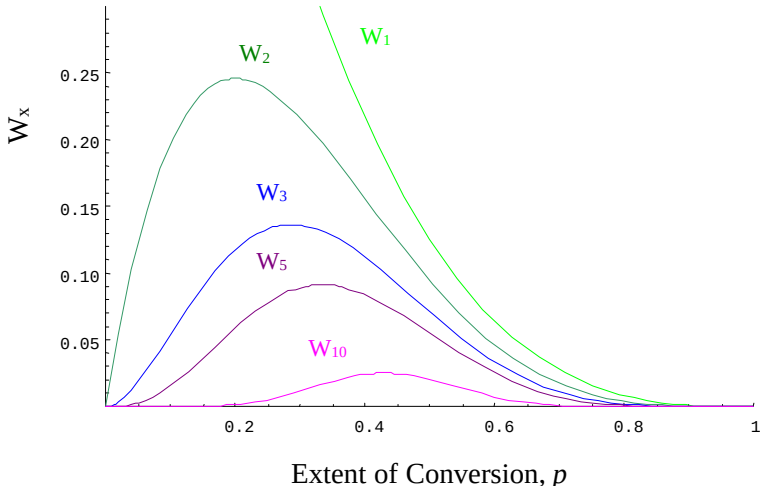

Figure 2-3. Weight fractions of various molecular species in a trifunctional step polymerization as a function of degree of conversion[1]. The weight fractions of the finite species were calculated from equation (2-1)

will be a system of A_f moles of f functional A-type monomer reacting with B_g moles of g functional B-type monomer. Our interest in thermosetting cure is to relate the average molecular weight to the degree of conversion so that we can mathematically express the average properties of non-linear polymers as a function of the extent of conversion. Macosko and Miller[7] developed mathematical models for a networking polymer that provide a generalized relationship between average molecular weight and the extent of conversion with the same assumptions as Flory and Stockmayer made.

Macosko and Miller have used the law of total probability for expectations in order to know the expectation value or average weight at a certain degree of conversion[7]. Let us define that $W_{A'}^{out}$ is the weight of groups attached to a randomly selected *A'* looking out from its parent molecule and $W_{A'}^{in}$ is the weight of groups attached to *A'* looking into its parent molecule as illustrated in Figure 2-4. Then $W_{A'}^{out}$ varies depending on its reacting status. As shown in Figure 2-4, $W_{A'}^{out}$ is equal to zero if *A'* does not react with *B* (as a simple notation, $W_{A'}^{out}\left|A_{noreact}\right.$),and $W_{A'}^{out}$ equals $W_{B''}^{in}$ if *A'* reacts with *B* (as a simple notation, $W_{A'}^{out}\left|A_{react}\right.$). In terms of a simple notation,

$$W_{A'}^{out} = \begin{cases} W_{A'}^{out}\left|A_{noreact} = 0\right. \\ W_{A'}^{out}\left|A_{react} = W_{B''}^{in}\right. \end{cases} \tag{2-4}$$

We can use conditional expectation theorem to find the expected weight attached groups on any *A* looking out from its parent molecule, $E(W_A^{out})$,

$$E\left(W_A^{out}\right) = E\left(W_A^{out}\left|A_{react}\right.\right)P\left(A_{react}\right) + E\left(W_A^{out}\left|A_{noreact}\right.\right)P\left(A_{noreact}\right) \tag{2-5}$$

where $E(e)$ is the expectation for an event, e, to occur and $P(e)$ indicates the probalility for an event, e, to happen.

The extent of conversion, p, can be defined as a fraction of the amount of consumption of *A* to the total A_{f0}, *i.e.*,

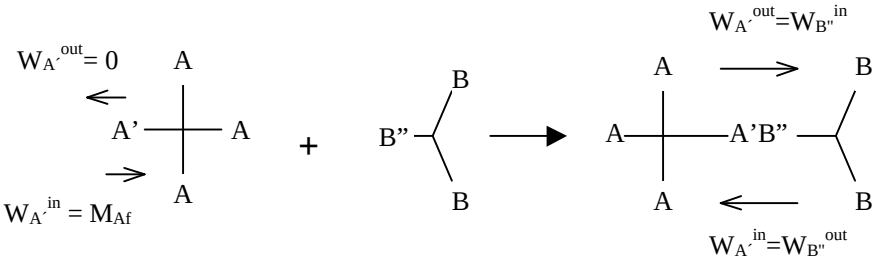

Figure 2-4. Schematic reaction of $\boldsymbol{A_4}$ with $\boldsymbol{B_3}$.

(2-6) $$p = p_A = \frac{A_{f0} - A_{ft}}{A_{f0}}$$

where A_{f0} is the total moles of A groups initially present in the system and A_{ft} is the moles left after a certain reaction time, t. Therefore, we can consider $P(A_{react})$ as p and $P(A_{noreact})$ as 1-p. Also if the functional group A is assumed to react only with the functional group B, the extent of conversion, p_B, with respect to B can be similarly defined. Thus the relationship between p_A and p_B can be expressed as

(2-7) $$p_B = \frac{fA_f}{gB_g} p_A = rp$$

where $r = \frac{fA_f}{gB_g}$. Then replacing the terms in equation (2-5) with equations (2-4) and (2-6) reduces to

(2-8) $$E\left(W_A^{out}\right) = pE\left(W_B^{in}\right)$$

In a similar way as in equation (2-4), the weight of groups attached to B looking out from the parent molecule, W_B^{out}, can be expressed as

(2-9) $$W_B^{out} = \begin{cases} W_B^{out} \middle| B_{noreact} = 0 \\ W_B^{out} \middle| B_{react} = W_A^{in} \end{cases}$$

And thus the following recursive formula in terms of W_B^{out} is obtained as equation (2-8) was obtained from equation (2-2):

(2-10) $$E\left(W_B^{out}\right) = rpE\left(W_A^{in}\right)$$

The molecular weight, W_{Af}, of the molecule to which a randomly selected A_f belongs will be the sum of the weight of groups attached to A looking into the parent molecule (W_A^{in}) and the weight of groups attached to A looking out from the parent molecule (W_A^{out}). Therefore, the average molecular weight attached to a randomly selected A_f will be

(2-11) $$E\left(W_{Af}\right) = E\left(W_A^{in}\right) + E\left(W_A^{out}\right)$$

By the same token,

(2-12) $$E\left(W_{Bg}\right) = E\left(W_B^{in}\right) + E\left(W_B^{out}\right)$$

The expected weight on any A looking into its parent molecule, $E(W_A^{in})$ will be the molecular weight of A_f plus the total weight of the groups attached to the other remaining (f-1) A's, which is just $(f\text{-}1)E(W_A^{out})$. Thus,

$$E\left(W_A^{in}\right) = M_{Af} + (f-1)E\left(W_f^{out}\right) \text{ and } E\left(W_B^{in}\right) = M_{Bg} + (g-1)E\left(W_B^{out}\right) \tag{2-13}$$

Solving equations (2-8), (2-10), (2-13) for $E(W_A^{in})$ and $E(W_B^{in})$ yields

$$E\left(W_A^{in}\right) = \frac{M_{Af} + p(f-1)M_{Bg}}{1 - rp^2(f-1)(g-1)} \tag{2-14}$$

$$E\left(W_B^{in}\right) = M_{Bg} + rp(g-1)\frac{M_{Af} + p(f-1)M_{Bg}}{1 - rp^2(f-1)(g-1)} \tag{2-15}$$

Substitution of equations (2-8), (2-10), (2-14), and (2-15) into equations (2-11) and (2-12) provides

$$E\left(W_{Af}\right) = M_{Af} + pf\,\frac{rp(g-1)M_{Af} + M_{Bg}}{1 - rp^2(f-1)(g-1)} \tag{2-16}$$

$$E\left(W_{Bg}\right) = M_{Bg} + rpg\,\frac{M_{Af} + p(f-1)M_{Bg}}{1 - rp^2(f-1)(g-1)} \tag{2-17}$$

The weight average molecular weight can be computed from equations (2-16) and (2-17):

$$\overline{M_W} = w_{Af}E\left(W_{Af}\right) + \left(1 - w_{Af}\right)E\left(W_{Bg}\right) \tag{2-18}$$

where w_{Af} is the weight fraction of monomer, A_f and thus it can be computed from

$$w_{Af} = \frac{M_{Af}A_f}{M_{Af}A_f + M_{Bg}B_g} \tag{2-19}$$

Therefore, when monomers A with f functionality and B with g functionality are polymerized, the weight average molecular weight at a certain conversion, p, is expressed as

$$\overline{M_W} = \frac{\frac{rg}{f}\left(1 + (g-1)rp^2\right)M_{Af}^2 + \left(1 + (f-1)rp^2\right)M_{Bg}^2 + 2rpgM_{Af}M_{Bg}}{\left(\frac{rg}{f}M_{Af} + M_{Bg}\right)\left(1 - (f-1)(g-1)rp^2\right)} \tag{2-20}$$

This equation (2-20) is more general than the Flory-Stockmayer approach in that it can cover the crosslinking by homopolymerization as introduced in the previous section. For

homopolymerization, it can be regarded that $A_f = B_g$, $f = g$ and $r = 1$. Then equation (2-20) is reduced to equation (2-3). However, the Macosko approach does not provide molecular weight distribution information at a given extent of conversion.

The number average molecular weight can be calculated from stoichiometry. At extent of conversion, p, the number average molecular weight is the total mass divided by the number of molecules present. Since the number of monomers which participate in the new bond formation till a certain conversion is pfA_f and the number of molecules which existed initially is $A_f + B_g$, the number average molecular weight is given by

$$\overline{M_N} = \frac{M_{Af}A_f + M_{Bg}B_g}{A_f + B_g - pfA_f} = \frac{\frac{rg}{f}M_{Af} + M_{Bg}}{1 + \frac{rg}{f} - rpg} \qquad (2\text{-}21)$$

This equation (2-21) can be reduced to equation (2-2) when homopolymerization takes place. The gel point, p_{gel}, is the extent of conversion where the weight average molecular weight approaches infinity. Thus

$$p_{gel} = \frac{1}{\sqrt{r(f-1)(g-1)}} \qquad (2\text{-}22)$$

We have reviewed average molecular structure as a function of the extent of conversion for the step-growth polymerization. The recursive approach of Macosko has some advantage over the combinatorial approach of Flory-Stockmayer in that the derivations of the former are simpler and more generalized than the latter. The recursive technique can be extended to treat the chain-growth polymerization and to take into account the problem of condensation by-products produced in the step-growth polymerization. However, since this dissertation is dedicated to investigate the cure of epoxy resin with catalytic or stoichiometric amounts of diamines, discussion of further application of the technique was not intended. The derived relations by Macosko's technique and the properties of the monomer molecules will be employed in the later chapters to derive thermal and rheological parameters which depend on the molecular structure.

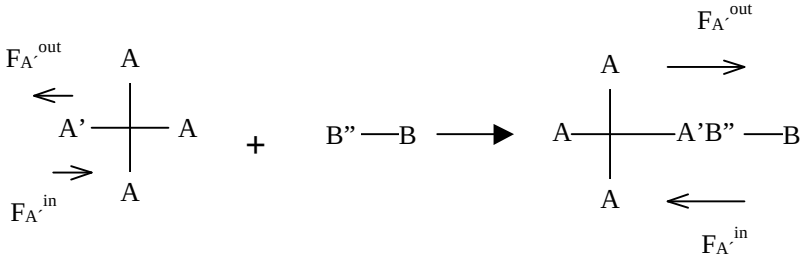

Figure 2-5. Schematic reaction of $\boldsymbol{A_4}$ with $\boldsymbol{B_2}$.

2.2.3. Prediction of Gel Fraction and Crosslink Density

The weight fraction of sol,w_s, and crosslink density, X, beyond the gel point can be calculated as a function of the extent of conversion from the knowledge of the structure of the starting monomers using the similar recursive method. The derivations of these relations will be described with the case of the step-growth polymerization of A_f+B_2 system. Since the sol fraction is the fraction of finite chains to all chains in the system at a certain degree of conversion, p, we will look for the probability of a randomly selected A group being attached to a finite or dangling chain rather than to the infinite network.

Let F_A^{out} be the event that a randomly selected A group is the start of a finite chain looking out from its parent molecule. The probability of the event, F_A^{out}, if A does not react, $P(F_A^{out} \mid A_{noreact})$, will be unity because all finite chains (sol) are reactants. If A reacts, the probability, $P(F_A^{out} \mid A_{react})$, will be equal to $P(F_B^{in})$, because the reaction always connects A group to B group. The probability of $P(F_A^{out})$ is the fraction of finite chains (sol) which have A groups as end groups. Therefore, using the law of total probability as in equation (2-5),

$$\begin{aligned} P\left(F_A^{out}\right) &= P\left(F_A^{out}\middle|A_{react}\right)P\left(A_{react}\right) + P\left(F_A^{out}\middle|A_{noreact}\right)P\left(A_{noreact}\right) \\ &= P\left(F_B^{in}\right)p_A + 1\left(1-p_A\right) \end{aligned} \tag{2-23}$$

$$\begin{aligned} P\left(F_B^{out}\right) &= P\left(F_B^{out}\middle|B_{react}\right)P\left(B_{react}\right) + P\left(F_B^{out}\middle|B_{noreact}\right)P\left(B_{noreact}\right) \\ &= P\left(F_A^{in}\right)p_B + 1\left(1-p_B\right) = rpP\left(F_A^{in}\right) + 1 - rp \end{aligned} \tag{2-24}$$

where p_A is the fraction of A groups which have reacted and p_B the fraction of B groups, $p_B = rp_A = rp$ (see equation (2-7)). For an A group to be a finite chain looking into its parent molecule, all of the other (f-1) A groups must be finite. Thus,

$$P\left(F_A^{in}\right) = P\left(F_A^{out}\right)^{f-1} \tag{2-25}$$

and similarly, since the functionality of the B_2 molecule is two,

$$P\left(F_B^{in}\right) = P\left(F_B^{out}\right) \tag{2-26}$$

Combining equations (2-23) through (2-26) yields

$$\left(rp^2\sum_{i=0}^{f-2}P\left(F_A^{out}\right)^i - 1\right)\left(P\left(F_A^{out}\right) - 1\right) = 0 \tag{2-27}$$

The roots of equation (2-27) are $P(F_A^{out}) = 1$ or $rp^2\sum_{i=0}^{f-2}P\left(F_A^{out}\right)^i - 1 = 0$. $P(F_A^{out}) = 1$ physically implies that the system has not yet gelled and is not of our interest. The gel point can be independently determined from equation (2-27). In order for a system to

have no infinite network, no solution should exist between 0 and 1 for the following equation:

$$g(x) = rp^2 \sum_{i=0}^{f-2} x^i - 1 = 0 \qquad (2\text{-}28)$$

where $x = P(F_A^{out})$. The function, $g(x)$, is monotonically increasing for x between 0 and 1, and $g(0)$ = -1 and $g(1) = rp^2(f-1) - 1$. Therefore, if $rp^2(f-1) - 1$ is less than 0, equation (2-28) has no root between 0 and 1. When $rp^2(f-1) - 1 = 0$, then an infinite network starts to form. That is,

$$p_{gel} = \frac{1}{\sqrt{r(f-1)}} \qquad (2\text{-}29)$$

Thus, the roots of the equation (2-27) are for a system of A_4+B_2,

$$P(F_A^{out}) = \begin{cases} 1 & \text{for } p \le p_{gel} \\ \left(\frac{1}{rp^2} - \frac{3}{4}\right)^{\frac{1}{2}} - \frac{1}{2} & \text{for } p > p_{gel} \end{cases} \qquad (2\text{-}30)$$

All f arms of a randomly chosen A_f molecule should be connected to a finite chain to remain as sol. Also both arms of a randomly chosen B_2 molecule should be connected to a finite chain to remain as sol. Thus the weight fraction of sol is computed

$$w_s = w_{Af} P(F_A^{out})^f + (1 - w_{Af}) P(F_B^{out})^2 \qquad (2\text{-}31)$$

where ω_{Af} is the weight fraction of monomer A_f (see equation (2-19)). Substitution of equation (2-25) into equation (2-24) yields

$$P(F_B^{out}) = rpP(F_A^{out})^{f-1} + 1 - rp \qquad (2\text{-}32)$$

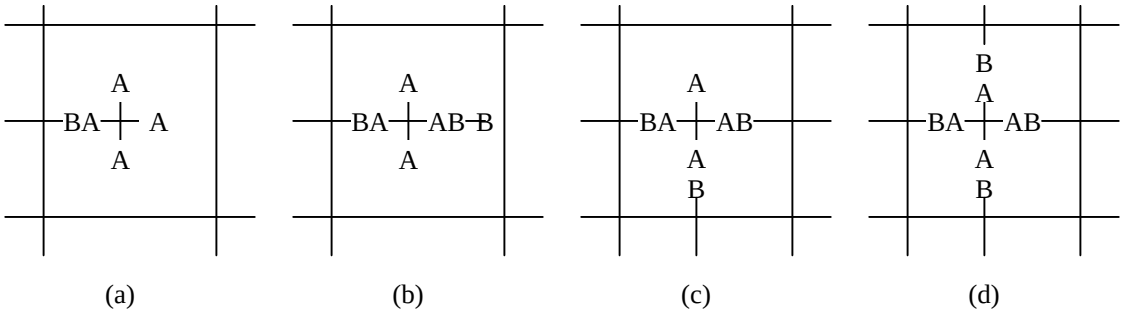

(a) (b) (c) (d)

Figure 2-6. Examples of ineffective and effective junctions: (a) ineffective 1 arm dangling connection (b) ineffective 2 arm connection (c) effective 3 arm connection (d) effective 4 arm connection

Another important network property is the crosslink density or the concentration of effective junction points in the infinite network. For a randomly selected A_f to act as an effective junction point, three or more of its arms should be connected to the infinite network as illustrated in Figure 2-6 (c) and (d). If one or two arms of this A_f molecule are connected to the network, these connections are not contributing to the crosslink density as illustrated in Figure 2-6 (a) and (b). The molecule B_2 cannot act as effective junction points. The probability that all four arms of A_4 are connected to the infinite network is

$$P\left(X_{4,4}\right) = \left(1 - P\left(F_A^{out}\right)\right)^4 \tag{2-33}$$

The probability that three arms of A_4 are connected to the infinite network is

$$P\left(X_{3,4}\right) = \binom{4}{3} P\left(F_A^{out}\right)\left(1 - P\left(F_A^{out}\right)\right)^3 = 4P\left(F_A^{out}\right)\left(1 - P\left(F_A^{out}\right)\right)^3 \tag{2-34}$$

Figure 2-7 illustrates variations of the weight and number average molecular weights, sol fraction, and probabilities of effective junction points as functions of the extent of conversion for DGEBA/DDS system. The weight average molecular weight goes to infinity at the gel point of 0.577 where an infinite network starts to form. The system consists of all sol components till the gel point. The weight fraction of sol rapidly decreases in the post gel stage while the effective three-arm crosslinks ($P(X_{3,4})$) increase initially to a maximum and then decreases. The effective four-arm crosslinks ($P(X_{4,4})$) form chasing the trend of $P(X_{3,4})$ and then increase rapidly to unity at complete conversion.

The total probability of the effective crosslinks, *i.e.*, the sum of $P(X_{3,4})$ and $P(X_{4,4})$ is the fraction of crosslinks. It is useful to represent the fraction of crosslinks in terms of the concentration of effective network junctions or crosslink density (the number of junctions per unit volume or mole of junctions per unit volume). The crosslink density is

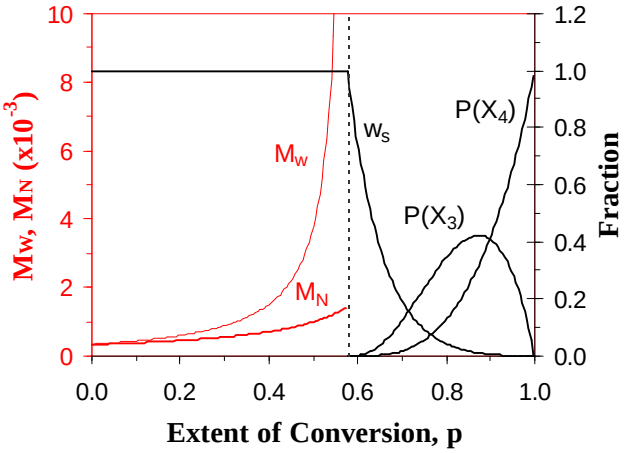

Figure 2-7. Calculated properties as a function of the extent of cure for DGEBA epoxy (374 g/mol) cured with DDS (248 g/mol) in stoichiometric ratio.

just the initial concentration of A_f times the probability summed over all effective crosslinks. That is, for the A_4+B_2 system,

$$[X] = [A_4]_0 \left(P(X_{3,4}) + P(X_{4,4})\right) \tag{2-35}$$

2.3. TIME-TEMPERATURE-TRANSFORMATION DIAGRAMS

In the previous sections, we have explained how low molecular weight liquid reactants are transformed to high molecular weight amorphous solid polymers or three-dimensional networks as the chemical reaction proceeds. The product properties are determined by the chemical structure of the reactants and reaction conditions. Once the reacting materials are characterized in terms of stoichiometry and their functionalities, the average molecular weight variations can be estimated as a function of the extent of conversion from the theories explained in the previous sections.

For thermosetting systems, it is substantially useful in industrial applications to establish relations of transition phenomena such as gelation, vitrification, and/or phase separation to reaction time at different cure temperatures so that the desired properties can be controlled. In this sense, the Flory-Stockmayer and Macosko approaches described in the previous sections are substantial contributions to practical applications as well as to the science. Their techniques provided the variation of the molecular structure as a function of the extent of conversion. Since such transition phenomena can be related to the chemical structure, they can be related to the extent of conversion that is a function of temperature and time. For a practical application of such relations, it would be noteworthy that such transition phenomena are directly related to the cure temperature and time. Gillham *et al.*, were the first investigators in polymer to experimentally and

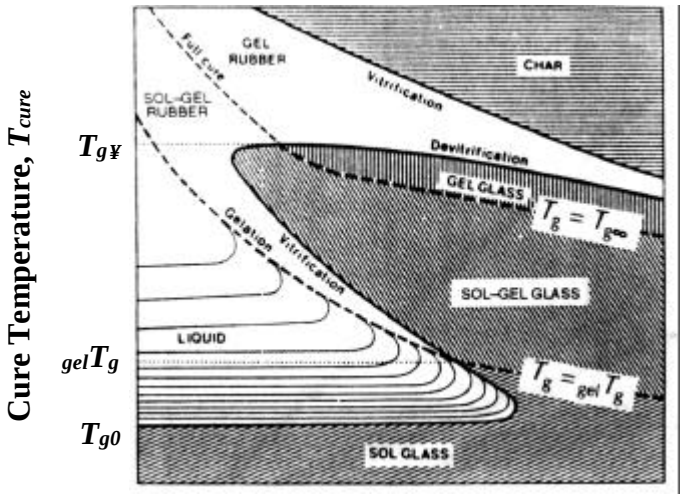

Figure 2-8. Schematic TTT diagram for a thermosetting system. The successive iso-viscous contours are shown in the liquid region.

theoretically establish a diagram that provides a map of the different states encountered during isothermal cure[8-11]. The contours of the time to gelation and the time to vitrification at different reaction temperatures form the basis of the isothermal time-temperature-transformation (TTT) cure diagram as shown in Figure 2-8.

In the schematic TTT diagram presented in Figure 2-8, the seven distinct states of matter are indicated in the space of log time and the isothermal cure temperature, T_{cure}. They are liquid, sol/gel rubber, gel rubber, sol glass, sol/gel glass, gel glass, and char. These states of matter are divided by the curves of gelation, full cure, vitrification, and devitrification. The three characteristic glass transition temperatures are also shown: T_{g0}, ${}_{gel}T_g$, and $T_{g\infty}$. T_{g0} is the glass transition temperature of the uncured reactants. Below this temperature, the system essentially has no reactivity due to the frozen mobility of molecules. Thus the material is in a glass state containing only sol.

When the system is cured at a temperature above T_{g0}, the molecules will react with each other to grow and branch and the glass transition temperature rises due to the molecular weight increases. If the glass transition temperature rises to the cure temperature before the formation of three-dimensional networks, then the material is solidified and the chemical reaction is quenched. Because the material has solidified with no gel fraction, it is called sol glass and is soluble and fusible.

If the material is cured at a temperature higher than ${}_{gel}T_g$, at which gelation occurs simultaneously with vitrification, gelation occurs first to form three-dimensional networks and then vitrification occurs when the glass transition temperature reaches the cure temperature. Even after gelation, the reactive molecules can further react with increase in gel fraction until reaction is quenched by the vitrification. The material in this region is called sol/gel rubber because it includes sol and gel together at the temperature above the glass transition temperature. After the vitrification, the molecular mobility is substantially decreased and the chemical reaction is essentially quenched. It has been reported that the glass transition temperature increases at a reduced rate even beyond vitrification[12]. It implies that the reaction occurs in the glassy state on prolonged isothermal cure beyond vitrification.

Cure above $T_{g\infty}$, which is the maximum glass transition temperature of the system, leads to gelation but does not vitrify. Further reaction will reduce the sol fraction to zero at the full cure. The region between gelation and the full cure is the sol/gel rubber state and the region after the full cure is gel rubber without degradation. Lowering temperature after the full cure put the material into the gel glass region. The determination of the full cure curve is important in that comparison of properties of a system to those of another would not be fair without achieving the same cure states. Postcure above $T_{g\infty}$ for enough time to achieve the full cure before the degradation of the materials is the most frequently used way for achieving the same states of cure.

At high temperatures, thermal degradation becomes important and may prevent full cure from being achieved[13]. Two degradation events have been noted in relation to the TTT diagram: devitrification followed by elastomer formation; and vitrification followed by char formation. Devitrification is the consequence of thermal degradation

that can result in a decrease of T_g at high cure temperatures. The onset of char formation can result in increase of T_g and rigidity.

The TTT isothermal cure diagram is often extended to include multiphase systems such as rubber or thermoplastic modified thermosets. In such modified systems, a homogeneous solution of rubber with thermoset resins is usually employed at the initial reaction stage. As polymerization proceeds, phase separation usually takes place due to the conformational entropy change induced by the chain growth of crosslinking molecules. The final morphology of the product is greatly influenced by the cure schedule. The incipient time of the phase separation is normally measured by the cloud point, where the intensity of transmitted light decreases dramatically. These cloud points measured at different cure temperatures can be incorporated in the TTT diagram. The fundamental phase separation phenomena will be reviewed in later sections to discuss morphology control in later chapters.

2.4. THERMODYNAMICS OF PHASE SEPARATION

Variation of temperature, pressure, and/or composition of a mixture may result in phase separation from a homogeneous single phase to binary or multi-phases depending on which state is more stable. Thermodynamic evaluation of a system provides only information about the stability of the system at given external variables. For example, if a temperature is abruptly changed to another temperature, the system tries to adjust to a new state with the minimum free energy available in the new environment. Thermodynamics describes only where the most stable state lies, but does not describe the path of the system. Therefore, in a predicted model, the final state of the system should be dictated by the combined effects of the thermodynamics of the system and the kinetics of the path. This latter effect is particularly significant for macromolecules. We will examine

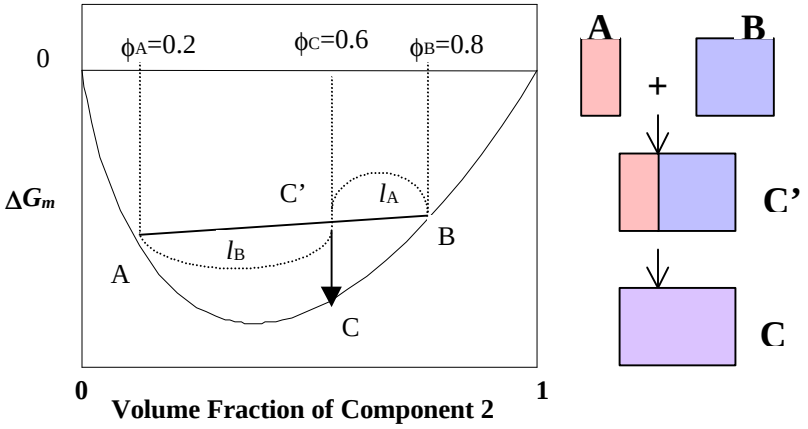

Figure 2-9. Schematic diagram of free energy as a function of composition. Phase A is mixed with phase B and generate a new single phase C.

thermodynamic phase equilibria first without kinetic considerations on phase separation.

The stability of the system is determined from the free energy of mixing, DG_m. The following two requirements should be satisfied for a binary mixture to be miscible at any composition, ϕ:

1. $\Delta G_m(f) < 0$: The free energy should be negative.

2. $\frac{\partial^2 \Delta G_m}{\partial f^2}(f) > 0$: The free energy curve should be concave upwards.

If two components are always miscible regardless of the composition, the two miscibility conditions should be satisfied for all compositions and the free energy curve should be concave downwards for all compositions as illustrated in Figure 2-9. Imagine two phases, *A* and *B*, and phase *B* is twice the volume of phase *A*. Assume that phase *A* is a homogeneous solution of component 1 and 2, where the volume fraction of component 2 is 0.2. Furthermore, phase *B* is a homogeneous mixture of component 1 and 2, where the volume fraction of component 2 is 0.8.

When these two phases contact each other to make a new system that is three times bigger than phase *A*, there are two possibilities. One possibility is that the two phases mix to form a new phase *C* and the other is that they remain phase separated system, shown as *C'=A+B*. The amount of component 2 in *C* or *C'* should be the sum of component 2 used to be in phases *A* and *B*. Therefore, the volume fraction of component 2 in *C* or *C'* is

$$f_C = \frac{0.2 \times 1 + 0.8 \times 2}{3} = 0.6$$

When the mixture remains phase separated (*C'*), the volume fraction of phase *A* is 1/3 and the volume fraction of component 2 is the same as that in phase *C*. Point *C'* in the free energy diagram corresponds to the free energy of the heterogeneous mixtures of *A* and *B* that is higher than the free energy of point *C*. Hence, the mixture of *A* and *B* will form a homogeneous solution with $f_C = 0.6$.

Now let us consider a system that is miscible in a certain composition range and immiscible in the other range. This will occur when the free energy curve includes a concave-upwards in a certain composition range. In other words, the second derivative of the free energy with respect to composition should change the sign from positive to negative. The point where the convexity changes (*i.e.*, $\left(\frac{\partial^2 \Delta G_m}{\partial f^2}\right)_{p,T} = 0$) is an inflection point marked as points S or S' in Figure 2-10. The inflection points are referred to as spinodal points. This situation is illustrated in Figure 2-10 which is a combination of two concave-upward curves and a concave-downward curve. We will show that any composition between the two inflection points is unstable such that the homogeneous solution of the composition does not exist.

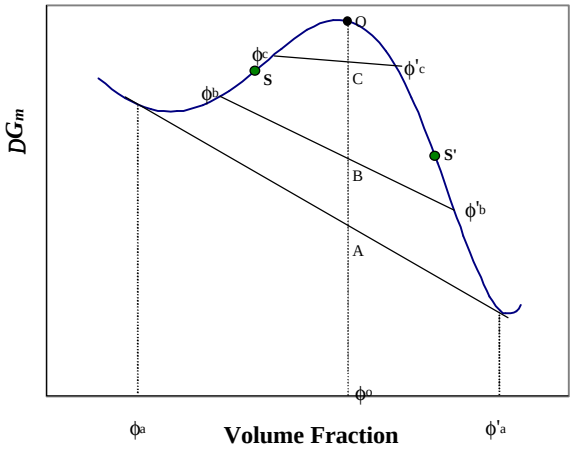

Figure 2-10. Schematic diagram of the free energy as a function of composition in the unstable region inside the two inflection points denoted as S and S'.

Suppose that there is a homogeneous solution of composition ϕ_o that lies in the unstable region (point O in Figure 2-10). The free energy of point O should be compared to those of any two separated phases of which each composition is different to each other, but whose average composition is also ϕ_o. To satisfy these requirements, one phase (*e.g., a*) should lie at ϕ_a less than ϕ_o, and the other phase (*e.g., a'*) should lie at ϕ'_a higher than ϕ_o. The volume fraction of one phase can be computed from mass balance and the free energy of the mixture will be the average of the free energies of the two phases. For example, when the two phases are *c* and *c'*, the volume fraction of *c* is

$$v_f = \frac{f'_c - f_o}{f'_c - f_c} = \frac{\Delta G_m(C) - \Delta G_m(f'_c)}{\Delta G_m(f_c) - \Delta G_m(f'_c)} \tag{2-36}$$

If we denote the free energy value of point C as ΔG_m(C), then the free energy of the mixture of phase *c* and phase *c'* with volume fraction v_f is

$$\begin{aligned} \Delta G_m(\text{mix. of } c \text{ and } c') &= v_f \Delta G_m(f_c) + (1 - v_f)\Delta G_m(f'_c) \\ &= \frac{(f'_c - f_o)\Delta G_m(f_c) + (f_o - f_c)\Delta G_m(f'_c)}{f'_c - f_c} \\ &= \frac{(\Delta G_m(C) - \Delta G_m(f'_c))\Delta G_m(f_c) + (\Delta G_m(f_c) - \Delta G_m(C))\Delta G_m(f'_c)}{\Delta G_m(f_c) - \Delta G_m(f'_c)} \\ &= \Delta G_m(C) \end{aligned} \tag{2-37}$$

Since the free energy of point O is higher than that of point C, the system would rather phase separate (mixture of *c* and *c'*) than remain a homogeneous solution (single phase O). However, the combination of *c* and *c'* does not provide the lowest free energy. Hence, phase separation will proceed spontaneously and continuously through the succes

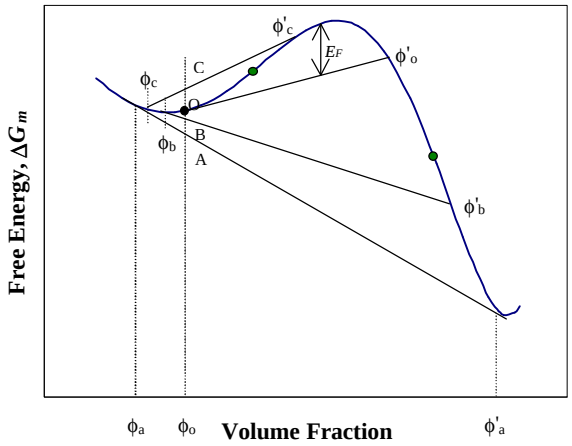

Figure 2-11. Schematic diagram of the free energy as a function of composition in the metastable region.

sive phases until the lowest free energy is achieved as represented by *a* and *a'* in Figure 2-10. The points where the lowest free energy are achieved are defined as binodal points. These two binodal phases have the same chemical potential and thus the two phases can co-exist thermodynamically in the system.

Consequently, once phase separation has occurred in the spinodal region through any small perturbation in composition, the system cannot homogenize spontaneously because that would require an uphill climb from the free energy well. The spinodal points define the boundary, inside which any composition would spontaneously phase separate. Phase separation that occurs in the spinodal region is referred to as spinodal decomposition.

Now let us consider a case in which an initial homogeneous solution (point O) of composition f_o lies in the region between a binodal and a spinodal points as illustrated in Figure 2-11. Any small perturbation of composition about f_o in the region between f_c and f_c' would result in two phases whose average free energy is higher than that of the homogeneous solution (point O). Thus, it would remain as a single phase. The composition of a new phase must be higher than f_o' to obtain the free energy of the mixture lower than that of homogeneous phase O. The composition, f_o', is the one corresponding to the intersection point of the free energy curve and the tangent line at f_o. Thus, phase O is metastable since it requires the activation energy (E_F) for phase separation. Consequently, the binodal point defines the boundary between stable state and metastable state. Phase separation within the metastable region occurs through a nucleation and growth mechanism.

We have considered the miscibility of a binary mixture at a constant temperature and pressure. The behavior of miscibility at different temperatures can be represented in a

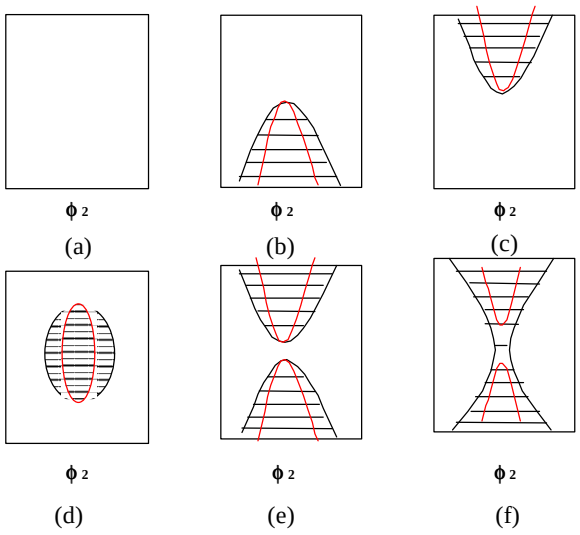

Figure 2-12. Schematic representations of typical phase diagram for liquid-liquid binary mixture. Shaded areas indicate metastable and unstable regions.

phase diagram. Some typical phase diagrams for liquid-liquid mixture are schematically presented in Figure 2-12[14]. These diagrams can be constructed mathematically by evaluating the binodal and spinodal points determined from free energy curves at different temperatures. The free energy should be mathematically expressed as a function of composition at constant temperature and pressure. Rudolf and Cantow[14] studied the phase behaviors of polystyrene-polyisoprene (PS/PI), polystyrene-poly(methylphenyl-siloxane) (PS/PMPS), and polystyrene-poly(cyclohexyl methacrylate) (PS/PCHMA) blend systems using visual cloud point measurements and also by theoretical modeling. They observed through experimental data two types of phasediagrams: upper critical solution temperature (UCST) behavior for PS/PI and PS/PMPS systems and lower critical solution temperature (LCST) behavior for PS/PCHMA shown as in Figure 2-12 (b) and (c), respectively. Computations based on the Sanchez-Lacombe[15] equation of state theory and the theory developed by Flory[16], Prigoine[17] and Patterson[18] have shown qualitatively similar phase behavior and predicted that the phase diagrams shown in Figure 2-12 (d)-(f) were possible. In the next section, a mathematical form of the Gibbs free energy of mixing will be presented based on Flory-Huggins[19] lattice model.

2.4.1. Free Energy of Mixing

The free energy change at a given temperature is related to the enthalpy and entropy changes upon mixing by

(2-38) $$\Delta G_m = \Delta H_m - T\Delta S_m$$

The enthalpy and the entropy can be related to molecular properties, the interaction between molecules and the configurations of the molecules in the mixture, respectively. One of the two criteria for ideal solutions is athermal mixing ($DH_m = 0$) since it is assumed that the energy of interaction between a pair of solvent molecules, a pair of solute molecules, and a solvent-solute pair is the same. Consequently, it only remains for the entropy contribution to be calculated. The other criterion is that there is no volume change on mixing. This is satisfied if the solvent and solute molecules have the same size and have no specific interactions. Using Boltzmann's Law and counting the number of ways to arrange solvent and solute molecules in a given system, the mathematical expression for an ideal solution results:

$$\Delta G_m = -T\Delta S_m = kT\left(n_1 \ln N_1 + n_2 \ln N_2\right) < 0$$

$$\frac{\partial^2 \Delta G_m}{\partial n_i^2} > 0 \qquad \text{(2-39)}$$

where n_1 and n_2 are the number of molecules of solvent and solute, respectively, and N_1 and N_2 are their mole fractions, respectively. Since equation (2-39) satisfies both requirements for the stability of a homogeneous solution in all the compositions, components forming an ideal solution will always be completely miscible.

Polymer solutions, however, deviate from the ideal solution behavior even when the athermal condition is satisfied. This deviation is attributed to the fact that the size of a polymer molecule is much larger than that of a low molecular weight solvent. The entropy change per unit volume of a sytem produced by mixing a polymer in a solvent is much smaller than that when lower molecular weight species are mixed. Flory and Huggins independently developed a theory that describes the behavior of a polymer solution based on a lattice model.

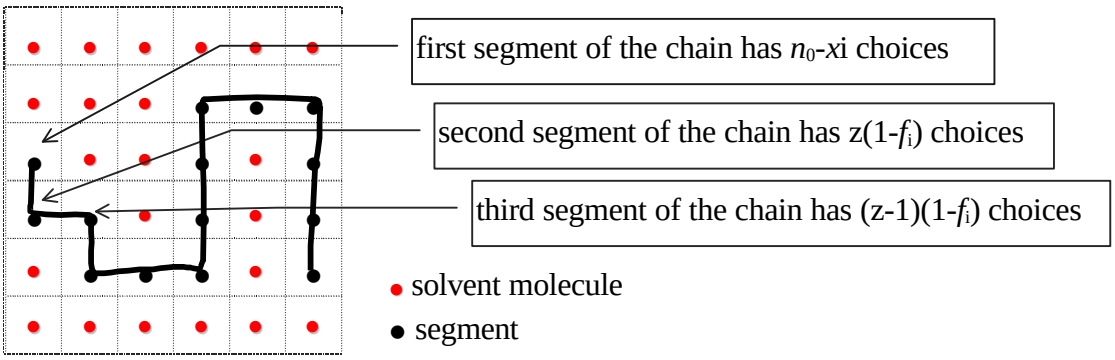

Figure 2-13. Two-dimensional lattice occupied by segments of a polymer chain and solvent molecules

2.4.2. Entropy of Mixing

In the description of polymer solutions, a conceptual lattice that consists of uniform cell size or sites is introduced to calculate the entropy associated with the number of unique arrangements of polymer and solvent molecules on this lattice. Each lattice site can be occupied by a solvent molecule or a segment of a polymer chain that has an equivalent size of a solvent molecule. Therefore, the number of lattice sites that a polymer molecule occupies is the ratio of the molar volume of the polymer molecule (V_2) to that of the solvent molecule (V_1), *i.e.* $x = V_2/V_1$. If the number of solvent and polymer molecules in the solution is n_1 and n_2, respectively, then the polymer molecules will occupy xn_2 lattice sites and the total number of lattice sites occupied by the solvent and polymer is $n_0 = n_1 + xn_2$.

Flory and Huggins considered three states to formulate the entropy change of mixing a polymer in a solvent. The first state is the perfectly ordered state of both polymer and solvent where the entropy is zero. The second state is one of disordered polymer chains which allow chains to be placed randomly on a lattice. The last state is a state in which the polymer chains are completely mixed with solvent molecules. Counting the number of ways to arrange the molecules at each state provides the entropy change of mixing a polymer in a solvent.

Calculating the number of ways to arrange polymer segments and solvent molecules on the lattice is different from the method used in the derivation of ideal solutions in that segments in a polymer chain must occupy x contiguous sites because of their connectivity. The number of ways to fill n_0 cells with n_1 identical solvent molecules and n_2 identical solute molecules can be expressed in the following form if we denote the number of ways to fill a polymer chain i into the lattice as w_i:

$$\Omega(n_1, n_2) = \frac{1}{n_2!}\prod_{i=1}^{n_2} w_i \qquad (2\text{-}40)$$

Let us think about calculation of w_{i+1}. The number of cells available to the first segment of chain i+1 is n_o-xi since xi lattice sites are already occupied by i chains in the lattice. The first segment restricts the number of cells available to the second segment of chain i+1. Because the second segment is bonded to the first one, the former can only be placed on an adjacent neighbor cell to the latter. Let us denote the number of neighbor cells to a segment as coordination number z. The previous chains may already take some of these z cells. According to mean field approximation, the fraction of occupied cells in z cells is assumed to be equal to the fraction of cells occupied by the previous i chains in n_0 cells, i.e., $f_i = \frac{xi}{n_0}$. Then the number of ways to put the second segment of chain i+1 is z (1-f_i), where 1-f_i is the fraction of unoccupied cells. The third or later segments have z-1 cells available because the previous adjacent segment already occupies one cell in the z cells (see Figure 2-13). Therefore, the number of ways for the third or later segments is (z-1)(1-f_i). Since the number of segments in a single chain is x, w_i is expressed as:

$$
\begin{aligned}
w_{i+1} &= (n_0 - xi)z(1 - f_i)[(z-1)(1-f_i)]^{x-2} \\
&\approx (n_0 - xi)[(z-1)(1-f_i)]^{x-1} \\
&\approx (n_0 - xi)^x \left(\frac{z-1}{n_0}\right)^{x-1}
\end{aligned} \tag{2-41}
$$

where the factor z appeared in the first step is approximated to z-1 in the second step of the above equation and 1-f_i is replaced by $\frac{n_0 - xi}{n_0}$. Therefore, substitution of w_i in equation (2-40) with equation (2-41) leads to

$$
\begin{aligned}
\Omega(n_1, n_2) &= \frac{1}{n_2!}\prod_{i=1}^{n_2} w_i = \frac{1}{n_2!}\prod_{i=0}^{n_2-1} w_{i+1} \\
&= \frac{1}{n_2!}\prod_{i=0}^{n_2-1}(n_0 - xi)^x \left(\frac{z-1}{n_0}\right)^{x-1}
\end{aligned} \tag{2-42}
$$

We need to evaluate $\ln\Omega$ by taking the logarithm of both sides of equation (2-42). Using some algebraic operations leads to

$$
\ln\Omega = \sum_{i=0}^{n_2-1} x\ln(n_0 - xi) + n_2(x-1)\ln\left(\frac{z-1}{n_0}\right) - \ln n_2! \tag{2-43}
$$

The summation of the first term in equation (2-43) may be replaced by integration and n_2-1 may be approximated to n_2 if n_2 is sufficiently large. That is,

$$
\begin{aligned}
\sum_{i=0}^{n_2-1} x\ln(n_0 - xi) &\approx \int_0^{n_2} x\ln(n_0 - xi)di \\
&= \int_0^{n_2 x} \ln(n_0 - xi)d(xi) \\
&= n_1 \ln\frac{n_0}{n_1} + xn_2 \ln n_0 - xn_2
\end{aligned} \tag{2-44}
$$

Therefore, substitution of equation(2-44) into equation (2-43) and use of the Stirling's approximation yields

$$
\begin{aligned}
\ln\Omega &\approx n_1 \ln\frac{n_0}{n_1} + xn_2 \ln n_0 - xn_2 + n_2(x-1)\ln\left(\frac{z-1}{n_0}\right) - \ln n_2! \\
&= n_1 \ln\frac{n_0}{n_1} + n_2 \ln\frac{n_0}{n_2} + n_2(x-1)\ln\left(\frac{z-1}{e}\right)
\end{aligned} \tag{2-45}
$$

Consequently, the configurational entropy change by mixing the perfectly ordered polymer and the pure solvent is then given by

$$S_c = k \ln \Omega \approx k\left[n_1 \ln \frac{n_0}{n_1} + n_2 \ln \frac{n_0}{n_2} + n_2 (x-1) \ln\left(\frac{z-1}{e} \right) \right] \tag{2-46}$$

because the entropies of the perfectly ordered polymer and the pure solvent are zero.

Since there are no solvent molecules, the entropy change for the transition of a perfectly ordered polymer to the amorphous state is obtained from substitutions of n_1=0 and n_0= xn_2 into equation (2-43):

$$S_{am} \approx k\left[n_2 \ln x + n_2 (x-1) \ln\left(\frac{z-1}{e} \right) \right] \tag{2-47}$$

Therefore, the entropy change of mixing an amorphous polymer in a solvent is obtained from equations (2-46) and (2-47)

$$\begin{aligned} \Delta S_m^* &= S_c - S_{am} - S_1 \\ &= k\left[n_1 \ln \frac{n_0}{n_1} + n_2 \ln \frac{n_0}{x n_2} \right] \\ &= -k\left[n_1 \ln f_1 + n_2 \ln f_2 \right] \end{aligned} \tag{2-48}$$

where f_1 and f_2 are the volume fractions of solvent and solute, *i.e.*

$$\left.\begin{aligned} f_1 &= \frac{n_1}{n_0} = \frac{n_1}{n_1 + x n_2} \\ f_2 &= \frac{x n_2}{n_0} = \frac{x n_2}{n_1 + x n_2} \end{aligned}\right\} \tag{2-49}$$

2.4.3. Enthalpy of mixing:

In the derivation of the entropy change from the lattice theory, it was assumed that the segment locating process is purely statistical and the enthalpic and entropic parts of the free energy can be treated separately and are additive[20]. The contribution due to the differences in solvent-solvent, segment-segment, and segment-solvent interactions should be incorporated in the enthalpy of mixing. Since the attractive force between uncharged molecules decreases rapidly with the distance of separation (~ r^{-6}), it is reasonable to consider that only the interaction between neighboring lattice sites is significant. Denoting 1 as solvent, 2 as polymer segment and [1,1], [2,2] and [1,2] as pairs of neighboring solvent-solvent, segment-segment and segment-solvent, respectively, the energy change for the formation of an unlike contact, Dw_{12}, is given by:

$$\frac{1}{2}[1,1]+\frac{1}{2}[2,2]=[1,2]$$

(2-50)

$$\Delta w_{12} = w_{12} - \frac{1}{2}(w_{11} + w_{22})$$

where w_{11}, w_{22}, and w_{12} are the solvent-solvent, segment-segment, and segment-solvent interactions, respectively. Letting p_{12} be the number of contacts between unlike species in solution, the heat of mixing from the pure components can be written as

(2-51) $$\Delta H_m = p_{12}\Delta w_{12}$$

In order to evaluate an average value of p_{12}, we will consider the number of the nearest cells which contact with x segments of a polymer molecule. Since each segment in the middle chain has coordination number z and two cells are occupied by segments before and after it from the same chain, the number of nearest cells around x-2 segments (the two terminal units are excluded) is (z-2)(x-2). For the two terminal segments, because there are z-*1* nearest cells around a terminal unit, 2(z-*1*) nearest cells are present around terminal segments of the molecule. Therefore, the number of the nearest cells around a single polymer chain is (z-*2*)x+2. Among the (z-*2*)x+2 nearest cells, some cells will be occupied by solvent (unlike) and some will be occupied by the other polymer chains (own kind). It is assumed that the mean field approximation holds, indicating that the probability that a solvent occupies a nearest cell around the polymer chain is equal to the volume fraction f_1 of solvent in the solution. Then the total number of contacts, p_{12}, for n_2 polymer chains is

(2-52) $$p_{12} = n_2((z-2)x+2)f_1 \approx n_2 zx f_1 = n_1 z f_2$$

The approximation to zx in the above equation is valid for large z and x. Therefore, substitution of equation (2-52) into equation (2-51) yields the heat of mixing

(2-53) $$\Delta H_m = z\Delta w_{12} n_1 f_2$$

Equation (2-53) can be modified to take into account the effect of a solvent molecule with x_1 segments (polymer solvent) on the enthalpy of mixing, *i.e.*

(2-54) $$\Delta H_m = z\Delta w_{12} x_1 n_1 f_2 = kTc_1 n_1 f_2$$

where the Flory-Huggins interaction parameter, c_1, of a polymer and a solvent is defined as

(2-55) $$c_1 = \frac{z\Delta w_{12} x_1}{kT}$$

When a small solvent molecule is used, the degree of polymerization of the solvent molecule, x_1 is one. Therefore, the total free energy is obtained by the combination of equations (2-48) and (2-54)

$$\Delta G_m = \Delta H_m - T\Delta S_m \qquad (2\text{-}56)$$
$$= kT(n_1 \ln f_1 + n_2 \ln f_2 + c_1 n_1 f_2)$$

In the derivation of the enthalpy of mixing, pair interactions were assumed to contribute to enthalpy not to entropy. However, because the segment locating process is also affected by the number of pair contacts in the solution as for the heat change, a change in entropy should be taken into account. Therefore, the interaction energy, Dw_{12}, may be regarded as a standard state free energy change for the process and separated into the enthalpic and entropic terms. That is,

$$\Delta w_{12} = \Delta w_h - T\Delta w_s \qquad (2\text{-}57)$$

Substitution of equation (2-57) into equation (2-55) separates the c_1 parameter into entropic and enthalpic parts:

$$c_1 = \frac{c_h}{T} + c_s = \frac{z\Delta w_h}{kT} - \frac{z\Delta w_s}{k} \qquad (2\text{-}58)$$

When equation (2-54) is substituted with equation (2-58) and combined with equation (2-45), the free energy of mixing can be written as:

$$\Delta G_m = \Delta H_m - T\Delta S_m \qquad (2\text{-}59)$$
$$= kT(n_1 \ln f_1 + n_2 \ln f_2 - \frac{z\Delta w_s}{k} n_1 f_2) + z\Delta w_h n_1 f_2$$

The first two terms in equation (2-59) arise from the configurational free energy change, and this quantity does not represent the total change entropy of mixing. Due to the entropic term in the interaction parameter, the entropy change of mixing for an actual polymer solution is smaller than expected by configurational entropy change. Nevertheless, the expression for the free energy of mixing in equation (2-59) is not changed by this consideration. The entropy and the enthalpy of mixing can be obtained from equation (2-56) by using the standard thermodynamic relationship: $dG = Vdp - SdT$ and the Gibbs-Helmholtz equation, $\Delta H_M = -T^2 \left(\frac{\partial \left(\Delta G_M / T \right)}{\partial T} \right)_p$. Thus,

$$\Delta S_m = -\left(\frac{\partial \Delta G_m}{\partial T} \right)_p \qquad (2\text{-}60)$$
$$= -\left(\frac{\partial kT\left(n_1 \ln f_1 + n_2 \ln f_2 + c_1 n_1 f_2\right)}{\partial T} \right)_p$$
$$= -k\left(n_1 \ln f_1 + n_2 \ln f_2 + \frac{\partial c_1 T}{\partial T} n_1 f_2 \right)$$

and

$$\Delta H_m = -T^2\left(\frac{\partial k\left(n_1 \ln f_1 + n_2 \ln f_2 + c_1 n_1 f_2\right)}{\partial T}\right)_p$$
$$= -kT^2 n_1 f_2\left(\frac{\partial c_1}{\partial T}\right) \qquad \text{(2-61)}$$

If the χ_1 parameter contains no entropic contribution, $\frac{\partial c_1 T}{\partial T} = 0$ since $c_1 = \frac{z\Delta w_h x_1}{kT}$. Therefore, the third term in equation (2-60) is zero and the entropy of mixing becomes the configurational entropy of mixing, $\Delta S_m = \Delta S_m^*$. Also DH_m reduces to the previous expression equation (2-54). That is,

$$\Delta H_m = -kT^2 n_1 f_2 \frac{z\Delta w_h x_1}{k}\left(\frac{\partial T^{-1}}{\partial T}\right)$$
$$= z\Delta w_h x_1 n_1 f_2 \qquad \text{(2-62)}$$
$$= kTc_1 n_1 f_2$$

The Flory-Huggins lattice model has been useful and provided a fundamental basis to develop modeling for polymer solution behavior mainly through its simplicity. However, the theory is unable to describe the behavior of dilute polymer solutions particularly because of the assumptions made for the simplicity on the derivation of the theory. In the derivation of entropy, it was assumed that the configurations available to the chain are unaffected by intermolecular interactions. Such interactions will further reduce entropy from the value of configurational entropy estimated by equation (2-46). Furthermore, the entropy of the disordered state, S_{am}, overestimates the value of the actual pure polymer since many configurations in the solution do not exist in the disordered state. Thus, the entropy change estimated from the Flory-Huggins theory will be larger than the actual polymer solution. The polymer chains were assumed to be flexible to occupy any neighboring sites available. Even if there are some empty sites around a segment, because of limited flexibility in the real chain, a segment may not occupy the free sites. The c_1 parameter was originally assumed to be independent of temperature and composition. However, experimental evidence has demonstrated that the c_1 parameter depends on the composition[21,22].

In the derivation, some equations were simplified with the assumptions of large n_2 and x and mean field approximation and thus the resulting equation for entropy change is suitable for a concentrated solution. It does not describe behaviors of a dilute solution due to non-uniformity of the solution. Flory and Krigbaum[23] developed thermodynamic relationships based on an excluded volume concept to overcome the limitations of the lattice theory. It is applicable to dilute solutions of heterogeneous high molecular weight

polymers. When the excluded volume vanishes (q condition), the theory becomes identical to the Flory-Huggins lattice model.

Another approach for describing phase behaviors of polymer-polymer blends is using an equation of state. The principles of this theory are developed by Prigogine[17] based on statistical mechanics. Flory[16] and Patterson[18] extended his formalism to the polymer solution theory. This theory predicted the lower critical solution temperature behaviors, which are often observed in polymer-polymer blends (See Figure 2-9 (c)).

2.4.4. Chemical Potentials

The chemical potential m_i of a component in solution relative to its chemical potential m_i^o in the pure state provides the basis of calculating the spinodals and binodals for a system of two polymer components obeying the Flory-Huggins theory. The first step is to calculate the partial molar free energy from equation (2-56) to find the binodals and spinodals at constant temperature and pressure. The chemical potential is obtained by differentiation of the free energy with respect to the number of moles of solvent, m_i (= n_i/N_A where N_A is Avogadro's number).

$$\begin{aligned}\Delta m_1 &= m_1 - m_1^o = \frac{\partial \Delta G_m}{\partial m_1} = N_A \frac{\partial \Delta G_m}{\partial n_1} \\ &= N_A \frac{\partial}{\partial n_1}\left[kT\left(n_1 \ln f_1 + n_2 \ln f_2 + n_1 c_1 f_2\right)\right] \\ &= RT\left(\ln f_1 + n_1 \frac{\partial \ln f_1}{\partial n_1} + n_2 \frac{\partial \ln f_2}{\partial n_1} + c_1 f_2 + n_1 c_1 \frac{\partial f_2}{\partial n_1}\right)\end{aligned} \tag{2-63}$$

Since $f_2 = \frac{xn_2}{n_1 + xn_2}$ and $f_1 = \frac{n_1}{n_1 + xn_2} = 1 - f_2$, with using the chain rule,

$$\begin{aligned}\frac{\partial f_2}{\partial n_1} &= -\frac{xn_2}{\left(n_1 + xn_2\right)^2} = -\frac{f_1 f_2}{n_1} \\ \frac{\partial f_1}{\partial n_1} &= -\frac{\partial f_2}{\partial n_1} = \frac{f_1 f_2}{n_1} \\ \frac{\partial \ln f_2}{\partial n_1} &= \frac{1}{f_2}\frac{\partial f_2}{\partial n_1} = -\frac{f_1}{n_1} \\ \frac{\partial \ln f_1}{\partial n_1} &= \frac{1}{f_1}\frac{\partial f_1}{\partial n_1} = \frac{f_2}{n_1}\end{aligned} \tag{2-64}$$

Therefore, equation (2-63) becomes

$$\Delta m_1 = RT\left(\ln f_1 + f_2 - n_2 \frac{f_1}{n_1} + c_1 f_2 - c_1 f_1 f_2 \right)$$

$$= RT\left(\ln(1-f_2) + \left(1 - \frac{n_2 f_1}{n_1 f_2}\right) f_2 + c_1 f_2 (1-f_1) \right) \quad \text{(2-65)}$$

$$= RT\left(\ln(1-f_2) + \left(1 - \frac{1}{x}\right) f_2 + c_1 f_2^2 \right)$$

Similarly,

$$\Delta m_2 = RT\left(\ln f_2 + (1-x)(1-f_2) + x c_1 (1-f_2)^2\right) \quad \text{(2-66)}$$

A binary system with two phases is at equilibrium if the chemical potentials of a component in both phases are the same, *i.e.*

$$(\Delta m_1)_A = (\Delta m_1)_B \text{ and } (\Delta m_2)_A = (\Delta m_2)_B \quad \text{(2-67)}$$

where *A* and *B* indicate two phases and subscripts 1 and 2 denote the components. Solving equation (2-67) for a composition provides an equilibrium (binodal) curve as a function of temperature, relative size of polymer to solvent, and the interaction parameter, c_1.

Substitution of equation (2-49) into equation (2-56) leads to

$$\overline{\Delta G_M} = \frac{N_A \Delta G_m}{(n_1 + x n_2)} = RT\left(f_1 \ln f_1 + \frac{f_2}{x} \ln f_2 + c_1 f_1 f_2 \right) \quad \text{(2-68)}$$

where $\overline{\Delta G_M}$ denotes the free energy of mixing per mole of sites. Figure 2-14 shows the free energy curves as a function of volume fraction of polymer at different temperatures, which were computed using equation (2-68) with x = 10 and χ_1 = 0.336 + 69.457/T (K). Solving equation (2-67) at a given temperature yields two conjugate binodal points. The binodal curve is obtained by connecting binodal points at different temperatures. Finding the compositions that correspond to the inflection points ($\frac{\partial^2 \overline{\Delta G_M}}{\partial f_2^2} = 0$) for each free energy curve gives spinodal points. The spinodal curve is created from the inflection points obtained from the free energy curves at different temperatures. The critical point is the point where the spinodal and binodal curves have a common tangent. Therefore, a phase diagram is obtained by plotting the binodal and spinodal curves in the volume fraction and temperature space. The bottom plot in Figure 2-14 shows an upper critical solution temperature behavior where the system is completely miscible above the critical temperature.

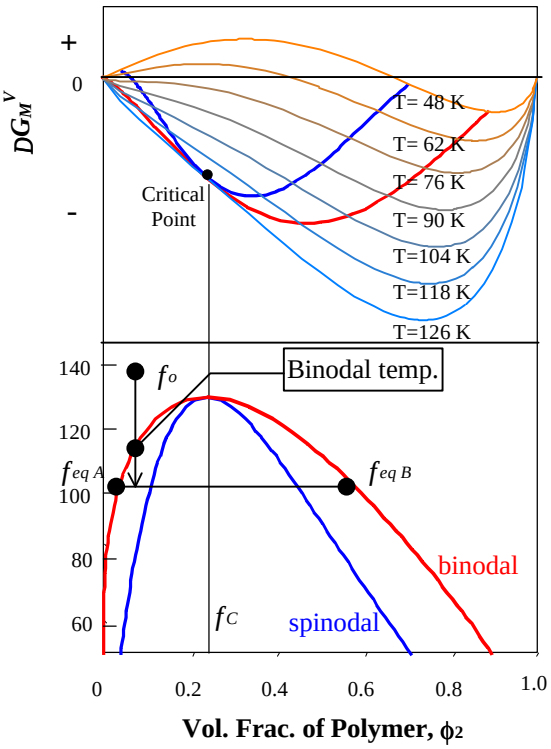

Figure 2-14. Free energy curve as a function of volume fraction at different temperatures (top) and phase diagram (bottom) computed from equation (2-68).

Since x is the ratio of size of a polymer molecule to that of a solvent, an increase in x means an increase in molecular weight or molar volume of the polymer. The effect of molecular weight on the phase behavior is shown in Figure 2-15. The critical composition of polymer shifts from 0.5 to lower composition and the critical temperature increases with an increase in molecular weight. When the molecular weight (size) of polymer is the same as that of solvent, the binodal and spinodal curves are symmetrical with respect to the composition of 0.5. As the difference between the polymer and solvent molecular weights increases, the curves become asymmetrical. Note that the polymer-rich metastable region increases and solvent-rich metastable region decreases as the molecular weight of polymer increases. This implies that a binary blend whose molecular weights are significantly different will have a greater chance to spinodally decompose rather than to nucleate and grow even when the composition of the high molecular weight species are relatively low. This will be discussed further in chapter 6.

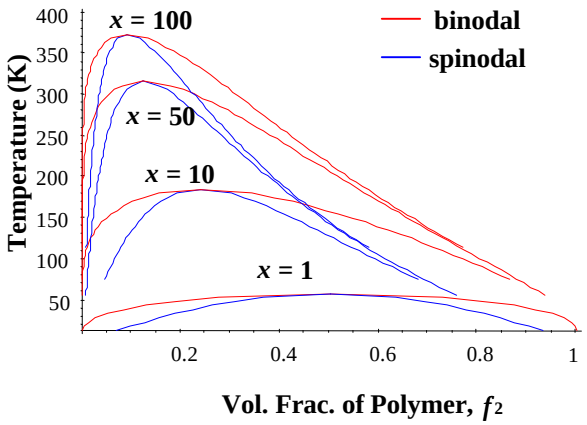

Figure 2-15. Theoretically predicted dependence of phase behavior on molecular weight of polymer. $c_1 = 0.35 + 95/T(K)$.

2.5. KINETICS OF PHASE SEPARATION

2.5.1. Spinodal Decomposition

Spinodal decomposition is a kinetic process of generating spontaneously and continuously a new phase interconnected with the parent phase, which has been in a thermodynamically unstable state. A necessary condition for spinodal decomposition is that the parent phase must be in the unstable region. Thus, the composition of the system must be within the two spinodal compositions at the temperature of phase separation.

Once it is in the unstable state, small sinusoidal fluctuations of composition cause a new phase to be produced. The clustering of the new phase, in turn, makes the amplitude of the fluctuation bigger and the molecules of both components are moving toward the equilibrium (binodal) compositions, one of which is lower in concentration than the parent concentration. The concentration of the other phase will be higher than that of the parent phase as necessitated by mass balance. This spinodal growth process is illustrated in Figure 2-16. For simplicity, it shows the variation of only one sinusoidal fluctuation with time. An actual description of the composition fluctuations in a solution is a superposition of sine waves that are randomly oriented in space and amplitude[24]. While the amplitudes of the composition fluctuations keep increasing towards the equilibrium compositions, the wavelength of the fluctuations is fixed.

In the growth process, the phases exhibit an interwoven, interconnected, or co-continuous structure. Once parent and new phase have reached their equilibrium composition, the system tends to minimize the surface free energy by minimizing the interfacial area. Because a sphere has the minimum surface area to volume ratio, the co-continuous structure starts to coarsen or ripen toward the shape of spheres through a viscous flow mechanism. Due to high viscosities of both phases, the spherically dispersed

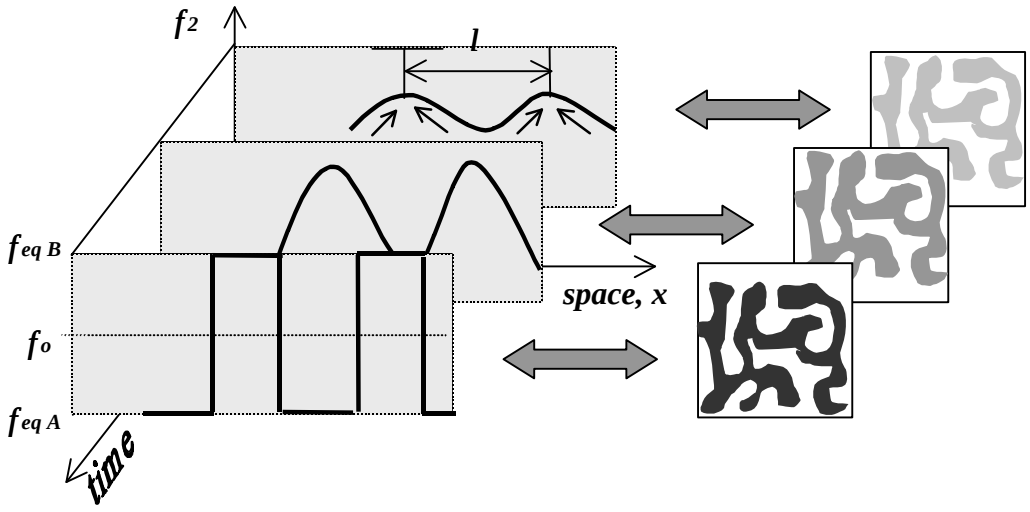

Figure 2-16. Schematic illustration of early stage of spinodal decomposition. The amplitude of fluctuation increases but the wavelength is fixed.

structure may not result. If the viscosity were sufficiently low, density differences of both phases would cause dispersed phases to gather on top or bottom of the system and concentrate the phases in the region. Because a large sphere has less surface area than two or more small spheres with the same total volume, the dispersed spheres will coagulate and eventually result in two layers, one on top of the other.

Thermodynamic theories of non-homogeneous solutions have been developed by Cahn[24] and Debye[25]. Cahn and Hilliard were able to predict the connectivity of phases using their theory. They concluded that the kinetics of the initial stages and the resulting morphology are controlled entirely by the magnitude of the second derivative of the free energy density of homogeneous material ($\frac{\partial^2 G'}{\partial f_1^2}$), the gradient energy coefficient (K) and diffusion coefficient. These values describe the kinetics of spinodal decomposition. The wavelength was given by

$$l_m = \frac{2p}{b_m} = 2\sqrt{2}p\left[-\left(\frac{1}{2K}\right)\frac{\partial^2 G'}{\partial f_1^2}\right]^{-\frac{1}{2}} \qquad (2\text{-}69)$$

where the second derivative of the free energy density has negative values in the spinodal region.

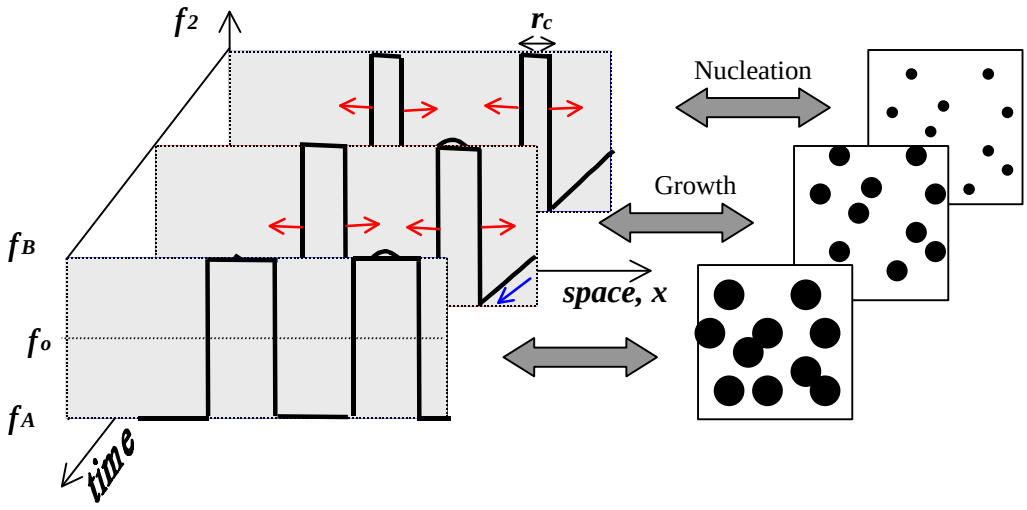

Figure 2-17. Schematic illustration of nucleation and growth mechanism. $f_{eq\,A}$ and $f_{eq\,B}$ are the equilibrium compositions corresponding to the matrix phase and the dispersed phase, respectively, and r_c is the critical nuclei size.

2.5.2. Nucleation and Growth Mechanism

Nucleation is a kinetic process generating nuclei of a new phase with size r_c from the parent phase (f_o in Figure 2-14 and Figure 2-17). By generating new phase, the mixture of nuclei phase and the parent phase has lower free energy than that of the old parent phase. The metastable nature of the parent phase requires composition fluctuations large enough to form stable nuclei. As shown in Figure 2-14, if the system is quenched from a stable temperature to the binodal temperature, the phase is at an equilibrium composition and the phase separation would not occur. In order for a undercooling is required to put the system in a metastable state.

Even though generating a new stable phase from the metastable parent phase reduces the free energy of the system, the generating of a new interface between phases increases the free energy. If the system is isotropic and the free energy change for the formation of a new phase is denoted as DG_N, then the new phase will be a sphere and the total free energy change of the system may be given by

$$\Delta G(r) = \frac{4}{3}pr^3\Delta G_N + 4pr^2g \qquad (2\text{-}70)$$

where g is the surface free energy of the interface between the new phase and parent phase. Since the formation of a new phase is favorable, DG_N is negative. A plot of the total free energy as a function of the radius of the spherical phase is presented in Figure 2-18, where there is a critical size (r_c) of a new phase. A new phase particle smaller than

the critical size will redissolve in the parent phase and the particles larger than the critical size will remain as nuclei. Therefore, the activation energy for the nucleation (DG_C) is taken to be the maximum of the total free energy, which can be found by the first derivative of equation (2-70) with respect to radius r. Thus

$$r_c = -\frac{2g}{\Delta G_N} \text{ and } \Delta G_C = \frac{16pg^3}{3\Delta G_N^2} \quad \text{(2-71)}$$

The probability of the presence of a nucleus of a given size is assumed to follow the Boltzman distribution and is therefore proportional to exp(-DG_C/kT) at constant temperature and pressure. Also it is assumed that there is no stress built by the volume change during the process. With these assumptions, the rate of nucleation, that is, the number of nuclei per unit volume per unit time generated from the homogeneous parent phase can be calculated as:

$$\frac{dN(r_c)}{dt} = N_0 D \exp\left(-\frac{\Delta G_C}{kT}\right) \quad \text{(2-72)}$$

where $N(r_c)$ is the number density of nuclei with critical radius r_c, D is the diffusion coefficient of component 2 in component 1[26].

Once those nuclei are formed, the parent phase reduces its composition with a decrease in free energy and nuclei grow. Figure 2-17 illustrates the growth process. If a nucleus of composition f_B is formed, the composition of the matrix phase in the vicinity of that nucleus would be f_A. However, the composition of the matrix phase far away from the nucleus remains essentially the composition of the parent phase, f_o, which is in a higher free energy state and higher concentration of component 2 than the equilibrium

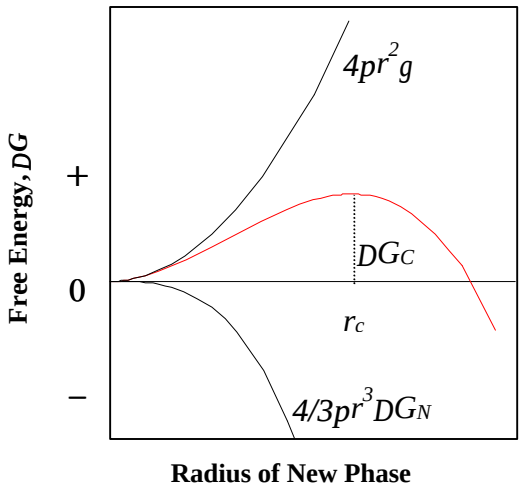

Figure 2-18. Formation of spherical nuclei of a new phase from the parent phase.

composition f_A. Therefore, the molecules within the parent phase would diffuse to the lower equilibrium composition f_A. At the expense of lowering concentration in the parent phase, the nuclei can grow and a spherically dispersed two phase system results. Depending on the particle density, the growing particles may coalesce with each other.

In contrast to the spinodal decomposition, phase separation by nucleation and growth begins with formation of particles and they may coalesce to form an interconnected morphology. Therefore, both mechanisms may give the same morphology at the end of phase separation. However, since the spinodal decomposition requires the initial composition of the parent phase to be close to the critical composition and the spinodal region is surrounded by the binodal region, the volume fraction of a minor phase for spinodal decomposition should be greater than for nucleation-and-growth.

2.6. FRACTURE TOUGHNESS (K_{IC} AND G_{IC}) AND TOUGHNENING MECHANISM

2.6.1. Deformation of Polymers

Polymers, in general, response to an applied stress by several types of deformation, e.g., elastic, viscoelastic, plastic, or hysterisis, depending on their structure and the testing conditions. The mechanical behavior of elastic materials obeys Hooke's law that the stress is proportional to the strain. Polymers only tend to obey Hooke's law at considerably small strains. At high strain, high temperature or slow testing rate, the behavior of polymers is toward that of viscous liquids. Polymers are therefore considered viscoelastic as they display both viscous and elastic behaviors. Shear yielding and crazing may be two important plastic deformation mechanisms often observed in the fracture of polymers.

2.6.1.1. Shear Yielding

Shear yielding is a material response to an applied shear stress by plastic deformation through the translation of chain molecules past each other with keeping the volume of specimen essentially constant and leads to a permanent change in shape. The molecules that are well anchored at entanglements in the structure are not broken to any great extent during deformation. Shear yielding in glassy polymer can occur through highly localized shear bands or diffuse shear deformation zone as shown in Figure 2-19 (12) and (13). Even though a polymer globally exhibits brittle crack propagation (linear elastic fracture), localized viscoelastic and plastic fracture can occur in the vicinity of the crack tip. Shear yielding and shear banding is often considered as one of the most plausible mechanisms for toughening.

2.6.1.2. Crazing

Crazes are microcracks bridged by fibrils and their formation is accompanied by an increase in specimen volume unlike shear yielding[27]. Crazes can form ahead of crack tip

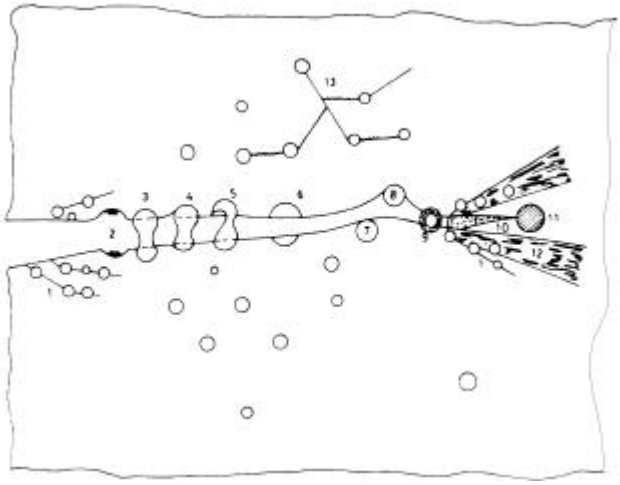

Figure 2-19. Crack Toughening mechanisms in toughened polymers[28].

and the crack propagates with crazes. Crazes are generally nucleated at imperfections and require the presence of a hydrostatic or dilatational component of the stress tensor. Multiple crazing can lead to general yielding and acts as toughening mechanism in polymers. Alternatively, highly localized crazing leads to craze breakdown, crack initiation and subsequent brittle failure. Crazing is more commonly found to be the main cause of failure in brittle thermoplastics.

2.6.2. Definition of Fracture Toughness

When a material is in a severe loading condition, it is broken to parts creating new surfaces. Its maximum load to break depends on its intrinsic property as well as its testing size, shape and loading conditions such as rate, temperature, *etc*. It is desirable to define a parameter that is a measure of ability to resist fracture and independent of sample geometry and size. The toughness of a material may be defined as energy per unit volume required for fracture. This quantity is readily measured by integrating the stress-strain curve up to the strain at break. However, it is unavoidable for a sample to include flaws, scratches, microvoids, microcracks and *etc*. The applied stress concentrates on those inherent artifacts and the crack propagates through part of them. Therefore, this definition of toughness does not tell the criteria that fracture occurs. Two main definitions for the fracture toughness have been widely used: critical strain energy release rate and critical stress intensity factor. Critical strain energy release rate, G_C, is defined as the critical energy required for propagating a crack per unit area. If a work done on a specimen exceeds the critical energy, fracture occurs. The critical stress intensity factor, K_C, defines the critical value of a material that fracture occurs when a applied stress intensity factor on the material is greater than the critical value. The stress intensity factor, K, is a measure of applied stress associated with crack size.

2.6.2.1. Critical Strain Release Rate G_C

Critical strain energy release rate is based on the energy criterion arising from Griffith's early work. He supposed that critical failure occurred when the growth of the crack releases sufficient energy to overcome the increase in free energy by creating two new surfaces, which is generated by the crack propagation. Therefore, the external work done on the system, *F*, must be equal to or greater than increase in the internal energy of the system, *U*, plus energy for creation of two new surfaces, 2*Ag*, where *A* is the new surface area created by the crack growth and *g* is the surface free energy. Then for the infinitesimal increase of crack, *da*, it may be written

$$\frac{\partial(F-U)}{\partial a} \geq \frac{\partial 2Ag}{\partial a} = 2bg \qquad (2\text{-}73)$$

where *b* is the thickness and thus $A = ab$. However, the energy required for fracture of a material sometimes exhibits much greater, even thousand times, than twice of its surface free energy. One of the reasons for this discrepancy is that fracture of a material includes breaking covalent bonding in addition to the rupture of secondary bonds for which energy per unit area corresponds to 2*g*. The energy required for bond rupture per unit area is referred to as the intrinsic fracture energy, G_o. This intrinsic fracture energy does not explain the discrepancy whole particularly for polymers. It is due to the fact that localized viscoelastic or plastic deformation in the vicinity of the crack tip or elsewhere in the sample dissipates energy when fracture occurs even for the brittle polymers[27].

The critical strain energy release rate is, therefore, defined to include the intrinsic fracture energy (G_o) and the energy dissipated by the viscoelastic or plastic deformation in the vicinity of the crack tip. Hence, the term 2*g* in equation (2-73) is replaced with G_C. That is

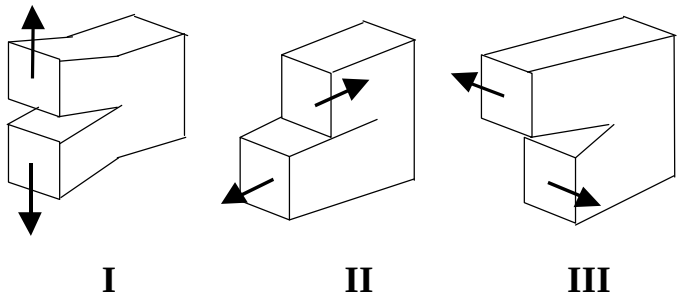

Figure 2-20. Different modes for crack propagation: Mode I: tensile opening, mode, Mode II: sliding or in-plane shear mode, Mode III: tearing or anti-plane shear mode.

$$\frac{1}{b}\frac{\partial(F-U)}{\partial a} \geq G_C \tag{2-74}$$

There are the three fundamental modes of crack propagation depicted in Figure 2-20, all of which may be superposed in the general case of crack loading. Experimentally the crack is usually controlled to follow only one of the three modes. Therefore, G_{IC} indicates the critical strain energy release rate measured in mode I. The most frequently used mode is the tensile crack opening, *i.e.* mode I.

2.6.2.2. Critical Stress Intensity Factor

Irwin[29] studied fracture behavior using the formalism by Westergaard[30] and found that the stress field around a sharp crack in a linear elastic material can be defined by a parameter which is called as the stress intensity factor, *K*. When an isotropic, elastic, and infinitely thin plate containing a infinitely sharp crack size of *a* is deformed uniaxially with stress σ_0 (Figure 2-21), the components of the stress tensor in a volume element in distance *r* and angle θ from the crack tip was computed to give the following solutions:

$$\begin{aligned} s_x &= s_0 \frac{\sqrt{pa}}{\sqrt{2pr}} \cos\frac{q}{2}\left(1-\sin\frac{q}{2}\sin\frac{3q}{2}\right) \\ s_y &= s_0 \frac{\sqrt{pa}}{\sqrt{2pr}} \cos\frac{q}{2}\left(1+\sin\frac{q}{2}\sin\frac{3q}{2}\right) \\ t_{xy} &= s_0 \frac{\sqrt{pa}}{\sqrt{2pr}} \sin\frac{q}{2}\cos\frac{q}{2}\cos\frac{3q}{2} \end{aligned} \tag{2-75}$$

where σ and τ represent tensile and shear stresses, respectively. Equation (2-75) indicates that the stress at the crack tip (r = 0) goes to infinity. Then a reasonable criterion for the fracture cannot be made using the stress. Therefore, Irwin introduced the stress intensity factor K_I that can give the criterion for fracture in mode I. He set the stress intensity factor as

$$K_I = s_0\sqrt{pa}Q \tag{2-76}$$

where *Q* is the geometry factor that corrects the assumption of a infinite thin plate in the derivation of equation (2-75). Similarly the critical stress intensity factor can be defined as

$$K_{IC} = s_C\sqrt{pa}Q \tag{2-77}$$

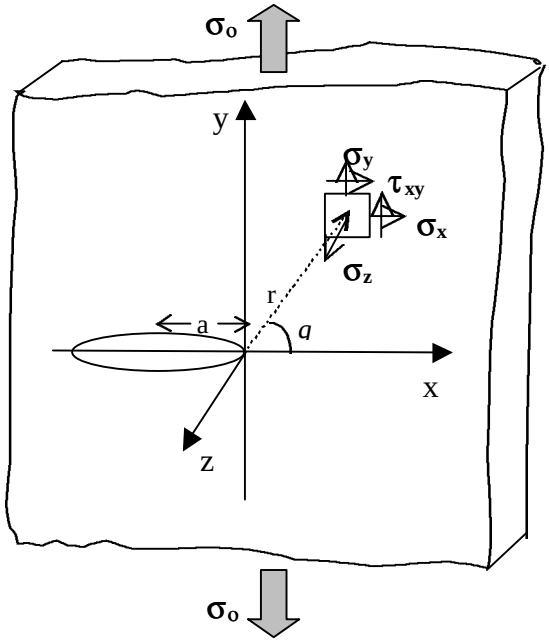

Figure 2-21. Stress analysis near a sharp crack tip of an isotropic and elastic plate

Therefore, the criterion for the fracture is

(2-78) $K_I \geq K_{IC}$

The critical stress intensity factor is a material property that characterizes the intensity of the stress field ahead of the crack tip. The geometry factor can be found in several handbooks[31-33] for many standard geometries.

2.6.3. Toughened Thermosets

Epoxies are one of important thermosetting materials for high performance adhesives and composites matrix applications[34]. These highly crosslinked networks combine good thermal and mechanical properties with outstanding adhesive properties. However, their inherent brittle behavior limits them for wide applications requiring high impact properties and high fracture strengths. Initial attempts to improve ductility or impact strength for epoxy thermoset systems employed various levels of "reactive " or "non-reactive plasticizers" based on long chain epoxidized glycols and dimer acids[35]. However, the use of most of these modifiers reduced thermal stability and strengths.

Traditional toughness modifiers such as carboxyl terminated butadiene acrylonitrile copolymer rubbers (CTBN) have been widely used to improve toughness since the frontier work by Sultan and McGary[36-41]. However, such improvements were achieved at the expense of high temperature performance. This has been attributed to the low glass transition temperature of the unsaturated rubbery phase that lowers the end-use

temperature and the modulus of the resulting networks. The amount of rubber incorporated is limited to the maximum of about 20 % wt for this reason.

A binary phase morphology consisting of relatively small (0.1- 5 μm) rubbery particles dispersed in and bonded to epoxy is generated. The toughness of the resulting networks was influenced by the properties of the pure epoxy (cross link density), morphology of dispersed particle phase, levels of interfacial adhesion, the initial composition and properties of the toughener[39]. Significant improvements (10 folds or so for K_{IC}) have been reported only for the case of lightly crosslinked epoxies[42]. Even though extensive studies have been done on the rubber toughened or thermoplastic toughened thermosets, the primary cause to improve the fracture toughness for the modified thermosets has not been firmly established due to the experimental difficulties to control the factors independently.

Disadvantage of CTBN and ATBN modified thermoset networks is that the presence of unsaturated bonds in the butadiene rubber may act as undesirable sites in oxidative and high temperature environments. The use of functionally terminated polysiloxanes as a toughener of bisphenol-A type of epoxy resins has also been reported[43-45]. Siloxane elastomers provide an attractive alternative to the butadiene acrylonitrile elastomers often used for modification of epoxy networks. Poly(dimethyl siloxane) displays interesting properties; good thermal stability, weatherability, oxidative stability and moisture resistance. The non-polar nature and the low surface energy of PDMS drive thermodynamically the siloxane phase to migrate to the air-polymer interface. This sometimes occurs even in the case of chemically crosslinked microphase separated systems. Such a migration of the siloxane phase leads to the formation of a hydrophobic and chemically bound surface coating. Therefore, this 'slippery' surface layer enhances the friction and wear properties (i.e., decreases friction and wear) of the epoxy substrate[46].

Particulate fillers such as alumina and silica, glass, dolomite, and aluminum hydroxide and zirconia have also been investigated with limited success[47,48]. Hybrid systems like glass fillers in rubber modified epoxies and zirconia-rubber-epoxy systems have also been reported to enhance toughness[49].

The use of thermoplastic polymers as toughener for thermosets has become widely employed in attempts to improve the fracture toughness as well as high thermal and dimensional stability. Studies using non-reactive thermoplastic modifiers have not always indicated the significant improvement of the toughness. It may be due to poor adhesion between the thermoset matrix and the modifier phase or others. It has been demonstrated that the selection of a thermoplastic as a toughener is limited to a few reactive thermoplastic polymers that exhibit high toughness, ductility, and T_g[50-53].

Improvements in toughness along with the retention of the moderately high modulus and thermal stability have been reported in the case of polysulfone modified epoxy and bismaleimide networks[50-53]. A use of copolymer of polyethersulfone (PES) and polyether-phosphineoxide (PEPO) as a toughener for epoxy thermosets has been reported that an increase in the content of PEPO increases hydrogen bonding with hydroxyl groups in epoxy molecules[54]. The strength of hydrogen bonding increases not only the interfacial adhesion but also the solubility of the toughener with the epoxy resin. Fracture toughness

was considerably improved in the case of phase separation. However, phase mixed material due to the high solubility did not exhibit significant improvement of fracture toughness.

2.6.4. Toughening Mechanisms

The improvement of fracture toughness of a material can be achieved by maximizing the energy dissipated under the applied stress with which the material can change the microstructure in several modes. For a material with second phase embedded in a matrix, the possible modes are:

1) shear band formation near toughener particles
2) fracture of particles after cavitation
3) stretching
4) debonding
5) tearing of particles
6) transparticle fracture
7) debonding of hard particles
8) crack deflection by hard particles
9) voided/cavitated particles
10) crazing
11) plastic zone at crack tip
12) diffuse shear yielding
13) shear band/craze formation
14) pinning of crack front

The features of these deformations are depicted in Figure 2-19 and Figure 2-22. Some of such failure modes may take place in a toughened polymer simultaneously depending on the type of particles and the matrix.

2.6.4.1. Crack Bridging Mechanism

Crack bridging has been considered to be a toughening mechanism of rubber- or glass filled-modified epoxy by Kuz-Douglass *et al.*[55], Ahmad *et al.*[56] and Rose[57]. The increase in fracture toughness was considered to be due to the dissipation of energy, which had been stored during stretching the particles by the crack opening, by tearing or debonding of particles from the matrix. Kunz-Douglass derived the fracture toughness increase, DG_{IC}, from the rubber elasticity[55]:

$$\Delta G_{IC} = 4\gamma v_f \left(1 - \frac{6}{\lambda^2 + \lambda + 4}\right) \qquad (2\text{-}79)$$

where λ is either the extension ratio at the time of debonding or rubber tearing, γ is either the energy per unit area of interface required to debond from the matrix or the rubber tearing energy, and v_f is the volume fraction of rubber particles. Of interest is the effect of

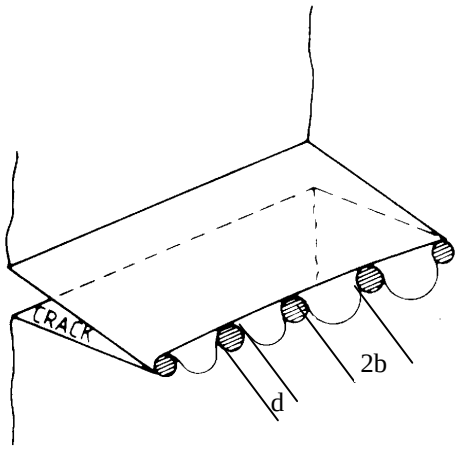

Figure 2-22. Schematic of the interaction of a crack front with dispersed particles by crack pining mechanism. The bowed crack front is at the verge of breaking away from pinning[58].

size and number density rather than volume fraction of particles on the fracture toughness in this thesis. If all the rubber particles are uniform in terms of number density and composition, the extension ratio of all particles on the crack tip at stretching would decrease with an increase in the particle size. Since $v_f \propto N_V r^3$ where N_V is the number of particles per unit volume and r is the radius of particles, the increase in fracture toughness is expected to be proportional linearly to the number density but has a maximum value with increase in the radius of particle.

Garg *et al.* showed that if the particle is elastic, the increase in fracture toughness due to the fracture of particle (mode 6 in Figure 2-19) is given by[28]

(2-80) $$\Delta G_{IC} = 3\eta^2 r v_f E e_b^2$$

where η is the stress concentration factor at the particle equator, r is the radius of the particle, v_f is the volume fraction of particles, E is Young's modulus of the particle and e_b is the strain of the particle at break.

2.6.4.2. Crack deflection

When the fracture toughness is improved by only the deflection of crack, which increases the crack surface area, the increase in the fracture toughness is given by

(2-81) $$\Delta G_{IC} = \pi r^2 N_A \gamma_m$$

Various theories have been set forth to explain the toughening mechanisms in rubber or particulate-filler modified epoxies. The fracture behavior may involve several

toughening mechanisms as depicted in Figure 2-19 and Figure 2-22. Several such modes may occur simultaneously contributing to the overall energy absorption process.

2.6.4.3. Crack pinning

The obstacles ahead of the crack tip prevent to the propagation of the crack front and cause an increase in toughness by bowing out the crack front between the obstacles as illustrated in Figure 2-22. Lange[59] has given a quantitative expression for the increase in the fracture toughness by crack pinning

$$\Delta G_{IC} = \frac{r g_m}{3b} \qquad (2\text{-}82)$$

where r is the average radius of the particles, $2b$ is the average interspacing between particles.

2.6.4.4. Rubber toughened epoxies

McGarry and co-workers[36-38] were the first to investigate the behavior of rubber toughened epoxies and suggested that the toughening mechanisms involved generation of crazes and shear banding in the vicinity of rubber particles. This was based on the observation of a stress whitened zone. They have suggested that large particles are responsible for crazing and small particles cause shear banding in CTBN modified epoxy resin[37]. Yee and Pearson[60,61] disputed such a theory and in turn suggested that the stress whitening zone was due to the micro-cavitation (voiding) of rubber particles.

Bucknall[62] has also postulated that crazing of a matrix containing rubber particle phase enhances the toughness. Crazing was attributed to an increase in volume during tensile creep tests. Yee and Peason[60,61] have disagreed such an interpretation by suggesting that volume dilation may also be caused by the cavitation of rubber particles.

Gebizlioglu *et al.*[63] has proposed that craze formation is related to mismatch in linear coefficient of thermal expansion and difference in the young's moduli.

Beaumont[55,64] established rubber particle tear energy model and emphasized importance in the role of the energy absorbed in the deformation and the fracture of the rubber particles. Kunz-Douglass[65] has demonstrated that the fracture toughness is not dependent on rubber volume fraction above 5% and is independent of particle size since the size increases with an increase in the rubber contents. Kunz-Douglass *et al.*[55] proposed rubber stretching and tearing as the dominant mechanism. They declined any contribution of shear yielding and crazing to toughness. However, Yee and Pearson opposed this model by suggesting that rubber stretching and tearing would account for only small increases in fracture toughness.

Kinloch[27,66,67] proposed toughening mechanism by the two basic processes in the vicinity of a crack tip: cavitation in the rubber or at the particle-matrix interface and localized shear yielding in the matrix initiated by the rubber particles. According to

Kinloch *et al.*[66], the Kunz-Douglass crack bridging model failed to account for stress whitening phenomena and it ignored contributions to toughness by rubber cavitation and shear yielding in the matrix. Riew[39] also agreed to Kinloch, Pearson and Yee showing that shear deformation in the matrix containing small rubber particles is dominant and crazing is caused by microvoid formation around large rubber particles. Maximum toughening is achieved under combined shear and craze deformations. According to Garg *et al.*[28], however, in addition to cavitation and shear yielding the role of crack bridging by the stretching and tearing of rubber particles cannot be neglected. Evan[68] concluded that combinations of dilation, microvoid, craze formation, shear banding and rubber stretching and tearing contribute the increase in the fracture toughness.

2.6.4.5. Particle Filled Epoxies

R. J. Young[49] suggested that a crack pinning for thermosets containing rigid particles is the primary toughening mechanism. For particle filled epoxies, the possible toughening mechanisms that have been suggested include: crack deflection, localized shear banding and yielding in the matrix around particles and crack blunting by the particles[48], and crack pinning[47]. It is also believed that crack blunting and crack pinning mechanisms are primarily responsible for enhancement of toughness in particular composites.

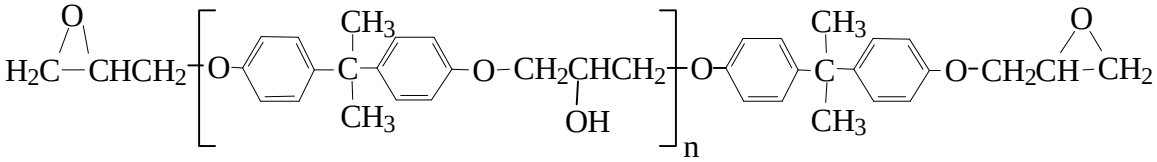

DER 331

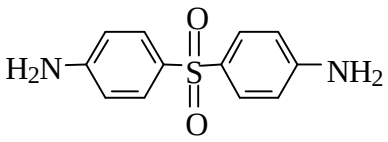

DDS

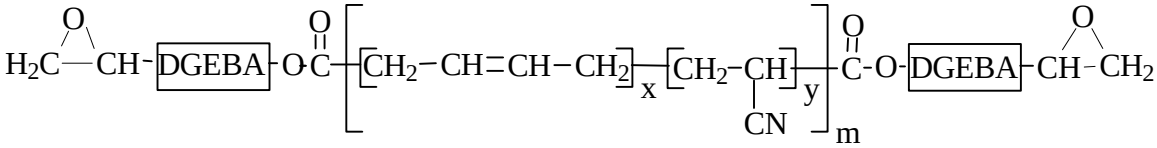

ETBN (40 %) + DGEBA Epoxy (60 %) = KELPOXY G272-100

Figure 2-23. Chemical structures of the materials used in this research

2.6.4.6. Thermoplastic Modified Epoxies

Pearson and Yee[60,61] have reviewed several toughening mechanisms that have been proposed for thermoplastic modified epoxies and these are as illustrated in Figure 2-19. Hedrick *et.al.*[50] based on SEM micrographs of the fracture surface in the case of Bisphenol-A polysulfone modified DGEBA epoxy suggested a particle bridging mechanism owing to ductile tearing of the fracture surface. Accordingly, plastic deformation of thermoplastic particles and epoxy matrix was postulated to be the main energy absorbing processes.

Kim and Brown[69] on the basis of their studies involving thermoplastic toughening of a resorcinol based epoxy attributed the source of toughness to a combination of particle-bridging and yielding of individual particles resulting from stress concentration in the particle-matrix interface. They suggested that this promoted shear banding of the matrix. According to Zengli and Yishi, in addition to plastic deformation of the particles and the matrix, crack-pinning is the most important toughening mechanism in the thermoplastic modified epoxy resins. On the other hand, Bucknall and Gilbert[70] employed a commercial poly(etherimide) to modify a tetra-functional epoxy with a remarkable success. Based on their analysis, they suggested that the toughening mechanism was particle bridging.

2.7. MATERIALS

The chemical structures of epoxy resin, curing agent, and reactive liquid rubber used are shown in Figure 2-23. The epoxy resin and curing agent for the rubber-modified epoxy system are a diglycidyl ether of bisphenol A (DGEBA) resin (DER-331, Dow Chemical Company, molecular weight of about 374 g) and diaminodiphenyl sulfone (DDS, Aldrich Chemical Company, Inc. molecular weight of 248 g) which is soluble at the cure conditions adopted in this study. The toughener is an epoxy terminated copolymer of butadiene and acrylonitrile (ETBN) which was supplied in the form of a mixture with epoxy (KELPOXY G272-100, Reichhold, molecular weight of 680 g).

This was made by functionalizing the end groups of CTBN (carboxyl terminated butadiene and acrylonitrile copolymer) to epoxy groups in the excess of DGEBA epoxy, where the rubber content is 40 wt %. The rubber copolymer (CTBN) contains 26 wt % acrylonitrile. The molecular weight of the rubber component was back calculated to be 3150 g/mol from the GPC results shown in Figure 2-24.

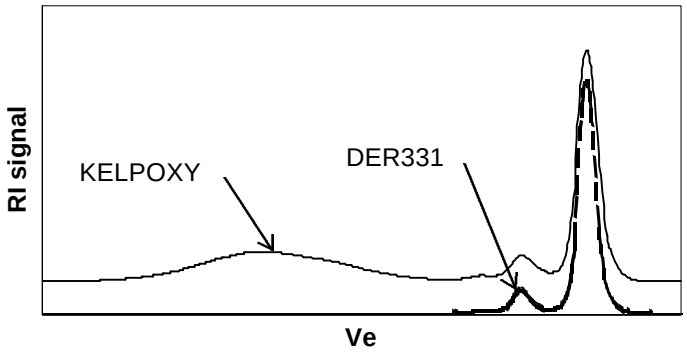

Figure 2-24. GPC chromatograms (RI detector) for KELPOXY G272-100 and DER 331

2.8. REFERENCES

1. F. W. Billmeyer Jr., Ed., "**Textbook of Polymer Science**", John Wiley and Sons, Inc., 1984, p. 436.
2. ASTM D-883-86b, "**Standard definition of terms relating to plastics**", Amer. Soc. for Testing Materials. Philadelphia, PA (1986).
3. H. F. Mark, N. M. Bikales, C. G. Overberger, G. Menges, Eds., **Encyclopedia of Polymer Science and Engineering**, Vol. 4, 1989, pp. 350-393.
4. P. J. Flory, "**Principles of Polymer Chemistry**", Cornell University Press, Ithaca, New York., 1953, Ch. 9.
5. W. Stockmayer, *J. Chem. Phys.*, **11**, 45 (1943); **12**, 125 (1944).
6. W. Stockmayer, *J. Polym. Sci.*, **9**, 69 (1952); **11**, 424 (1953).
7. C. W. Macosko, D. R. Miller, *Macromolecules*, **9**(2), 199 (1976).
8. J. B. Enns, J. K. Gillham, *J. Appl. Polym. Sci.*, **28**, 2567 (1983).
9. M. T. Aronhime, K. K. Gillham, *J. Coat. Tech.*, **56**, 35 (1984).
10. S. L. Simon, J. K. Gillham, *J. Appl. Polym. Sci.*, **47**, 461 (1993).
11. J. B. Enns, J. K. Gillham, *TRIP*, **2**, 406 (1994).
12. X. Peng, J. K. Gillham, *J. Appl. Polym. Sci.*, **30**, 4685 (1985).
13. L. C. Chan, H. N. Nae, J. K. Gillham, *J. Appl. Polym. Sci.*, **29**, 3307 (1984).
14. B. Rudolf, H. Cantow, *Macromolecules*, **28**, 6586 (1995); **28**, 6595 (1995).
15. I. C. Sanchez, R. H. Lacombe, *J. Phys. Chem.*, **80**, 2352 (1976); **80**, 2568 (1976).
16. P. J. Flory, *J. Polym. Sci., Part C*, **87**, 1833 (1965).
17. I. Prigogine, "**The Molecular Theory of Solutions**", North-Holland Publishing Co., Amsterdam, 1959.
18. D. J. Patterson, *J. Polym. Sci., Part C*, **16**, 3379 (1968).
19. P. J. Flory, "**Principles of Polymer Chemistry**", Cornell University Press, Ithaca, New York, 1953, Ch. 12.
20. J. H. Hildebrand, R. L. Scott, "**The Solubility of Non-Electrolytes**", 3rd Ed., American Chemical Society Monograph Series, 1950.
21. H. Tomba , "**Polymer Solutions**", Butterworth, London, 1956.

22. G. R. Strobl, J. T. Bendler, R. P. Kambour, A. R. Shultz, *Macromolecules*, **19**, 2683 (1986).

23. F. J. Flory, W. R. Krigbaum, *J. Chem. Phys.*, **18**, 1086 (1950).

24. J. W. Cahn, *J. Chem. Phys.*, **42**, 93 (1965).

25. P. J. Debye, *Chem. Phys.* **31**, 680 (1959).

26. R. H. Doremus, "**Rates of Phase Transformations**", Academic Press, Orlando, FL, 1985, p.65.

27. A. J. Kinloch, R. J. Young, "**Fracture Behavior of Polymers**", Applied Science Publishers Ltd. 1983,Chs. 1-4.

28. A. C. Garg, Y. W. Mai, *Comps. Sci. and Tech.*, **31**, 179, (1988).

29. G. R. Irwin, *Appl. Mats. Res.*, **3**, 65 (1964).

30. H. M. Westergaard, *J. Appl. Mech.*, **61**, 49 (1939).

31. G. C. Sih, "**Handbook of Stress Intensity Factors for Researchers and Engineers**", Lehigh Univ., Bethlehem, USA, 1973.

32. H. Tada, P. Paris, G. R. Irwin, "**The Stress Analysis of Cracks Handbook**", Del Research Corp., Hellertown, USA, 1973.

33. D. P. Rook, D. J. Cartwright, "**Compendium of Stress-Intensity Factors**", HMSO, London, 1976.

34. C. A. Arnold, P. M. Hergenrother, J. E. McGrath, "**An Overview of Orgranic Polym. Matrix Resins Composites"**, in "**Composite Applications: The Role of Fiber Matrix and Interface**", T. Vigo, B. Kinzig, Eds., VCH Publishers, 1992.

35. H. Lee, K. Neville, "Handbook of Epoxy Resins", McGraw Hill, 1967, Ch. 16.

36. F. J. McGarry, A. M. Wilner, *Org. Coat. Plast. Chem.*, **28**(1), 512 (1968).

37. J. N. Sultan, R. C. Laible, F. J. McGarry, *J. Appl. Polym. Sci.*, **6**, 127 (1971).

38. J. N. Sultan, F. J. McGarry, *Polym. Eng. Sci.*, **13**, 29 (1973).

39. C. K. Riew, E. H. Rowe, A. R. Siebert, In ***Toughness and Brittleness of Plastics***; R. D. Deanin, A. M. Crugnola, Eds.; Advances in Chemistry Series 154; American Chemical Society: Washington D.C., 1976; pp. 326-343

40. C. B. Bucknall, C. J. Page, V. O. Young, *J. Mater. Sci.*,**8**, 1800 (1973).

41. W. O. Bascom, R. L. Cottington, R. L. Jones, P. Peyser, *J. Appl. Polym. Sci*., **19**, 2545 (1975).

42. R. A. Pearson, A. F. Yee, *Polymer*, **34**, 3658 (1993).

43. E. M. Yorkgitis, N. S. Eiss Jr., C. Tran, G. L. Wilkes, J. E. McGrath, In ***Rubber-Modified Thermoset Resins***; Riew, C. K.; Gillham, J. K., Eds.; Advances in Chemistry 208; American Chemical Society: Washington D.C., 1984; p. 137.

44. Q. Ji, O. Kwon, M. Muggli, K. S. Kwan, J. E. McGrath, T. C. Ward,, *Polymer Preprint*, **38**, 107 (1997).

45. Q. Ji, O. Kwon, H. Kang, J. E. McGrath, T. C. Ward, *Polymer Preprint*, in press (1998).

46. E. M. Yorkgitis, N. S. Eiss Jr., C. Tran, G. L. Wilkes, J. E. McGrath, "**Advances in Polymer Science**", vol. 72, "Epoxy resins and Composites I", K. Dusek, Ed., Springer Verlag, 1985.

47. A. C. Maloney, H. H. Kausch, H. R. Stieger, *J. Mat. Sci.*, **18**, 208 (1983).

48. J. Spanoudakis, R. J. Young, *J. Mat. Sci.*, **19,** 473 (1984).

49. A. J. Kinloch, D. L. Maxwell, R. J. Young, *J. Mat. Sci.*, **20**, 4169 (1985).

50. J. L. Hedrick, I. Yilgor, G. L. Wilkes, J. E McGrath, *Poly. Bull.*, **13**, 201, (1985).

51. S. C. Liptak, S. P. Winkinson, J. C. Hedrick, T. C. Ward, J. E McGrath, *Radiation Effects on Polymers*, ACS Symp. Ser. **475**, 364 (1991).

52. S. P. Winkinson, T. C. Ward, J. E McGrath, *Polymer*, **34**(4), 870 (1993).

53. S. J. Pak, G. D. Lyle, R. Mercier, J. E McGrath, *Polymer*, **34**(4), 885 (1993).

54. J. Wang, S.Wang, Q. Ji, O. Kwon, J. E. McGrath, T. C. Ward, *Proc. Adhesion. Soc.*, (1998).

55. S. Kunz-Douglass, P. W. R. Beaumont, M. F. Ashby, *J. Mat. Sci.*, **15**, 1109 (1980).

56. Z. B. Ahmad, M. F. Ashby, P. W. R. Beaumont, *Scr. Mett.*, **20**, 843 (1986).

57. L. R. F. Rose, *Mech. Mater.*, **8**, 11 (1987).

58. F. F. Lange, In ***Composite Materials***, vol. 5: Fracture and Fatigue; L. J. Broutman, ed., Academic Press, New York, 1974, pp. 2-44.

59. F. F. Lange, *Phil. Mag.*, **22**, 1990, pp. 983-992.

60. A. F. Yee, R. A. Pearson, *J. Mat. Sci.*, **21**, 2462 (1986).

61. A. F. Yee, R. A. Pearson, *J. Mat. Sci.*, **21**, 2462 (1986).

62. C. B. Bucknall, "***Toughened Plastics"***, Applied Science Publishers, London, 1977.

63. O. S. Gebizlioglu, A. S. Argon, R. E. Cohen, *Polymer*, **26**, 519 (1985); **26**, 529 (1985).

64. S. Kunz, P. W. R. Beaumont, *J. Mat. Sci.*, **16**, 3141 (1981).

65. S. Kunz, J. A. Sayre, R.A. Assink, *Polymer*, **23**, 1897 (1982).

66. A. J. Kinloch, S. J. Shaw, D.A. Tod, D. L. Hunston, *Polymer*, **24**, 1341 (1983).

67. A. J. Kinloch, S. J. Shaw, D. L. Hunston, *Polymer*, **24**, 1355 (1983).

68. A. G. Evans, Z. B. Ahmad, D. G. Gilbert, P. W. R. Beaumont, *Proceedings of an International Conference: Toughening of Plastics-II*, London, July 2-4, 1985, The Plastics and Rubber Institute, p. 16.

69. S. C. Kim, H. R. Brown, *J. Mat. Sci.*, **22**, 2589 (1987).

70. C. B. Bucknall, A. H. Gilbert, *Polymer*, **30**, 213 (1989).

Chapter 3: CONSTRUCTION OF PARTICLE SIZE DISTRIBUTION

3.1. INTRODUCTION

In multicomponent polymeric blend systems, micro-phase separation can take place to form dispersed phases in a continuous matrix phase. The mechanical and physical properties of these types of materials are often dependent on the number, size, and interspacing of the dispersed phase particles[1-11]. Examples of this are high-impact polystyrene[5], acryronitrile-butadiene-styrene copolymers[6], and rubber-modified epoxies[1-4,7-13]. Microscopy has been widely used to examine morphological parameters in investigation of their effects on the properties of these phase separated materials.

The use of microscopy for quantitative study of these parameters presents difficulties arising from the fact that it provides only two dimensional information[1,7,10-13]. This two dimensional (2-D) information may not reflect the correct three dimensional (3-D) distribution. For instance, the diameter of a circle appearing in the micrograph of a thin-sectioned sample may be smaller than the actual diameter of the corresponding spherical particle; and, also, the number of particles in a unit area may not be the same as the actual number of particles in a unit volume. Nevertheless, many authors use two dimensional parameters as an approximation for or as a substitute for three dimensional representations[2,8-10]. The difference between these two representations may be considerable. Some researchers have used fractography to avoid underestimation of the size of the dispersed phase particles[11-13]. This assumes that the fractured surface always

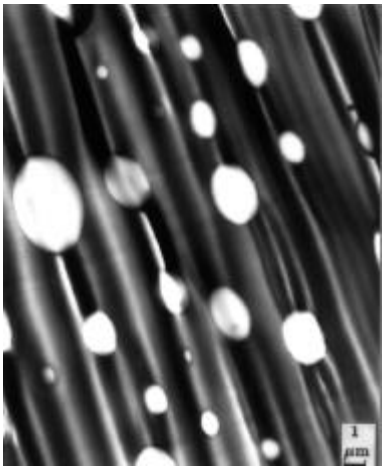

Figure 3-1. A transmission electron micrograph of a thin section of a rubber modified epoxy sample. The rubber-rich dispersed phase appears as ellipses rather than circles due to deformation of the spherical rubber particles by shearing action of the microtoming knife.

occurs on the equators of the presumed spherical particles. Although the radii on the fracture surface may be the actual radii of the particles, the surface is no longer a plane. This means that either the number of particles per unit area or the number of particles per unit volume cannot be obtained using this method. Both the number and size of particles in 3-D are important in describing a morphology as well as in influencing the mechanical and physical properties of a polymeric blend system[1-13].

Several statistical methods to convert 2-D parameters to 3-D information have been developed and may be found in various resources[14-20]. Though a method exists for the construction of 3-D size distributions from chord length measurements[14-16], it will not be discussed further. Here we will be restricted to constructions from 2-D data. For simplicity, we will limit our discussion to only those systems with spherical inclusions. To compare each statistical method with the various other methods as well as to the two dimensional data, a computer simulation technique was adopted.

This study presents a system where dispersed spherical particles are embedded in a continuous matrix and discusses the statistical methods which estimate the 3-D morphological parameters from 2-D data. A common example of this kind of a system is a rubber modified epoxy, whose multiphase microstructure can be seen clearly in the transmission electron micrograph of a thin section shown Figure 3-1. The aim of this work is not only to compare the various methods of constructing a 3-D distribution but also to suggest an experimental procedure to establish a representative 2-D distribution from micrographs.

Evaluation of the various simulations is accomplished by mimicking the process used to generate micrographs. This is performed on a system with a known true particle size distribution. First, it is necessary to place particles with a known size distribution in a random position in a rectangular box. Next, the box is randomly sectioned and a representative 2-D size distribution is generated by counting the circles appearing in the section area. Finally, an estimation of the 3-D parameters from the 2-D information by a conversion method is performed and the results are compared with the known true

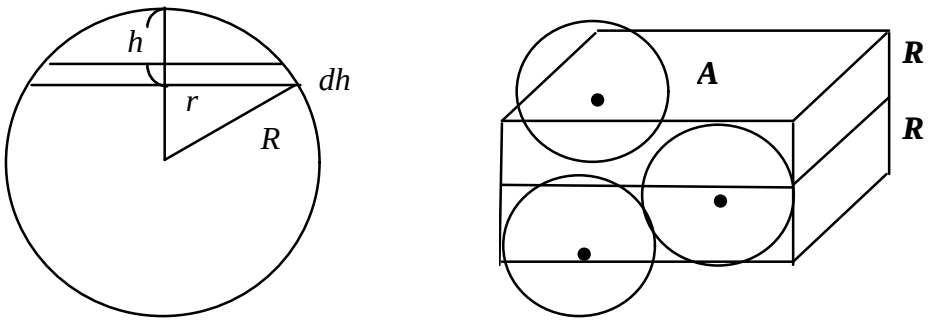

(a) (b)

Figure 3-2. Schematic diagrams (a) showing different sizes of circles created by dissection, and (b) showing probability to get thickness *dh* from a sphere of R_j.

values. This chapter will not only demonstrate how large the sampled section area should be to obtain a representative 2-D distribution but also suggest a method to judge the quality of the conversion.

3.2. THEORETICAL BACKGROUNDS

3.2.1. Fundamental Concepts-Monodisperse System

Consider a monodisperse system where N_V number of spheres of radius R are randomly distributed in a unit volume without overlapping. If the spheres are intersected by a plane of area A, only spheres whose centers lie within the distance R on either side of the plane will be intersected, as shown in Figure 3-2 (a). Therefore, the number of circles in the area of the plane, A, is equal to the number of spheres in a volume of height $2R$ and area of the plane, A. Therefore, the following equation holds,

$$N_A A = 2N_V AR \text{ or } N_A = 2N_V R \tag{3-1}$$

where N_A is the number of circles per unit area. Notice that the circles can have various radii in the range of $0 \le r \le R$ so that the distribution of the circles is continuous with the radius. Therefore, if the circles are classified into groups with the same radius, r_i, the total number of circles in a unit area can be written as

$$N_A = \int_0^R N_A(i)dr_i \tag{3-2}$$

where N_A(i) is the number of circles in a group i which have a radius of r_i. However, it is practically impossible to get a continuous 2-D distribution due to sampling limitations. The observed distribution is therefore often represented with a histogram rather than the continuum of the true 2-D distribution. If $N_A(i)$ represents the number of circles whose radius falls in the range of $r_l < r_I \le r_u$, the integral in equation (3-2) can be replaced by the summation through all groups,

$$N_A = \sum_i N_A(i) \tag{3-3}$$

The probability that a section makes a circle of radius r_i from a sphere of radius, R, is identical to the geometrical probability of obtaining thickness of dh from the radius R of a sphere as shown in Figure 3-2 (b)[15]. If the probability is denoted as $P(i)$, then

$$\begin{aligned} P(i) &= \frac{\text{Number of circles of radius } r_i}{\text{Total number of circles generated from spheres of } R} \\ &= \frac{N_A(i)}{\sum_i N_A(i)} = \frac{dh}{R} \end{aligned} \tag{3-4}$$

From Figure 3-2 (b), it is obvious that

$$(R-h)^2 = R^2 - r_i^2 \qquad (3\text{-}5)$$

Thus,

$$dh = \frac{r_i}{R-h}dr_i = \frac{r_i}{\sqrt{R^2 - r_i^2}}dr_i \qquad (3\text{-}6)$$

and the probability of obtaining a circle of radius, r_i, in the range of $r_l < r_I \le r_u$ can be computed as follows:

$$P(i) = P(r_l < r_i \le r_u) = \int_{r_l}^{r_u} \frac{r_i}{R\sqrt{R^2 - r_i^2}}dr_i = \frac{1}{R}\left[\sqrt{R^2 - r_l^2} - \sqrt{R^2 - r_u^2}\right] \qquad (3\text{-}7)$$

Once the upper and the lower limits of each circle group are set, the expected circle size distribution can be constructed from equations (3-1), (3-4), and (3-7). As more circles are counted in a larger plane, the resulting circle size distribution will approach the expected circle size distribution. The selection of the minimum sample size area necessary to examine for a given experiment will be discussed more fully later, so that the calculated sphere size distribution will accurately depict the true distribution.

3.2.2. Extension to Polydisperse System

Consider a polydisperse system, consisting of randomly dispersed spheres of different sizes in a volume without overlapping. We define this system by the number per unit volume and the radius of spheres, $N_V(j)$ and R_j, of a sphere group j. If this system were randomly dissected, circles in a circle group i could be made from different sphere groups, which are larger than or equal to the circle group size. The number of circles in a circle group i made from spheres in a sphere group j will be denoted as $N_A(i,j)$, where radius of the sphere group j is larger than or equal to that of the circle group i. Then, the total number of circles made from a sphere group with a radius, R_j, can be represented by the sum of $N_A(i,j)$ through all possible i groups with the same principle as introduced in the equations (3-2) and (3-3), i.e.,

$$N_A \text{ made from the sphere group of } R_j = \int_0^{R_j} N_A(i,j)dr_i \text{ or } \sum_{i=1}^{j} N_A(i,j).$$

Similarly, equation (3-1) and (3-4) for a monodisperse system can be applied to the polydisperse system keeping in mind that an additional index, j, is used to denote a group of spheres, j. The probability of obtaining a circle of radius r_i from a sphere of radius R_j will be denoted as $P_j(i)$ and may be calculated as in equation (3-7). Therefore,

$$\sum_{i=1}^{j} N_A(i,j) = 2N_V(j)R_j \qquad (3\text{-}8)$$

(3-9) $$P_j(i) = \frac{N_A(i,j)}{\sum_{i=1}^{j} N_A(i,j)} = \frac{dh}{R_j}$$

Substitution of $\sum_{i=1}^{j} N_A(i,j)$ in equation (3-9) with equation (3-8) and rearrangement yields

(3-10) $$N_A(i,j) = 2P_j(i)N_V(j)R_j$$

However, the data obtained from microscopy is the number of circles in a group i, $N_A(i)$, which may originate from any spheres larger than or equal to r_i. Although we can not determine the origin of the circles in a given group, we know that $N_A(i)$ is the sum of the contributions from all spheres larger than or equal to r_i; that is,

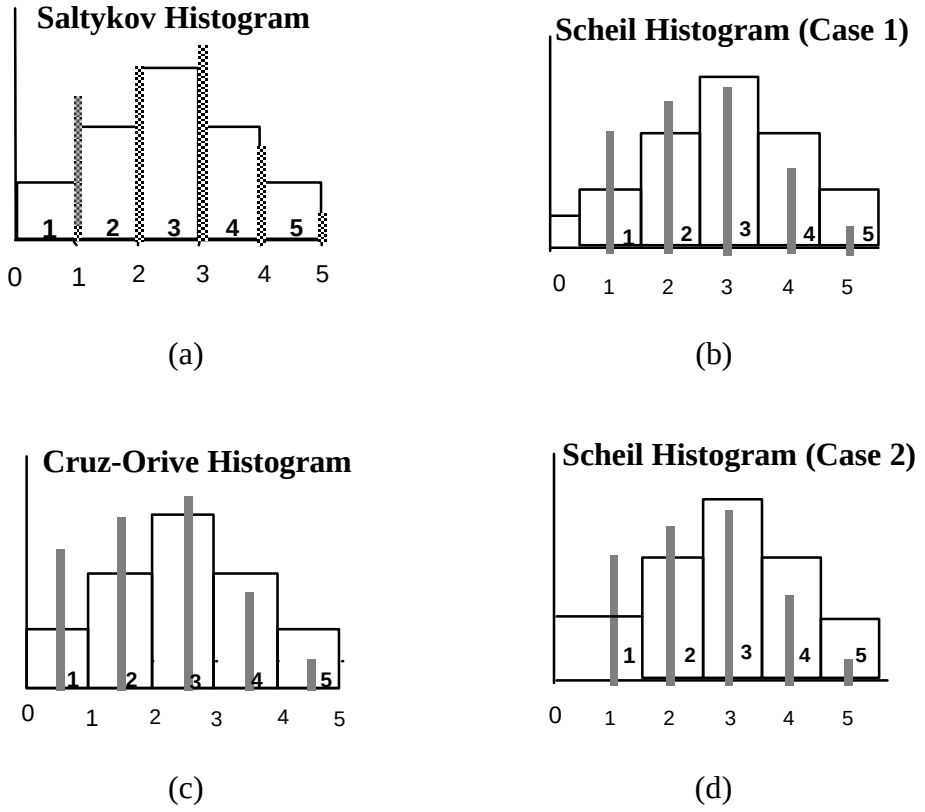

Figure 3-3. Schematic distributions for spheres (bold lines) and circles (square bars) showing different grouping methods. A bold number above the x-axis represents a group number of objects and a plain number below the x-axis represents the radius of a group.

$$N_A(i) = \sum_{j=i}^{m} N_A(i, j) \tag{3-11}$$

Therefore, summation of both sides of equation (3-10) yields the relation

$$N_A(i) = \sum_{j=i}^{m} 2N_V(j)P_j(i)R_j \tag{3-12}$$

Equation (3-12) is simply a matrix equation which can be solved for $N_V(j)$ once the probability $P_j(i)$ and the radius R_j are defined. We may further simplify equation (3-12) by introducing a coefficient matrix as $k_{ij} = 2P_j(i)R_j$. This coefficient matrix should be defined in order to compute $N_V(j)$ from $N_A(i)$. The coefficient matrix critically depends on the way the sphere and circle radii, R_j and r_i, are classified into size groups. Figure 3-3 illustrates how some typical methods classify the spheres and circles into size groups with an equal size interval between these groups.

If a sufficient number of circles in a section of a polydispersed sphere system are examined, the maximum radius of circles will be identical to the maximum radius of spheres because the equatorial position is the most probable location to bisect the sphere. Classification of spheres and circles with an equal interval requires knowledge of the number of size groups. Let us suppose the objects are to be classified into m groups. The group interval for both spheres and circles will then be $\Delta = R_{max}/m$, where R_{max} is the maximum radius of spheres or circles. It is significant that the distribution of spheres is discontinuous and exact, whereas that of circles is actually continuous and may be approximated by a discrete histogram as depicted in Figure 3-3. In other words, while all spheres in a group have the same radius, the circles in a group continuously vary in size within its interval. We will briefly describe three typical methods for the selection of groups with equal intervals: Saltykov's method[18], Scheil's method[19], and Cruz-Orive's method[20].

3.2.3. Transformation Coefficient Matrices

Saltykov classified circles and spheres into m groups with the class interval $\Delta = R_{max}/m$ as shown in Figure 3-3 (a). The radius of the jth sphere group R_j is taken to be $j\Delta$and the radius range of the ith circle group from $(i\text{-}1)\Delta$ to $i\Delta$ (i, j = 1, 2, ..., m). As a result of this choice, the coefficient matrix k_{ij} is defined as

$$k_{ij} = \begin{cases} 2\Delta\left[\sqrt{j^2-(i-1)^2} - \sqrt{j^2-i^2}\right] & \text{for } j \geq i \\ 0 & \text{for } j < i \end{cases} \tag{3-13}$$

Scheil defined the coefficient matrix k_{ij} by taking the sphere group as $j\Delta$ and the circle group range from $(i\text{-}1/2)\Delta$ to $(i\text{+}1/2)\Delta$. The resultant formula for the coefficient matrix k_{ij} is:

$$k_{ij} = \begin{cases} 2\Delta\left[\sqrt{j^2-(i-\frac{1}{2})^2}-\sqrt{j^2-\left(i+\frac{1}{2}\right)^2}\right] & \text{for } j \geq i \\ 0 & \text{for } j < i \end{cases} \qquad (3\text{-}14)$$

Equation (3-14) has been referenced in several publications without justification[14,16] and its values for 15x15 matrix have been tabulated and may be found elsewhere[15,19]. An unfortunate result of equation (3-14) is that imaginary numbers result when $j = i$. The table given by Scheil also appears to be values actually calculated from the formula for Saltykov's coefficient matrix shown in equation (3-13). This poses a question about the correct coefficient matrix formulation using Scheil's grouping method. As shown in Figure 3-3 (b) and (d), there are two ways to classify the first circle size group when the ith group occupies $(i\text{-}1/2)\Delta$ to $(i\text{+}1/2)\Delta$: Case1 takes the first group as range of $1/2\Delta\sim3/2\Delta$, and case 2 takes it as $0\sim3/2\Delta$.

For case 1 that $N_A(i)$ is taken to be number of circles of radii which fall into the range, $r_i\text{-}\Delta/2 < r \leq r_i\text{+}\Delta/2$, where i runs from 1 to m, $N_A(1)$ includes circles with a radius between $\Delta/2$ and $3\Delta/2$, and $N_A(m)$ includes circles with a radius between $(m\text{-}1/2)\Delta$ and $m\Delta$. However, it is unimportant that the range of $N_A(m)$ goes between $(m\text{-}1/2)\Delta$ and $m\Delta$ or between $(m\text{-}1/2)\Delta$ and $(m\text{+}1/2)\Delta$, because there are no circles larger than $m\Delta$. Notice that circles of radii less than $\Delta/2$ can not be included in any group, $N_A(i)$. The circles which fall in the region less than $\Delta/2$ can be denoted as the Oth group and its number density corresponds to $N_A(0)$. Because it is impossible to obtain radii of circles larger than r_i from the spheres of R_i, that is, in the case of $j = i$, the upper integral limit in equation (3-7) should not be $(i\text{+}1/2)\Delta$, but $i\Delta$. Therefore, the probability integral in equation (3-7) can be grouped into two cases for any $i = 1, 2, ..., m$ as follows:

$$P_j(i) = P_j\left(r_{i-1/2} < r \leq r_{i+1/2}\right) = \int_{r_{i-1/2}}^{r_{i+1/2}} \frac{r}{R_i\sqrt{R_i^2 - r_i^2}}\, dr_i \qquad \text{for } j = i\text{+}1, i\text{+}2, ..., m, \text{ and}$$

$$P_i(i) = P_i\left(r_{i-1/2} < r \leq r_i\right) = \int_{r_{i-1/2}}^{r_i} \frac{r}{R_i\sqrt{R_i^2 - r_i^2}}\, dr_i \qquad \text{for } j = i.$$

Substitution of these integrals into equation (3-12) leads to

$$
\begin{aligned}
N_A(i) &= \sum_{j=i}^{m} 2R_j N_v(j) P_j(i) \\
&= 2R_i N_v(i) P_i\left(\left(i-\frac{1}{2}\right)\Delta < r_i \le i\Delta\right) + \\
&\quad \sum_{j=i+1}^{m} 2R_j N_v(j) P_j\left(\left(i-\frac{1}{2}\right)\Delta < r_i \le \left(i+\frac{1}{2}\right)\Delta\right) \\
&= 2\Delta N_v(i)\left[\sqrt{i^2-\left(i-\frac{1}{2}\right)^2}\right] + \\
&\quad \sum_{j=i+1}^{m} 2\Delta N_v(j)\left[\sqrt{j^2-\left(i-\frac{1}{2}\right)^2}-\sqrt{j^2-\left(i+\frac{1}{2}\right)^2}\right] \\
&= \sum_{j=i}^{m} k_{ij} N_v(j)
\end{aligned}
\qquad \text{(3-15)}
$$

Therefore, the coefficient matrix for case 1 can be computed from the following equation:

$$
k_{ij} = \begin{cases}
2\Delta\left[\sqrt{j^2-(i-\frac{1}{2})^2}-\sqrt{j^2-\left(i+\frac{1}{2}\right)^2}\right] & \text{for } j > i \\
2\Delta\sqrt{i-\frac{1}{4}} & \text{for } j = i \\
0 & \text{for } j < i
\end{cases}
\qquad \text{(3-16)}
$$

This coefficient matrix also gives an m by m upper triangular matrix and m unknown variables, $N_V(j)$s. Therefore, the linear system of equations can be easily solved by a suitable numerical method[21]. Because the number of circles of radius less than $\Delta/2$, e.g., $N_A(0)$, can also be measured, this extra information as shown in equation (3-17) can be joined with the m by m coefficient matrix to give a new (m+1) by m matrix. This system of equations with a dimension of (m+1) by m can be solved by a least squares method to obtain $N_V(j)$[21].

$$
\begin{aligned}
N_A(0) &= \sum_{j=1}^{m} 2R_j N_v(j) P_j\left(0 < r_0 \le \frac{\Delta}{2}\right) \\
&= \sum_{j=1}^{m} N_v(j)\Delta\left[\sqrt{4j^2}-\sqrt{4j^2-1}\right]
\end{aligned}
\qquad \text{(3-17)}
$$

Case 2 is different from case 1 only in that $N_A(1)$ includes all circles of radii between 0 and 3Δ/2. Thus, the O[th] group no longer exists and the integral limits of the probability of obtaining circles of the first circle group from spheres of the second sphere group or larger groups should be 0 to 3Δ/2. Since spheres of the first sphere group which have radius of Δ cannot make a circle of radius larger than Δ, the upper limit of the probability integral should be Δ for $i = j = 1$. Therefore, if one uses the same procedure as in case 1 with caution for the first group, one must obtain equation (3-15) for $i = 2, 3, \ldots, m$. In the case of $i = 1$,

$$
\begin{aligned}
N_A(1) &= 2R_1 N_v(1) P_1\left(0 < r_1 \le 1\Delta\right) + \sum_{j=2}^{m} 2R_j N_v(j) P_j\left(0 < r_1 \le \frac{3}{2}\Delta\right) \\
&= 2\Delta N_v(i) + \sum_{j=i+1}^{m} 2\Delta N_v(j)\left[j - \sqrt{j^2 - \frac{9}{4}}\right] \qquad \text{(3-18)} \\
&= \sum_{j=1}^{m} k_{1j} N_v(j)
\end{aligned}
$$

Therefore, the coefficient matrix for case 2 can be written as

$$
k_{ij} = \begin{cases}
2\Delta & \text{for } j = i = 1 \\
2\Delta\left[j - \sqrt{j^2 - \frac{9}{4}}\right] & \text{for } j > i = 1 \\
2\Delta\sqrt{i - \frac{1}{4}} & \text{for } j = i \ge 2 \\
2\Delta\left[\sqrt{j^2 - (i - \frac{1}{2})^2} - \sqrt{j^2 - \left(i + \frac{1}{2}\right)^2}\right] & \text{for } j > i \ge 2 \\
0 & \text{for } j < i
\end{cases} \qquad \text{(3-19)}
$$

Cruz-Orive made a choice of sphere groups such that the true radius of a sphere group is on the mid-point of the group interval ($R_j = (j\text{-}1/2)\Delta$), and took the range of the i[th] circle group as $(i\text{-}1)\ \Delta$ through $i\Delta$ ($(i\text{-}1)\Delta < r_i \le i\Delta$) similar to Saltykov's method as shown in Figure 3-2 (c). In the case of $j = i$, the upper integral limit in equation (3-7) should be $(i\text{-}1/2)\Delta$, since a sphere of the radius, $R_i = (i\ \text{-}1/2)\Delta$ cannot make a circle bigger than its radius. Therefore, taking the same procedure as in equation (3-15) provides the coefficient matrix for the Cruz-Orive method with

$$(3\text{-}20)\qquad k_{ij}=\begin{cases}2\Delta\sqrt{i-\dfrac{3}{4}} & \text{for } j=i\\ 2\Delta\left[\sqrt{\left(j-\dfrac{1}{2}\right)^2-(i-1)^2}-\sqrt{\left(j-\dfrac{1}{2}\right)^2-i^2}\right] & \text{for } j>i\\ 0 & \text{for } j<i\end{cases}$$

A suitable selection of the size groups for a circle size histogram as well as a proper coefficient matrix should be made depending on which method is employed for the reconstruction of the three dimensional distribution. We can test the described conversion methods with a known system and compare an estimated distribution with the true one. It is sometimes difficult to decide which estimated distribution is the better representation of the true distribution, because the number of particles in some groups may be underestimated while those in the other groups may be overestimated. We now introduce a new single parameter that quantifies the overall quality of an estimated distribution compared to the true distribution. The similarity parameter χ may be defined as follows:

$$(3\text{-}21)\qquad c=\frac{1}{m}\sum_{i=1}^{m}\frac{\left|f_i-f_i^T\right|}{f_i^T}$$

where f_i is a frequency which is the number density of the ith group divided by the total number density and the superscript, T, indicates the true values. By this definition, χ will be zero if the estimated distribution is exactly identical to the true distribution. This χ value is more sensitive to low frequency values than high frequency values. A lower value of χ means that the estimated distribution is globally more similar to the true distribution.

3.2.4. Morphological Parameters

Once a well estimated three dimensional distribution ($N_V(i)$) is achieved, many important morphological parameters can be extracted from it. The number, the area, and the volume average radii, $\overline{R_N}$, $\overline{R_A}$, and $\overline{R_V}$, respectively, can be calculated from the distribution:

$$(3\text{-}22)\qquad \overline{R_N}=\frac{\sum_{i=1}^{m}N_V(i)R_i}{\sum_{i=1}^{m}N_V(i)},\ \overline{R_A}=\left(\frac{\sum_{i=1}^{m}N_V(i)R_i^2}{\sum_{i=1}^{m}N_V(i)}\right)^{\frac{1}{2}},\ \text{and}\ \overline{R_V}=\left(\frac{\sum_{i=1}^{m}N_V(i)R_i^3}{\sum_{i=1}^{m}N_V(i)}\right)^{\frac{1}{3}}$$

The volume fraction V_f is defined as the total volume of spheres that is contained in the unit volume of the matrix so that

(3-23) $$V_f = \frac{4p}{3}\sum_{i=1}^{m} N_V(i)R_i^3$$

The surface density S_V expresses the ratio of total surface area of spheres to the volume of the matrix. Therefore,

(3-24) $$S_V = 4p\sum_{i=1}^{m} N_V(i)R_i^2$$

Another useful description of structure is the mean free distance λ between particles. This gives the average surface-to-surface distance between each particle and all of its neighbors. This mean free distance is directly related to the volume-to-surface ratio of the matrix in which the particles are embedded[14]:

(3-25) $$l = 4\frac{1-V_f}{S_V}$$

3.3. RESULTS AND DISCUSSION

3.3.1. Particle Size Distribution Starting with Zero Particle Size

The formulations of the methods which have been described in the previous sections were tested with a series of known histograms as shown in Table 3-1: two Gaussian distributions, a small-particle-enriched distribution, a large-particle-enriched distribution, and a bimodal distribution. All of the distributions in Table 3-1 have 10 groups with an equal step size of 1 μm. All distributions except the Gaussian distribution 2 in Table 3-1 have the group radii of 1, 2, 3,…, 10 μm. The group radii of the Gaussian distribution 2 runs from 0.5 μm to 9.5 μm. The Gaussian distributions 1 and 2 have symmetrical distributions with mean values of 5.5 μm and 5.0 μm, respectively. In the small-particle-enriched distribution, a peak occurs at a group radius of 2 μm while the large-particle-enriched distribution shows a peak at a group radius of 9 μm. The bimodal distribution presents a distribution with two peaks at group radii of 3 μm and 8 μm.

In order to make a randomly distributed polydispersed spherical system representing a given distribution, the center coordinates of spheres of different radii in a box of a known volume were randomly generated such that they do not overlap with others or the sides of the box, and these positions were recorded. The program, NEWGEN, was coded to accommodate a maximum of 100,000 spheres. Once the edge length of the box, the radius and the number of each sphere group are entered into NEWGEN, the coordinates of the sphere centers relative to a corner of box are generated

Table 3-1. Distributions of known sphere systems.

Group ID	Gaussian 1		Gaussian 2		Small particle enriched		Large particle enriched		Bimodal	
	Radius (μm)	N_V (mm^{-3})	Radius (μm)	N_V (mm^{-3})	Radius (μm)	N_V (mm^{-3})	Radius (μm)	N_V (mm^{-3})	Radius (μm)	NV (mm^{-3})
1	1.0	1690	0.5	1605	1.0	96792	1.0	152	1.0	439
2	2.0	4595	1.5	4364	2.0	153468	2.0	494	2.0	1663
3	3.0	9728	2.5	9239	3.0	78921	3.0	938	3.0	3074
4	4.0	16040	3.5	15233	4.0	45134	4.0	1319	4.0	1709
5	5.0	20595	4.5	19559	5.0	32741	5.0	1937	5.0	500
6	6.0	20595	5.5	19559	6.0	22375	6.0	2835	6.0	2197
7	7.0	16040	6.5	15233	7.0	15231	7.0	3908	7.0	3926
8	8.0	9728	7.5	9239	8.0	10833	8.0	6833	8.0	6250
9	9.0	4595	8.5	4364	9.0	5708	9.0	13287	9.0	3540
10	10.0	1690	9.5	1605	10.0	1759	10.0	8380	10.0	1116
Total		105295		100000		462963		40082		24414
Avg	5.5		5.0		2.98		8.02		6.39	

to yield a randomly distributed polydispersed sphere system. The true sphere distributions and average radii are presented in Table 3-1. For example, Gaussian distribution 1 in Table 3-1 was generated with 100,000 spheres in a box of 0.949703 mm^3 to yield a volume fraction of spheres of 10%.

The construction of a circle distribution was made by cutting the box at a position along the z-axis, measuring the size of circles in the section and counting the number of circles which fall in each size group. For the Gaussian distribution 1 in Table 3-1, the section plane has an area of 0.982949 mm x 0.982949 mm. The section plane was divided into frames of equal area (side length = 0.196590 mm), as shown in Figure 3-4. All frames are not necessarily in one section plane. It is sometimes necessary to take multiple sections in different locations to obtain sufficient particles to assure accurate representation. In this case, however, careful sectioning should be made so that the same spheres should not be cut more than once by any other section. The circular objects in multiple frames were counted to construct a representative circle size distribution. When the center of a circular object contacted the south or west boundary lines of a frame, it was included as an object within that. However, the objects whose centers lie on the north or the east boundary lines were excluded.

The area number density $N_A(i)$ was obtained from the number of circles in a frame divided by the area of the frame. Measurements in a single frame may not be sufficient to obtain a representative 2-D distribution. It is obvious that the measured distribution will approach the expected value as the total frame area examined goes to infinity. Therefore, it is a requirement that the largest number of frames possible be examined in order to obtain the expected 2-D distribution. The question is how many frames need to

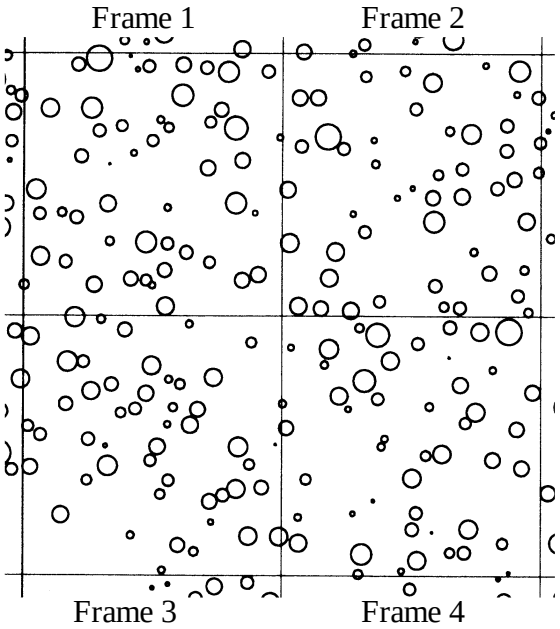

Figure 3-4. Circular objects appearing in each frame with edge length of 0.1965898 mm for the Gaussian distribution 1. The objects whose centers lie in the area of a frame are counted for the construction of distribution.

be examined to obtain a representative 2-D distribution. In order to quantify the quality of the measured distribution, a new parameter, δ, is introduced as follows:

$$d = \frac{\sqrt{\sum_{i}^{m} \left(N_A(i)_k - N_A(i)_{k-1} \right)^2}}{m}$$

where $N_A(i)_k = \frac{\sum_{l=1}^{k} N(i)_l}{\sum_{l=1}^{k} A_l}$, and $N(i)_l$ represents the number of circles appearing in the l^{th} frame of area, A_l. The quantity δ will asymptotically approach zero with an increase in the number of frames examined. The quantity δ was plotted as a function of the accumulated number of frames for the Gaussian, the small-particle-enriched, and the large-particle-enriched distributions as illustrated in Figure 3-5. One characteristic of them is that the peaks of the distributions are shifted toward larger radii in the order of the Gaussian, the small-particle-enriched, and the large-particle-enriched distributions. Because the probability of a section cutting large spheres is higher than the probability of it cutting small spheres, the small-particle-enriched distribution more slowly approaches the expected circle distribution than the large-particle-enriched distribution. Therefore, more frames should be examined in the case of the small-particle-enriched system to yield the

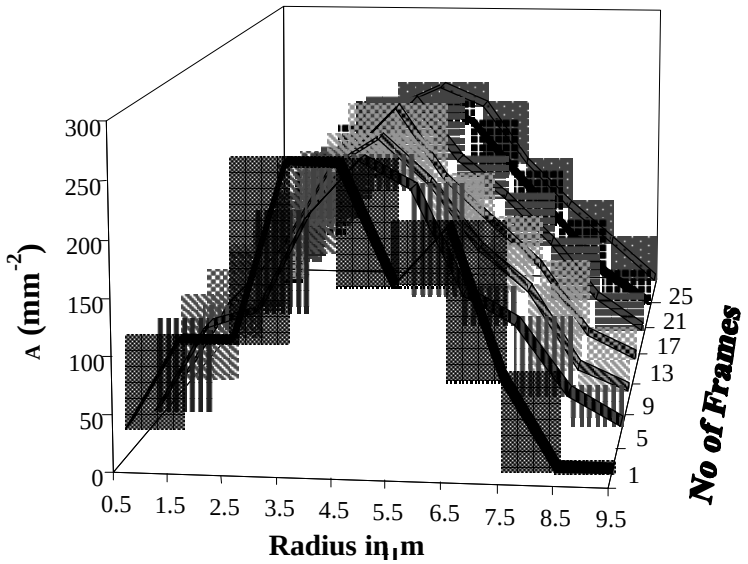

Figure 3-5. Variation of circle size distributions as more number of frames are examined. The numbers in the radius axis indicate the midpoints of the circle groups.

same number of particles sampled. Examination of more frames is expensive in time and costs. Thus, the number of frames that should be examined to form a well-represented 2-D distribution may have to be compromised. Figure 3-6 illustrates how the measured circle size distribution varies with increasing cumulative number of frames sampled. Measurement of only one frame may lead the observer to misidentify the sample as having a bimodal distribution when the actual distribution is unimodal. The circle size distributions for all systems except for the Gaussian distribution 1 were constructed with

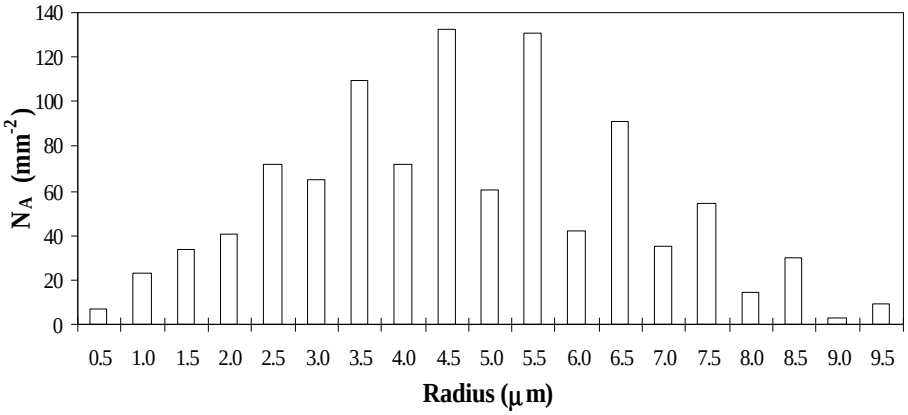

Figure 3-6. Section histogram of the Gaussian distribution 2 with half step size of the original sphere size group.

75 frames. The circle size distribution for the Gaussian distribution 1 was constructed with 25 frames. These are considered sufficient for the estimation of a 3-D distribution within a satisfactory error range.

Table 3-2 presents as a typical example the circle size histograms constructed from sections of the Gaussian distribution 1 in Table 3-1. As mentioned earlier, the different conversion methods utilize different classifications for circle size histograms (see Figure 3-3). While Saltykov's and Cruz-Orive's methods use the range of the i^{th} circle group as $(i\text{-}1)\Delta$ through $i\Delta$, both case 1 and case 2 take it to be $(i\text{-}1/2)\Delta$ through $(i\text{+}1/2)\Delta$ except for the first group. The first group range for case 1 runs from $1/2\Delta$ to $3/2\Delta$ and the extra group called the zeroth group runs from 0 to $1/2\Delta$. Case 2 takes it as 0 to $3/2\Delta$. As a result of these different classifications, the mid-point of each circle group for case 1 and case 2 shifts to larger radii than that for the Saltykov or Cruz-Orive case by half of the group size except for the first group. Therefore, the circle average radii calculated using the midpoints of groups should be different for different classification methods. In conclusion, the group range of the circle size distribution should be chosen according to the method employed for the estimation of the sphere size distribution.

Since the true discrete distribution is usually not known, neither the interval Δ between the adjacent sphere groups nor the number of sphere groups is known. Therefore, determination of the number of groups and the group range for the circle distribution is not well defined. However, if a smaller range of a circle group than the actual interval between the adjacent sphere groups is taken for the construction of the circle size histogram, its characteristic shape appears as shown in Figure 3-7. It is constructed from the system of the Gaussian distribution 2 with the step size of 0.5 μm, half of the original sphere size group (1.0 μm). Because the probability of obtaining a circle of the about same radius as that of the corresponding sphere is much higher than the probability of obtaining a circle smaller than that of the corresponding sphere ($P_j(j \geq i > j\text{-}1/2) >> P_j(j\text{-}1/2 \geq i > j\text{-}1)$), a see-saw type of histogram as shown in Figure 3-7 is usually obtained if a sufficient number of circles are examined. In this case, we can predict the

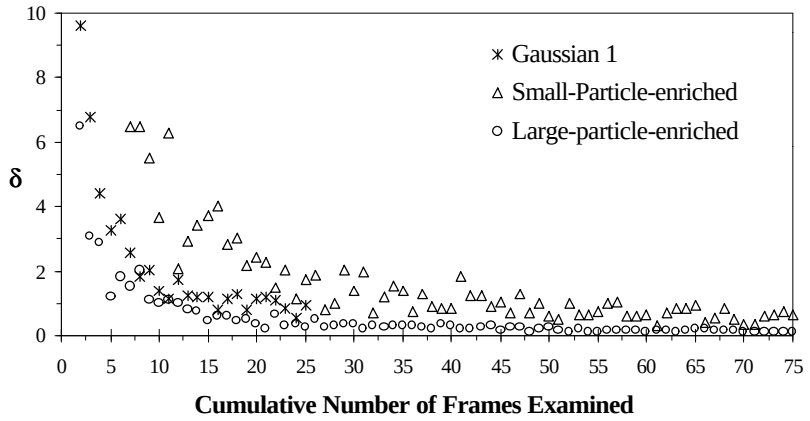

Figure 3-7. Plot of δ against the cumulative number of frames examined.

radius of each actual sphere group from the circle size histogram without knowledge of the sphere system. As the interval size between the adjacent sphere groups decreases, the number of circle measurements required to resolve the actual sphere groups increases tremendously. We can treat this kind of sphere system as a "continuous" distribution and the circle group range can be determined somewhat arbitrarily in this case. This type of system will be discussed later with an example.

Since the true discrete distribution is usually not known, neither the interval Δ between the adjacent sphere groups nor the number of sphere groups is known. Therefore, determination of the number of groups and the group range for the circle distribution is not well defined. However, if a smaller range of a circle group than the actual interval between the adjacent sphere groups is taken for the construction of the circle size histogram, its characteristic shape appears as shown in Figure 3-7. It is constructed from the system of the Gaussian distribution 2 with the step size of 0.5 μm, half of the original sphere size group (1.0 μm). Because the probability of obtaining a circle of the about same radius as that of the corresponding sphere is much higher than the probability of obtaining a circle smaller than that of the corresponding sphere ($P_j(j \geq i > j\text{-}1/2) >> P_j(j\text{-}1/2 \geq i > j\text{-}1)$), a see-saw type of histogram as shown in Figure 3-7 is usually obtained if a sufficient number of circles are examined. In this case, we can predict the radius of each actual sphere group from the circle size histogram without knowledge of the sphere system. As the interval size between the adjacent sphere groups decreases, the number of circle measurements required to resolve the actual sphere groups increases tremendously. We can treat this kind of sphere system as a "continuous" distribution and the circle group range can be determined somewhat arbitrarily in this case. This type of system will be discussed later with an example.

A representative 2-D histogram which has been measured according to a specified classification method was transformed to a 3-D distribution with the various conversion methods: Saltykov's method, Scheil's methods (case 1 and case 2), or Cruz-Orive's method. The resulting 3-D distributions are presented together with the true distributions in Figure 3-8. The values of the similarity parameter χ for each method are tabulated along with morphological parameters in Table 3-3. Although a smaller value of χ is better, it only represents the overall similarity. Because the value of χ is very sensitive to groups which have a small number of particles, the error for groups with a small number of particles may control the χ value. However, average values such as average radius are usually dominated by groups with a large number of particles. Therefore, the parameter χ alone should not be used as the only evaluation tool for the quality of the estimated distribution. An example of this is the small-particle-enriched distribution. The large-particle-enriched distribution in Table 3-3 and in Figure 3-8 reveals that the case 2 method shows the lowest χ value among those estimating methods excluding the direct 2-D method while the estimated number average radius is poorer than that produced using Saltykov's method, which shows the highest χ value.

Table 3-2. Comparisons of the estimated distributions with the true ones in terms of structural parameters.

		2-D		Cruz-Orive		Saltykov		Case 1		Case 2		True
		(% rel.error)		(% rel.error)		(% rel.error)		(% rel.error)		(% rel.error)		
I	$<R_N>$	4.69	(14.7)	5.22	(5.1)	5.44	(1.1)	5.50	(0.0)	5.51	(0.2)	5.50
	$<R_V>$	5.48	(10.2)	5.89	(3.4)	6.07	(0.5)	6.09	(0.2)	6.10	(0.0)	6.10
	V_f	0.0865	(13.5)	0.0967	(3.3)	0.1014	(1.4)	0.1013	(1.3)	0.1018	(1.8)	0.1000
	S_v	0.0415	(7.6)	0.0444	(1.1)	0.0455	(1.3)	0.0454	(1.1)	0.0456	(1.6)	0.0449
	λ	87.97	(9.7)	81.47	(1.6)	79.12	(1.3)	79.30	(1.1)	78.95	(1.5)	80.18
	N_V	124366	(18.1)	111565	(6.0)	108522	(3.1)	106915	(1.5)	107121	(1.7)	105295
	χ	0.561		0.146		0.101		0.163		0.182		0.0
II	$<R_N>$	4.51	(9.8)	4.80	(4.0)	5.08	(1.6)	4.82	(3.6)	4.82	(3.6)	5.00
	$<R_V>$	5.24	(7.1)	5.55	(1.6)	5.79	(2.7)	5.46	(3.2)	5.46	(3.2)	5.64
	V_f	0.0687	(8.8)	0.0763	(1.3)	0.0819	(8.8)	0.0686	(8.9)	0.0690	(8.4)	0.0753
	S_v	0.0345	(4.2)	0.0367	(1.9)	0.0380	(5.6)	0.0343	(4.7)	0.0346	(3.9)	0.0360
	λ	107.99	(5.1)	100.79	(1.9)	96.64	(5.9)	108.48	(5.6)	107.69	(4.8)	102.71
	N_V	113663	(13.7)	106656	(6.7)	100414	(0.4)	105675	(5.7)	106401	(6.4)	100000
	χ	0.347		0.459		0.162		0.106		0.106		0.0
III	$<R_N>$	3.17	(6.2)	2.43	(18.4)	2.95	(1.0)	2.98	(0.0)	2.98	(0.2)	2.98
	$<R_V>$	4.38	(6.8)	3.77	(8.1)	4.10	(0.0)	4.11	(0.1)	4.10	(0.1)	4.10
	V_f	0.1597	(19.3)	0.1322	(1.3)	0.1403	(4.8)	0.1367	(2.1)	0.1396	(4.3)	0.1339
	S_v	0.0841	(14.5)	0.0735	(0.1)	0.0765	(4.1)	0.0747	(1.7)	0.0764	(4.0)	0.0735
	λ	39.97	(15.3)	47.23	(0.1)	44.97	(4.7)	46.21	(2.0)	45.06	(4.5)	47.17
	N_V	452832	(2.2)	589716	(27.4)	485808	(4.9)	470699	(1.7)	481980	(4.1)	462963
	χ	0.280		0.264		0.112		0.131		0.130		0.0
IV	$<R_N>$	6.52	(18.6)	8.00	(0.3)	7.97	(0.6)	7.81	(2.6)	7.85	(2.0)	8.02
	$<R_V>$	7.21	(14.3)	8.29	(1.4)	8.38	(0.4)	8.33	(1.0)	8.35	(0.8)	8.41
	V_f	0.0787	(21.3)	0.0977	(2.3)	0.1011	(1.1)	0.1011	(1.1)	0.1013	(1.3)	0.1000
	S_v	0.0302	(11.9)	0.0341	(0.5)	0.0347	(1.2)	0.0346	(1.0)	0.0347	(1.3)	0.0342
	λ	122.189	(16.2)	105.883	(0.7)	103.76	(1.3)	103.929	(1.1)	103.644	(1.4)	105.12
	N_V	50119	(25.0)	40888	(2.0)	41034	(2.4)	41813	(4.3)	41624	(3.8)	40082
	χ	1.344		0.656		0.732		0.615		0.432		0.0.
V	$<R_N>$	5.71	(10.6)	6.06	(5.1)	6.36	(0.5)	6.39	(0.1)	6.40	(0.2)	6.39
	$<R_V>$	6.49	(9.4)	7.00	(2.3)	7.21	(0.6)	7.22	(0.8)	7.23	(0.8)	7.17
	V_f	0.0317	(15.9)	0.0374	(0.6)	0.0389	(3.3)	0.0388	(3.0)	0.0389	(3.4)	0.0376
	S_v	0.0132	(8.3)	0.0144	(0.1)	0.0147	(2.1)	0.0146	(1.8)	0.0147	(2.2)	0.0144
	λ	293.58	(9.7)	267.49	(0.1)	261.87	(2.2)	262.68	(1.9)	261.51	(2.3)	267.68
	N_V	27587	(13.0)	25989	(6.5)	24785	(1.5)	24537	(0.5)	24614	(0.8)	24414
	χ	0.834		0.398		0.380		0.354		0.347		0.000

$<R_N>$, $<R_V>$, and λ have unit of μm and V_f and χ have no unit. S_v has a unit of μm^{-1}, and the total number of particle per unit volume, N_V, has a unit of mm^{-3}.

I is the Gaussian distribution 1, II the Gaussian distribution 2, III the small-particle-enriched distribution, IV the large-particle-enriched distribution, and V the bimodal distribution.

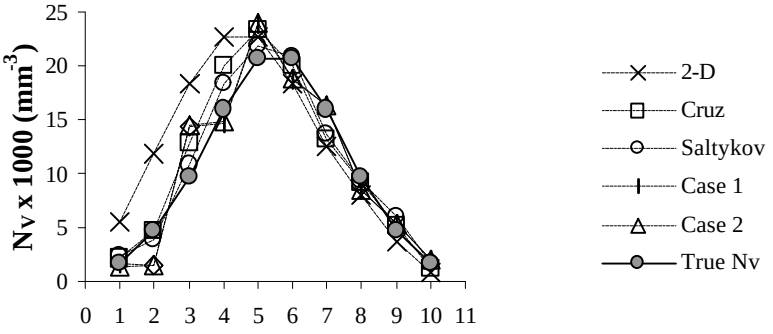

a) Gaussian Distribution 1

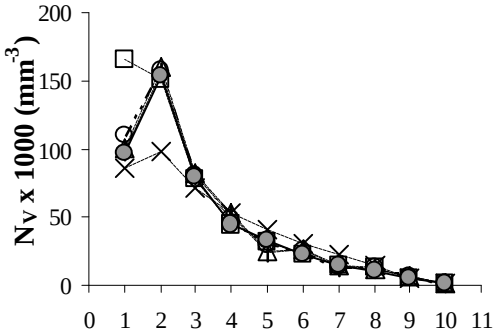

b) Gaussian Distribution 2

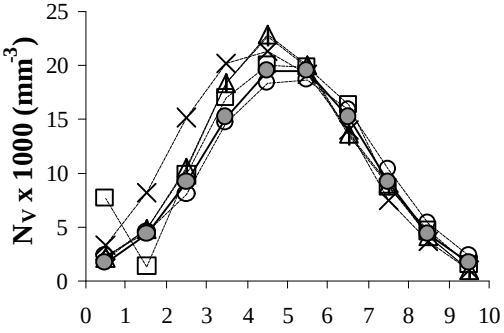

c) Small-particle-enriched Distribution

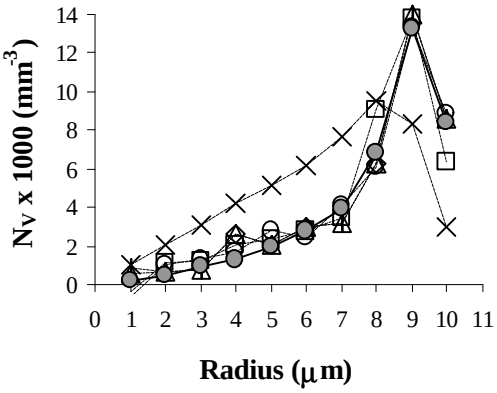

d) Large-particle-enriched Distribution

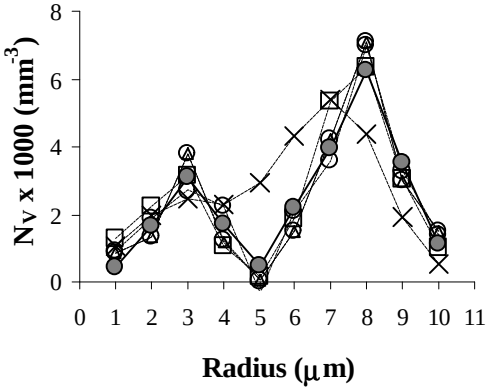

e) Bimodal Distribution

Figure 3-8. Comparison of estimated sphere size distributions with the true distribution. Lines between data points are drawn for easy identification.

The values in the column labeled "2-D" in Table 3-3 and 3-5 were calculated under the assumption that the circle frequency profile by Saltykov's grouping procedure is the same as the sphere frequency profile. Since the total number of spheres in a unit volume N_V can be calculated using equation (3-1), the frequency profile can be transformed to a sphere size distribution, $N_V(i)$. Therefore, an estimated sphere size distribution was obtained by multiplying the frequency of each circle group by the total number of spheres per unit volume. From this estimated distribution the parameter values in the first columns of Table 3-3 and 3-5 were obtained.

Because the Cruz-Orive method considers the actual radii of the sphere group to be in the middle of the circle group range as shown in Figure 3-2, the group radii of the estimated sphere size histograms do not match those predicted by the Saltykov's or Scheil's case 1 or case 2 method. For comparison of this result with those given by other methods, we should estimate the number of particles in a group of the same radius as the alternative methods. A simple way is to take an average value of any two adjacent groups. For example, the number density in a group of radius 1 μm can be obtained using half of the sum of the number densities in the groups with radii of 0.5 μm and 1.5 μm. Of course, because the true group radii of the Gaussian distribution 2 are composed of 0.5, 1.5, …, and 9.5 μm, estimated distributions by the other methods were transformed to this radius basis.

The prediction by direct use of 2-D data deviated most from the true values among the tested methods with a maximum relative error of about 25%. From results shown in Table 3-3 and 3-5 and Figure 3-8 and Figure 3-10, the direct use of a circle size distribution may be problematic because it deviates significantly from the true distribution for some systems (e.g. the bimodal distribution) while it is similar to the true distribution for other systems (e.g. the small-particle-enriched distribution). The direct use of a circle size distribution seems to be most accurate for a system which has a greater population in the small particle size groups.

Table 3-3. Morphological parameters computed from the average distributions of Saltykov, Cruz-Orive, and Case 2 for all tested systems.

	Gaussian 1	Gaussian 2	Small particle enriched	Large particle enriched	Bimodal	Continuous
	% rel. error	% rel. error	% rel. error	% rel. error	% rel. error	% rel. error
$<R_N>$	5.41 (1.6)	4.90 (1.9)	2.88 (3.4)	7.88 (1.7)	6.31 (1.3)	4.97 (0.6)
$<R_V>$	6.03 (1.2)	5.60 (0.8)	4.04 (1.6)	8.32 (1.1)	7.16 (0.1)	5.44 (0.6)
V_f	0.1000 (0.0)	0.0769 (2.1)	0.1374 (2.6)	0.1001 (0.1)	0.0384 (2.0)	0.1026 (1.8)
S_v	0.0452 (0.6)	0.0368 (2.2)	0.0754 (2.7)	0.0345 (0.7)	0.0146 (1.5)	0.0522 (0.4)
λ	79.71 (0.6)	100.34 (2.3)	45.74 (3.0)	104.42 (0.7)	263.60 (1.5)	68.82 (0.6)
N_V	109069 (3.6)	104490 (4.5)	498172 (7.6)	41480 (3.5)	24987 (2.3)	152028 (0.1)
χ	0.134	0.191	0.121	0.394	0.317	0.684

Table 3-4. Comparison of the estimated distributions with the true distribution for the system described in Figure 3-10 in terms of structural parameters.

	2-D		Cruz-Orive		Saltykov		Case 1		Case 2		True
	(% rel.error)		(% rel.error)		(% rel.error)		(% rel.error)		(% rel.error)		
$<R_N>$	4.28	(14.4)	4.82	(3.5)	5.06	(1.2)	4.93	(1.4)	4.93	(0.2)	5.00
$<R_V>$	4.93	(8.9)	5.37	(0.8)	5.55	(2.6)	5.37	(0.8)	5.37	(0.8)	5.41
V_f	0.0887	(12.0)	0.1014	(0.5)	0.1071	(6.2)	0.0988	(1.9)	0.0994	(1.4)	0.1008
S_v	0.0478	(8.0)	0.0518	(0.4)	0.0533	(2.5)	0.0511	(1.7)	0.0514	(1.1)	0.0520
λ	76.25	(10.2)	69.42	(0.3)	67.02	(3.2)	70.55	(1.9)	70.09	(1.3)	69.21
N_V	176483	(16.2)	156588	(3.1)	149230	(1.7)	152392	(0.4)	153235	(0.9)	151832
χ	1.930		0.796		0.770		0.552		0.562		0.0

We conclude that this direct method is the least accurate among those tested methods and we therefore will limit our discussion to the other methods. The other four methods predict the morphological parameters within a relative error of about 5% except for the results for the small-particle-enriched distribution by the Cruz-Orive method. It is illustrated in Figure 3-8 that the Cruz-Orive method suffers more from over- or under-estimation for the small particle size groups than the other methods. Because of this, the Cruz-Orive method is not as good as the other methods for analyzing a distribution that has a larger population of small particles. From those results in Table 3-3 and Figure 3-8, the Cruz-Orive method shows no advantages over the other three methods examined. This conclusion is somewhat inconsistent with published results[14]. We think this inconsistency may arise from a different treatment of group radii. Unfortunately, the details of the examination of each method were not published.

Because one method was superior to another for a given morphological system yet was inferior to other methods for other morphological systems, selecting any one technique as the absolute “best” is not possible based on our findings. It is suggested that taking an average of the distributions estimated by the Cruz-Orive, Saltykov, and case 1or case 2 methods may be a safe choice regardless of a possible small sacrifice in accuracy compared to the best method for a specific system. Predictions of the sphere size distribution by case 1 and case 2 methods did not show significant differences between them. If we use both distributions predicted by the case 1 and case 2 methods in calculation of the average distribution, this average may be weighted toward this distribution. Therefore, either method could be used in the average distribution in addition to Cruz-Orive’s and Saltykov’s methods, but not both.

The morphological parameter values computed from the average distributions of all systems estimated by the Cruz-Orive, Saltykov, and case 2 methods are presented in Table 4. This demonstrates that taking the average of the distributions estimated by these three methods improves the overall accuracy compared to the distribution estimated by each method individually.

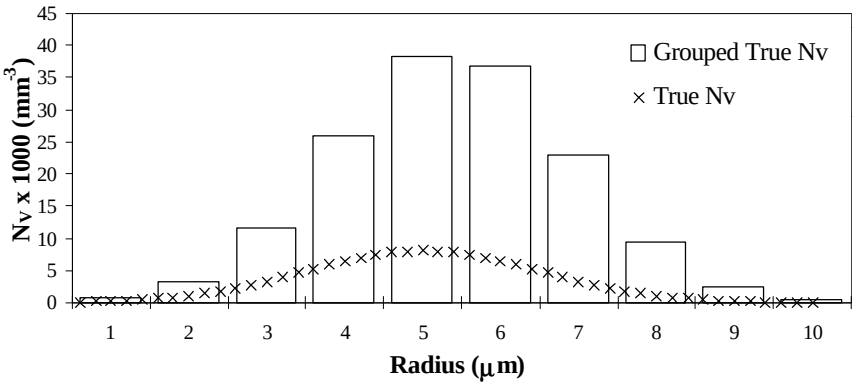

Figure 3-9. The sphere size distribution with the actual interval between adjacent groups (cross points) and the regrouped distribution with a wider interval (bars).

When a homogeneous polymeric blend system undergoes phase separation isotropically by a nucleation and growth mechanism, nuclei of a definite size with a certain population form and grow with time[22]. The resulting particle size distribution can be treated as a "continuous" distribution rather than a discrete distribution because the interval between the adjacent particle groups is too small to resolve in actual measurements.

In order to mimic this situation, let us suppose that the true distribution has an interval of 0.2 μm, but a given microscope can only discern objects down to 1 μm. In Figure 3-9, this type of a system is illustrated showing the true distribution with cross points and the grouped histogram with bars. Because it requires tremendous effort to construct a representative circle histogram with group size of 0.2 μm, a circle size histogram with a group size of 1 μm was constructed for the conversion to sphere size distribution. The estimated sphere size histograms will therefore appear as if the sizes of spheres are discrete with an interval of 1 μm.

The morphological parameters with the χ values from the sphere distributions estimated by the tested conversion methods are given in Table 3-5. The results are similar to those given for systems described earlier. Specially, the average distribution for this system gives, as a whole, better predictions of the structural parameters than the other systems tested in this study. This is apparently due to the fact that the actual distribution of spheres are regrouped locally into a large sphere group range, while the other systems have sphere groups consistent with the true size of spheres.

3.3.2. Particle Size Distribution Starting with Non-Zero Particle Size

We have so far successfully predicted distributions of several sphere systems. A common characteristic of these distributions is that the first sphere group has spheres

Table 3-5. Morphological parameters computed from the average distributions of Saltykov, Cruz-Orive, and Case 2 for all tested systems.

	Gaussian 1		Gaussian 2		Small particle enriched		Large particle enriched		Bimodal		Continuous	
	% rel. error		% rel. error		% rel. error		% rel. error		% rel. error		% rel. error	
$<R_N>$	5.41	(1.6)	4.90	(1.9)	2.88	(3.4)	7.88	(1.7)	6.31	(1.3)	4.97	(0.6)
$<R_V>$	6.03	(1.2)	5.60	(0.8)	4.04	(1.6)	8.32	(1.1)	7.16	(0.1)	5.44	(0.6)
V_f	0.1000	(0.0)	0.0769	(2.1)	0.1374	(2.6)	0.1001	(0.1)	0.0384	(2.0)	0.1026	(1.8)
S_v	0.0452	(0.6)	0.0368	(2.2)	0.0754	(2.7)	0.0345	(0.7)	0.0146	(1.5)	0.0522	(0.4)
λ	79.71	(0.6)	100.34	(2.3)	45.74	(3.0)	104.42	(0.7)	263.60	(1.5)	68.82	(0.6)
N_V	109069	(3.6)	104490	(4.5)	498172	(7.6)	41480	(3.5)	24987	(2.3)	152028	(0.1)
χ	0.134		0.191		0.121		0.394		0.317		0.684	

arranged such that the number of circles in the first group have partially originated from the spheres in the first group. What would happen in a sphere system where the first group or several groups have no spheres? When a sufficient number of sections of such a system are examined, the circles which fall in the first group or several groups ($0 < r \leq i\Delta$) are still found though there are no spheres of this size in an actual sphere system. If we use a coefficient matrix which ranges from the first sphere group to the last sphere group as was done for the systems described earlier, the resulting number of particles in the first group be negative or appear highly overestimated. This is due to an accumulation of errors from large radius groups on those small size groups.

If we are able to identify the groups in which the number of particles cannot be negligible, we can intentionally set the number density in the sphere groups below it as zero. For instance, if the distribution has a significant number of particles starting from the k^{th} group, the sphere groups below the k^{th} group would have negligible or zero number

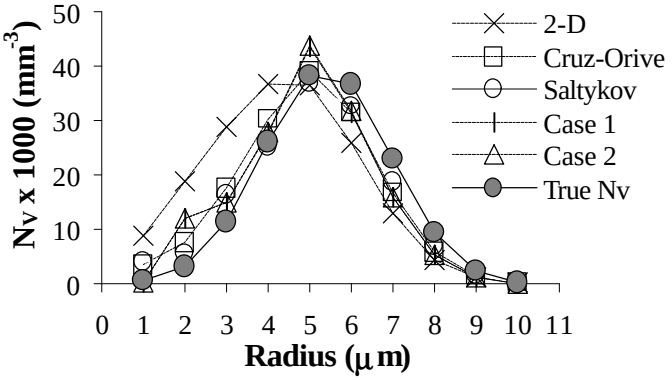

Figure 3-10. Comparison of estimated sphere size distributions with the grouped distribution of "continuous" sphere size system as shown in Figure 3-9. Lines between data points are drawn for easy identification.

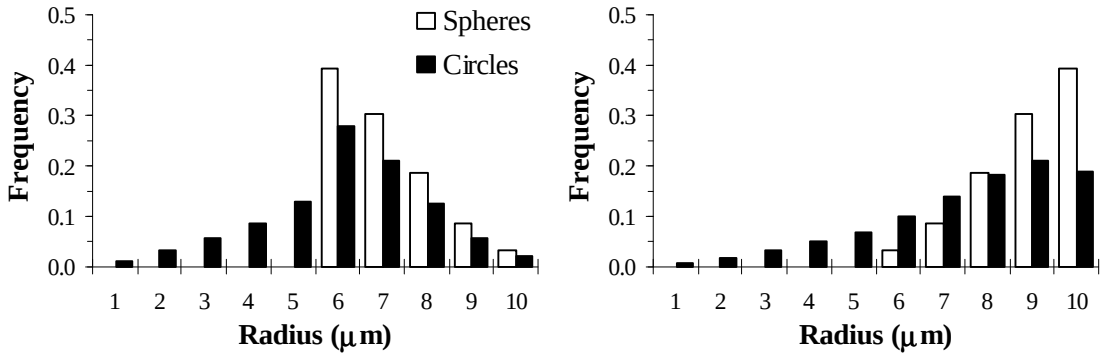

(a) (b)

Figure 3-11. Two typical size histograms expected from the two extreme sphere size distributions when the sphere systems are randomly dissected.

of particles. Computation with a suitable coefficient matrix should yield zero for these groups. Placing zeros in the elements of the coefficient matrix corresponding to the negligible sphere group forces the resulting $N_V(j)$ to be zeros where j = 1, 2, 3, ..., k-1. The coefficient matrix now has dimensions of m by (m-k+1) instead of m by m, and the unknowns $N_V(j)$ are (m-k+1) and the knowns $N_A(i)$ are m. This m by (m-k+1) linear system of equations may be solved by using a least squares method[21]. Using this treatment, we can prevent error propagation from large particle size groups to small particle size groups and eliminate some small particle size groups having meaningless negative numbers.

The problem in this case is how to determine which circle groups contain circles originating from larger spheres and none from spheres of the same size. Let us suppose the true distribution has sphere sizes beginning with the k^{th} sphere group. A section of this sphere system provides a circle size distribution beginning with zero radius. The $(k-1)^{th}$ circle group has only the sum of contributions of the k^{th} and higher sphere groups and no contribution from its own sphere group. Because the major contribution of a circle group is made from its own sphere group, the circles in a group below the k^{th} group would not be as numerous as the circles in a group above the k^{th} group. Therefore, we expect a jump in the population of the k^{th} group in the circle distribution as shown in Figure 3-11 (a). In some cases, the magnitude of the jump in the circle distribution may be too small to allow identification of the group from which significant number of particles originate. Such a case is illustrated in Figure 3-11 (b), where the frequency variation across the sphere groups is very smooth starting from zero. In this case, use of the normal coefficient matrix does not affect the results significantly.

3.4. CONCLUSIONS

It has been shown that a representative circle size distribution is a requirement for a good estimation of the sphere size distribution. The parameter δ has been introduced to check the validity of a circle size distribution measured from a micrograph. In addition, improved techniques of sampling for quantitative measurements with microscopy were suggested. A method of determination of the circle group size was given which is consistent with the true sphere group size for the construction of circle size distribution. Testing conversion methods with known polydisperse sphere systems revealed that the use of a circle size distribution as an approximation or substitute for the sphere size distribution may sometimes cause unacceptable errors. The method established by Scheil was found inaccurate for a recursive formula in a coefficient matrix. We have corrected and tested this method to predict a three dimensional distribution with results similar to Saltykov's or Cruz-Orive's method. These three methods have their own characteristics due to their unique methods of grouping circles and spheres. Therefore, taking an average of the various distribution estimation techniques combines their characteristics to predict the true distribution better than the distributions estimated individually.

3.5. REFERENCES

1. S. C. Kunz J. A. Sayre, R. A. Assink, *Polymer*, **23**, 1897 (1982).
2. C. B. Bucknall, T. Yoshii, *The British Polymer Journal*, **10**, 53 (1978).
3. S. Kunz-Douglass, W. R. Beaumont, M. F. Ashby, *J. Mater. Sci.*, **15**, 1109 (1980).
4. A. J. Kinloch, In *Rubber-Toughened Plastics*; C. K. Riew, Eds.; Advances in Chemistry 222; American Chemical Society: Washington DC, 1989, p 68.
5. C. R. Dupre, U. S. Patent 4 146 589, (1979).
6. A. Echte, In *Rubber-Toughened Plastics*; C. K. Riew, Eds.; Advances in Chemistry 222; American Chemical Society: Washington DC, 1989, p 16.
7. L. C. Chan, J. K. Gillham, A. J. Kinloch, S. J. Shaw, In *Rubber-Modified Thermoset Resins*; C. K. Riew, J. K. Gillham, Eds.; Advances in Chemistry 208; American Chemical Society: Washington DC, 1984, p 235.
8. A. F. Yee, R. A. Pearson, *J. Mater. Sci.*, **21**, 2462 (1986).
9. P. Bartlet, J. P. Pascault, H. Sautereau, *J. Appl. Polym. Sci.*, **30**, 2955 (1985).
10. W. H. Lee, K. A. Hodd, W. W. Wright, In *Rubber-Toughened Plastics*; C. K. Riew, Eds.; Advances in Chemistry 222; American Chemical Society: Washington DC, 1989, p 263.
11. D. Verchere, J. P. Pascault, H. Sautereau, S. M. Moschiar, C. C. Riccardi, R. J. J. Williams, *J. Appl. Polym. Sci.*, **42**, 701 (1991).
12. D. Chen, J. P. Pascault, H. Sautereau, *Polymer International*, **33**, 263 (1994).
13. E. Butta, G. Levita, A. Marchetti, A. Lazzeri, *Polym. Eng. Sci.*, **26**, 63 (1986).
14. E. R. Weibel, *Stereological Methods*; vols 1 and 2, Academic Press: New York, 1979.
15. E. E. Underwood, In *Quantitative Microscopy*; R. T. Dehoff, F. N. Rhines, Eds.; McGraw-Hill: New York, 1968, p 149.
16. S. L. Chan, In *Fractography and Failure Mechanisms of Polymers and Composites*; A. C. Roulin-Moloney, Ed.; Elsevier Applied Science: New York, 1989, p 145
17. J. C. Russ, *Computer-Assisted Microscopy*, Plenum Press: New York, 1990

18. Saltykov, S. A. *Stereometric Metallography*, 2nd Ed., Metallurgizdat: Moscow, 1958

19. Scheil, E. *Z. Metallk.***1935**, 27, 199.

20. Cruz-Orive, L. M. *J. Microscopy* **1978**, 112, 153.

21. Golub, G.; van Loan, C. F. *Matrix Computations*; John Hopkins University Press: Baltimore, 1989.

22. Olabisi, O.; Robeson, L. M.; Shaw, M. T. *Polymer Polymer Miscibility*; Academic Press: New York, 1979.

Chapter 4: MODEL FOR MORPHOLOGY PREDICTION

4.1. OBJECTIVES

In a formulation for a rubber toughened epoxy, the liquid reactive rubber is initially miscible with the epoxy resin and the curing agent. As polymerization starts at a designed temperature or temperature ramp, molecular chains grow and the weight average molecular weight of the epoxy molecule becomes infinite as the reaction approaches the gel point. The rubber component becomes incompatible with the epoxy resin at a certain degree of polymerization. This is due to the increase in free energy of mixing resulting from the decrease in the absolute value of change in configurational entropy. Therefore, phase separation from an initial homogeneous solution takes place to form a rubber-rich dispersed particle phase and an epoxy-rich matrix phase. This phase separation occurs at the degree of polymerization that can be experimentally observed as a cloud point.

The phase separation process is completed well before gelation or vitrification due to kinetic limitations in most rubber-modified epoxy systems. The morphology of the rubber phase developed by this process depends on the relative rates of polymerization and phase separation, which are controlled by the initial composition and the cure temperature. The mechanical and physical properties of the final product depend on the crosslink density, rubber compositions and glass transition temperatures in both dispersed and continuous phases, volume fraction, as well as the number and size of the dispersed particle phase. Cure conditions for a single formulation can vary all of these parameters.

It is desirable to predict and regulate how the morphology is developed at different cure temperatures and how the resulting morphological parameters affect the fracture toughness of the modified thermoset. Understanding the evolution of rubber rich particles by a phase separation process is crucially important in the control of morphology and thus in elucidating the toughening mechanism[1-3]. Williams and coworkers proposed a theoretical model based on the Flory-Huggins equation along with constitutive equations for polymerization and phase-separation rates to predict composition, volume fraction, number density and the average size of dispersed particles[4,5]. This model only works for phase separation in the metastable region. These researchers proposed that the rubber-modified epoxy thermosets employed in their model developed the rubber-rich particles by a nucleation and growth mechanism with the initial rubber composition being less than the critical composition. On the other hand, Yamanaka *et al.*[6-8] suggested that phase separation proceeds via spinodal decomposition and that the spherical domain structure results from the fixation of the morphology at a late stage of spinodal decomposition. Careful examination and enhancement of this model will provide a guide to producing desirable morphology as well as a theoretical justification for experimentally observed facts.

This chapter involves modification of the Williams model for predicting the particle size distribution as well as other morphological parameters which result from phase separation during polymerization. The same materials as those employed by Williams are analyzed with the modified model[8]. The concepts of this model and computation techniques will be described in this chapter with some simplifications for the purpose of illustration.

4.2. THEORETICAL CONSIDERATION

In order to predict the final morphology of the rubber modified epoxy system, it is necessary to understand how the rubber rich particles are generated from the epoxy-rich phase and grow during the phase separation process. The Flory-Huggins equation defines a thermodynamic equilibrium state of the system at each extent of cure. Since molecular chain mobility or diffusibility toward the equilibrium state decreases as reaction proceeds, the actual rubber composition may become locked in a non-equilibrium state. Williams and coworkers established a model to solve this non-equilibrium state problem by combining the Flory-Huggins theory with a nucleation and growth mechanism.

4.2.1. Thermodynamics of Binary Mixture

The free energy change of mixing per unit volume, ΔG_V^M, described by the Flory-Huggins equation is expressed as

$$\Delta G_V^M = \frac{RT}{\overline{V_1}}\left[(1-f_2)\ln(1-f_2)+\frac{f_2}{z}\ln f_2 + c f_2(1-f_2)\right] \quad (4\text{-}1)$$

where $\overline{V_1}$ is the molar volume of the epoxy resin, ϕ_2 is the volume fraction of the rubber component, z is the ratio of molar volumes of rubber to that of epoxy resin, and χ is the Flory-Huggins interaction parameter per mole of epoxy solvent. The parameters, $\overline{V_1}$, z, and χ, change with conversion due to chain extension[9]. These parameters can be related to the degree of conversion through the average molecular weight of non-linear polymers as described in Chapter 2.

When an epoxy resin is reacted with piperidine as a catalyst, the main reaction in forming the three dimensional network is etherification. Ring opening by a hydroxyl group in other molecules creates a hydroxyl group and this can link with other epoxide group by opening the ring. Therefore each epoxide group has two functionalities, and each epoxy monomer has two epoxide groups. Thus the functionality of this system can be regarded as four. Assuming that all functional groups have equal reactivity and no intramolecular reactions occur, the homopolymerization of an epoxy monomer with four reactive groups per mole can be characterized by the Flory-Stockmayer statistical approach or Macosko branching theory with the following parameters[9, 10]:

$$p_{gel} = \frac{1}{3} \quad (4\text{-}2)$$

(4-3) $$\overline{X_n} = \frac{\overline{M_{Np}}}{\overline{M_{No}}} = \frac{1}{1-2p}$$

(4-4) $$\overline{X_w} = \frac{\overline{M_{Wp}}}{\overline{M_{Wo}}} = \frac{1+p}{1-3p}$$

where M_N and M_W represent the number and weight average molecular weights, respectively, and the subscripts *p* and *o* denote the extent of conversion and monomer.

Equation (4-1) can then be expressed as a function of the degree of cure for non-linear step-growth polymerization with A_4 type of monomers

(4-5) $$\Delta G_V^M = \frac{RT}{\overline{V_{1_o}}}\left[(1-2p)(1-f_2)\ln(1-f_2) + \frac{f_2}{z_o}\ln f_2 + c_o f_2(1-f_2)\right]$$

through the following relations:

(4-6) $$\overline{V_1} = \overline{V_{1o}}\frac{\overline{M_{Np}}}{\overline{M_{No}}} = \frac{\overline{V_{1o}}}{1-2p}$$

(4-7) $$z = \frac{\overline{V_2}}{\overline{V_1}} = \frac{\overline{V_2}}{\overline{V_{1o}}}(1-2p) = z_o(1-2p)$$

(4-8) $$c = c_o\frac{\overline{V_1}}{\overline{V_{1o}}} = \frac{c_o}{1-2p}$$

Equation (4-5) can be used to illustrate the free energy of mixing curve at a certain degree of cure as a function of ϕ_2, as shown in Figure 4-1. In this figure, the molar volume ratio of rubber to epoxy, z_0, was set equal to 10 because the molecular weight of roughly 3500 g/mol for rubber and 380 g/mol of epoxy resin is often used in the rubber toughened epoxy. The interaction parameter was defined as $\chi_o = 0.35 + 90/T$ (K).

As the epoxy monomers polymerize, the free energy of mixing increases due to the decrease in the absolute value of the entropic contribution. At a certain degree of cure, phase separation will occur because the chemical potential of each component in the two phases is lower than that of a homogeneous solution. This situation is illustrated in Figure 4-1. The rubber composition of the continuous phase, ϕ_{2c}, remains the initial rubber composition, ϕ_{2o}, because the system is stable until it reaches a certain degree of cure, p_{cl}, which is the equilibrium point for the epoxy phase. At this conversion, the solution is supersaturated.

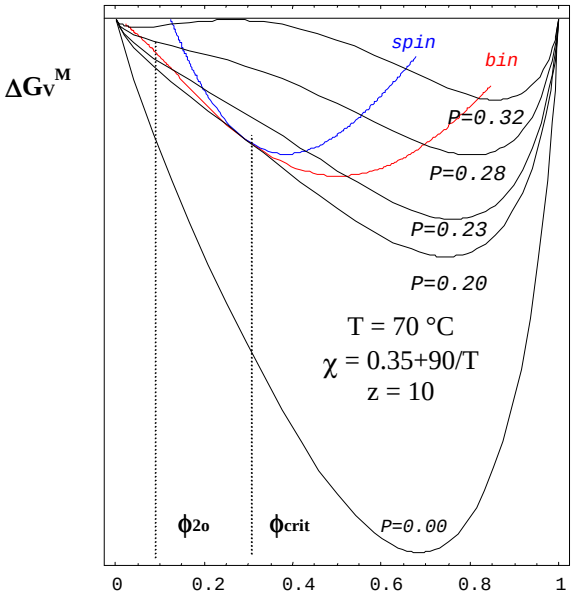

Figure 4-1. Free energy of mixing as a function of rubber volume fraction for different degrees of cure at different conversion. ϕ_{2o} is the initial rubber fraction and ϕ_{2crit} is the critical rubber fraction.

With an initial rubber volume fraction of ϕ_{2o} significantly less than the critical composition, phase separation may start at the degree of cure, p_{cl}, which corresponds to the value of the binodal curve at ϕ_{2o}, as shown in Figure 4-1. If the reaction proceeds further to a conversion p_i without changing the initial composition, ϕ_{2c}, the system will fall into a metastable state. All of the points on the tangent line at the rubber composition in the free energy curve corresponding to p_i represent the partial free energy per unit volume of the virtual homogeneous mixture of the solution, ϕ_{2c} with any other solution[11]. Therefore, the energy difference between the tangent line and the free energy curve represents the free energy change for the formation of the new phase, with a composition, ϕ_{2N} from the solution of ϕ_{2c}. This energy difference as a function of volume fraction of rubber is presented in Figure 4-2. A positive energy difference at ϕ_{2N} implies that the new phase with ϕ_{2N} cannot be formed, and a negative value means that the new phase can be formed with the composition ϕ_{2N}. Therefore, the maximum difference is the free energy change for the formation of an infinite size of the new phase. The composition corresponding to this maximum free energy is the rubber composition of the new phase.

If a homogeneous solution has a composition between spinodal and binodal compositions, phase separation requires composition perturbation large enough for the system to reach both of the equilibrium compositions due to its metastability. Even if composition fluctuation is sufficiently high to overcome the energy barrier, $\boldsymbol{E}_F$, which is

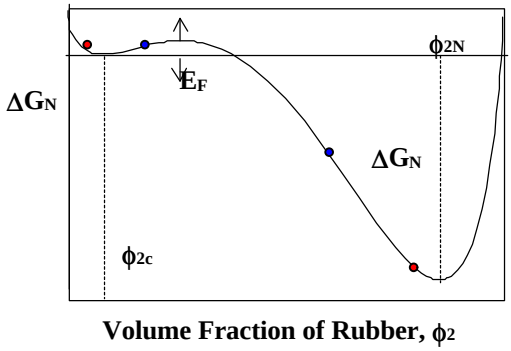

Figure 4-2. Free energy change per volume for the formation of infinite size of the new phase with composition of ϕ_{2N}. The dots on the curve represent the binodal and spinodal points.

illustrated in Figure 4-2, it is not necessary for the actual rubber composition of each phase to move to the corresponding equilibrium composition. The rate of composition fluctuation per unit volume, *F*, is proportional to the diffusion coefficient of rubber in the epoxy, *D*, and has an Arrhenius dependence on the energy barrier, $\boldsymbol{E}_F$

$$\frac{dF}{dt} = F_0 D \exp\left(-\frac{E_F}{RT}\right) \tag{4-9}$$

where F_0 is a proportionality constant.

When a new phase with composition ϕ_{2N} is formed from the parent phase with composition ϕ_{2c}, the composition of the parent phase, ϕ_{2c}, should reduce to a composition close to the equilibrium composition. Because the amount of the newly formed phase can be determined from the nucleation and growth theory, the new composition of the rubber in the parent phase can be determined from the law of mass conservation. Consequently, it is possible to track the variation of composition of both phases during phase separation.

The extent to which composition ϕ_{2c} approaches the equilibrium composition depends on the ratio of the rates of both phase separation and polymerization. This is because the cure reaction is proceeding to establish a new equilibrium composition while molecules are moving toward the old equilibrium composition. If the cure reaction is slow relative to the phase separation, the composition of each phase will evolve, passing through the binodal curve, as illustrated by the ϕ_{2c} curve for cure at 40 °C in Figure 4-3. If the cure reaction is fast relative to the phase separation, there will be insufficient time for the rubber composition to follow the binodal curve. This is illustrated by the ϕ_{2c} curve at 160 °C in Figure 4-3.

In contrast to the binodal region, a rubber composition inside the spinodal curve is unstable, and spontaneous phase separation will take place because there is no energy barrier, $\boldsymbol{E}_F$, in this region. As shown in Figure 4-3, spinodal decomposition requires a

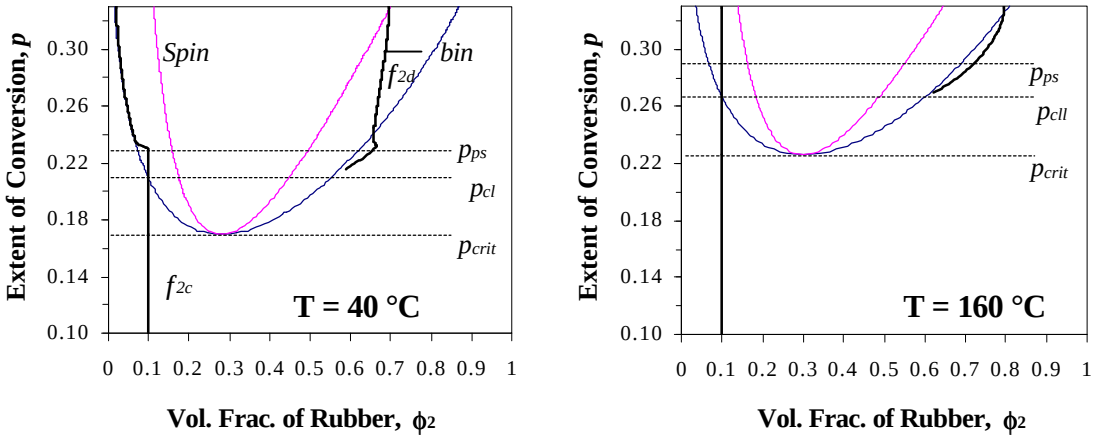

(a) (b)

Figure 4-3. Phase diagram of degree of cure as a function of volume fraction of rubber and trajectory of rubber compositions in both phases at 40 °C and at 160 °C. ϕ_{2d} is the average volume fraction of rubber in rubber phase.

system to have the initial rubber composition close to the critical composition, where the spinodal and the binodal curve have a common tangent. Also, the rate of cure should be considerably high and the cure temperature low to result in spinodal decomposition. Because the initial rubber composition should be small (5-20 wt %) for toughening epoxy thermoset, phase separation is usually considered to occur through the binodal decomposition for low molecular weight toughener (about 3000 g/mol). Therefore, this study is restricted to the phase separation in the metastable region.

4.2.2. Nucleation and Growth

Because the size of a new phase is finite, the free energy change for the formation of a finite size of a new phase must be affected by the surface free energy, σ, as well as the free energy change of new phase formation per unit volume, DG_N. Therefore, the free energy change for forming the new spherical phase of radius r can be expressed as

$$\Delta G(r) = \frac{4p}{3} r^3 \Delta G_N + 4pr^2 s \qquad (4\text{-}10)$$

where σ is the surface free energy. Williams indicated that σ did not affect the final morphology significantly when the value was varied from $4\text{x}10^{-4}$ to $2\text{x}10^{-2}$ N/m. In this study, the value was set to $2\text{x}10^{-4}$ N/m. $\Delta G(r)$ reaches a maximum value (ΔG_c) at the critical radius r_c. Using equation (4-10), the critical values can be calculated:

$$r_c = -\frac{2s}{\Delta G_N} \qquad (4\text{-}11)$$

(4-12) $$\Delta G_c = \frac{16p s^{3}}{3\Delta G_N^2}$$

The particles with a radius less than r_c are re-dissolved into the matrix phase, and the particles greater in size than r_c can grow. Therefore, the nucleation rate can be expressed in the product of the rate of composition fluctuations and the Boltzman factor with energy barrier of ΔG_c

(4-13) $$\frac{dN}{dt} = \frac{dF}{dt}\exp\left(-\frac{\Delta G_c}{kT}\right) = \frac{dF}{dt}\exp\left(-\frac{N_A \Delta G_c}{RT}\right)$$

where N_A is the Avogadro's number. From now on, we will express $N_A DG_c$ as DG_c and thus the unit for DG_c is J/mol.

Williams[8] assumed a simple second order reaction kinetics for illustration purposes,

(4-14) $$\frac{dp}{dt} = A(1-p)^2 \exp\left(-\frac{E_a}{RT}\right)$$

where the rate constant, A, and the activation energy, E_a, for the reaction were taken to be $5x10^7$ sec^{-1} and 83.14 KJ/mol, respectively. The viscosity of epoxy matrix increases as polymerization proceeds at a constant cure temperature due to the increase in molecular weight. Viscosity also decreases with temperature. Both the molecular weight and the temperature effect on the viscosity are usually expressed with the following equation:

(4-15) $$h(T,p) = h\big|_{\substack{p\to 0\\ T\to\infty}} \left(\frac{M_{wp}}{M_{wo}}\right)^n \exp\left[\frac{E_h}{RT}\right] = h\big|_{\substack{p\to 0\\ T\to\infty}} \left(\frac{1+p}{1-3p}\right)^n \exp\left[\frac{E_h}{RT}\right]$$

Williams used $\eta\big|_{\substack{p\to 0\\ T\to\infty}}$ =2.24 x 10^{-6} kg/m s, E_h = 33.3 KJ/mol and the power, n = 2 for simplicity.

Equation (4-13) can be rewritten in terms of the degree of cure, p, using equations (4-9), (4-13) and (4-14) and Stokes-Einstein equation, $D = \frac{D_0 T}{h}$

(4-16) $$\frac{dN}{dp} = \frac{F'_o T}{A}\left(\frac{1-3p}{1-p^2}\right)^2 \exp\left[\frac{E_a - E_h - E_F - \Delta G_c}{RT}\right]$$

where F'_0 is an adjustable parameter and set to 10^{11} $cm^{-3}K^{-1}sec^{-1}$. The E_F and ΔG_c are functions of the composition as well as the degree of cure p. It should be noticed that the unit of ΔG_c must be properly converted to the unit of J/mole. Equation (4-16) predicts that no nuclei are born at the gel point because of the infinite viscosity at the gel point. At

the binodal conversion, p_{cl}, the rubber-dissolved epoxy system is supersaturated and ΔG_c has an infinite value. Thus no particles are born. Therefore, the number of nuclei born at the degree of cure, p_{cl}, is equal to zero even though the size of particle is infinite.

The growth of nuclei born at a certain degree of cure, p, depends on the viscosity of the dispersed particle as well as the number of particles and extent of deviation, $\left(f_{2c} - f_2^a\right)$, from the equilibrium composition of rubber in the continuous phase. The growth rate, which is defined as the increase in volume fraction per unit time, is proportional to the interfacial area per unit volume and the driving force $\left(f_{2c} - f_2^a\right)$. That is,

$$\frac{dV}{dt} = 4\pi r^2 k_f N_V \left(f_{2c} - f_2^a\right) = 4\pi r^2 N_V \frac{dr}{dt} \tag{4-17}$$

where N_V is the number of particles in unit volume, and k_f is a mass transfer coefficient. The mass transfer coefficient for a sphere in a stagnant medium[12] is given by $k_\phi = \frac{D}{r}$. From equation (4-17), the following equation can be derived:

$$\frac{dr}{dt} = k_f \left(f_{2c} - f_2^a\right) \tag{4-18}$$

Therefore, using Stokes-Einstein relationship, the rate of change in radius can be written as

$$\begin{aligned} r\frac{dr}{dt} &= D\left(f_{2c} - f_2^a\right) = D_o \frac{T}{h}\left(f_{2c} - f_2^a\right) \\ &= D_o \frac{T}{h\big|_{\substack{T\to\infty \\ p\to 0}}} \left(\frac{1-3p}{1+p}\right)^2 \exp\left[-\frac{E_h}{RT}\right]\left(f_{2c} - f_2^a\right) \\ &= B\left(\frac{1-3p}{1+p}\right)^2 \left(f_{2c} - f_2^a\right) \end{aligned} \tag{4-19}$$

where $B = D_o \frac{T}{h\big|_{\substack{T\to\infty \\ p\to 0}}} \exp\left[-\frac{E_h}{RT}\right]$. Equation (4-19) may be expressed in terms of p, using equation (4-14):

$$\begin{aligned} r\frac{dr}{dp} &= B\left(\frac{1-3p}{1-p^2}\right)^2 \left(f_{2c} - f_2^a\right)\exp\left[\frac{E_a}{RT}\right] \\ &= B'\left(\frac{1-3p}{1-p^2}\right)^2 \left(f_{2c} - f_2^a\right) \end{aligned} \tag{4-20}$$

where $B' = \frac{D_o T}{Ah\big|_{\substack{T\to\infty \\ p\to 0}}} \exp\left[\frac{E_a - E_h}{RT}\right]$. The composition ϕ_{2c} is a function of *r* and *p* and the equilibrium composition is only dependent on *p*.

4.2.3. Coalescence

The coalescence process reduces the number of particles, but enlarges the size of particles. The number of particles making coalescence per unit time is proportional to the square of the number of particles and inversely proportional to viscosity. Therefore, the net rate of change in the number of particles per unit volume can be expressed in terms of *p* using the following equation:

$$\begin{aligned} \frac{dN_V}{dp} &= \frac{dn}{dp} - \frac{4kT}{3Ah} N_V^2 \exp\left[\frac{E_a}{RT}\right] \frac{1}{(1-p)^2} \\ &= \frac{dn}{dp} - \frac{4h\big|_{\substack{p\to 0 \\ T\to\infty}} kT}{3A} \left(\frac{1-3p}{1-p^2}\right)^2 N_V^2 \exp\left[\frac{E_a - E_h}{RT}\right] \end{aligned} \tag{4-21}$$

We need to know how the sizes of particles are changed by coalescence. It is algebraically difficult to determine which particles and how many of them are colliding to form larger particles. It may be possible to calculate the average radius resulting from coalescence at a certain *p*. However, coalescence hardly occurs with a low initial rubber composition, and thus we may make the simplifying assumption of neglecting this coalescence process when the rubber volume fraction is less than 0.1.

4.2.4. Mass Balance

Once the values of N_V and *r* have been obtained at a certain *p*, the volume fraction of the dispersed phase particles at *p* can be calculated from the following equation:

$$V_d(p) = \frac{4p}{3} r(p)^3 N_V(p) \tag{4-22}$$

Because the initial rubber composition and the number and size of particles are now known, an expression can be written for the mass balance:

$$\begin{bmatrix}\text{Total amount} \\ \text{of rubber}\end{bmatrix} = \begin{bmatrix}\text{Amount of rubber} \\ \text{in particle phase}\end{bmatrix} + \begin{bmatrix}\text{Amount of rubber} \\ \text{in matrix phase}\end{bmatrix}$$

$$f_{2o} = f_{2N}(p) \times V_d(p) + f_{2c}^{new}(p) \times (1 - V_d(p)) \tag{4-23}$$

Therefore, the following equation can be obtained from the rearrangement of equation (4-23) for the new rubber composition in epoxy phase, ϕ_{2c}^{new}, which results from the phase separation process during the small increment of conversion, δp:

(4-24) $$f_{2c}^{new}(p) = \frac{f_{2o} - f_{2N}(p)V_d(p)}{(1-V_d(p))}$$

4.3. COMPUTATIONS

The Euler method was used to numerically solve the differential equations (4-16) and (4-20) in the range, $p_{cl} \pounds p \pounds p_{gel}$. With a small increment, h, of p from the p_{cl}, solving equation (4-16) gives the number of nuclei born at each p. In this calculation, the $\boldsymbol{E_F}$ and DG_c at $\phi_{2c}(p)$ can be determined as explained in Figure 4-2. Similarly, radius of the dispersed particles at each p can be obtained using equation (4-20).

Let us consider the rubber composition of the dispersed phase. The rubber composition of a newly forming phase at a certain conversion p_j is determined from Figure 4-2 and is denoted by $\phi_{2N,j}$. While the nuclei born at this conversion will have the rubber composition, $\phi_{2N,j}$, previously born particles will grow further from a composition of $\phi_{2N,j-1}$ by the amount of rubber phase with the rubber composition of $\phi_{2N,j}$. The radius of particles born at conversion, p_i and grown until p_j can be denoted as $r_{i,j}$. It can be seen that a particle with radius of $r_{i,j}$ at the conversion, p_j, has the history of composition which has been $\phi_{2N,i}$, $\phi_{2N,i+1}$, $\phi_{2N,i+2}$,..., and $\phi_{2N,j}$. If the compositions inside the particle were in a stable region, they would dissolve to form a single homogeneous particle phase. Otherwise, the particle would show a concentric composition gradient. If it is assumed that the particles constitute a uniform homogeneous phase, then the rubber composition of a particle born at p_i and grown until p_j can be shown as

(4-25) $$f_{2N}(i,j) = \frac{1}{r_{i,j}^3}\sum_{k=i}^{j} f_{2N}(k,k)\left(r_{i,k}^3 - r_{i,k-1}^3\right)$$

Since the dispersed phase particles at the conversion p_j can possess a variety of rubber compositions ranging $\phi_{2N}(1,j)$, $\phi_{2N}(2,j)$, ..., and $\phi_{2N}(j,j)$, the average rubber composition of the dispersed phase, $<\phi_{2d}(j)>$, at p_j can be expressed as

(4-26) $$\left\langle f_{2d}(j)\right\rangle = \frac{\sum_{i=1}^{j} f_{2N}(i,j) r_{i,j}^3 n_i}{\sum_{i=1}^{j} r_{i,j}^3 n_i} = \frac{\sum_{i=1}^{j}\sum_{k=i}^{j} f_{2N}(k,k)\left(r_{i,k}^3 - r_{i,k-1}^3\right) n_i}{\sum_{i=1}^{j} r_{i,j}^3 n_i} = \frac{\sum_{i=1}^{j} f_{2N}(i,j) V_d(i,j)}{\sum_{i=1}^{j} V_d(i,j)}$$

where n_i is the number of nuclei born at conversion p_i and $V_d(i,j)$ is the volume fraction of the dispersed particles which were born at p_i and grown until p_j. The total volume fraction

of all the dispersed particles at p_j is then simply the sum of $V_d(i,j)$, i.e., $V_d(j) = \sum_{i=1}^{j} V_d(i, j)$. The following material balance equation (4-27) can then be used to obtain the new rubber composition of the continuous matrix phase.

$$f_{2cj} = \frac{f_{2o} - \frac{4p}{3}\sum_{i=1}^{j} f_{2N}(i, j) r_{i,j}^3 n_i}{1 - \frac{4p}{3}\sum_{i=1}^{j} r_{i,j}^3 n_i} = \frac{f_{2o} - \langle f_{2d}(j) \rangle V_{d,j}}{1 - V_{d,j}} \quad \text{(4-27)}$$

The average radius at conversion p_j can then be calculated using the following expression:

$$\overline{R_j} = \frac{\sum_{i=1}^{j} r_{i,j} n_i}{\sum_{i=1}^{j} n_i} = \frac{\sum_{i=1}^{j} r_{i,j} n_i}{N_{V,j}} \quad \text{(4-28)}$$

Therefore, the trajectory of f_{2c} as a function of p can be obtained by solving the equations (4-16), (4-20), (4-25), (4-26), and (4-27), simultaneously, at each degree of cure.

4.4. RESULTS AND DISCUSSION

4.4.1. Morphology Evolution for Isothermal Cure

A computational result for a sample with the initial rubber volume fraction of 0.1 cured at 70 °C will be analyzed in detail with respect to the extent of conversion in this section. Since DG_N is zero at the binodal conversion, p_{cl}, no phase separation occurs because no nuclei are born even if the size of nuclei is infinite. Hence, the composition of the continuous phase maintains the initial composition. As reaction proceeds, the equilibrium composition shifts to lower composition and thus there is such a finite value of DG_N where a significant number of nuclei can be generated with a finite size.

As presented in Figure 4-4 (a), significant phase separation starts at conversion of 0.245. During this process, the number ($N_V(p)$) of nuclei generated increases but the size of nuclei decreases. With so many nuclei being generated, the rubber component in epoxy phase transfers to the dispersed phase, and the epoxy molecules diffuse to the epoxy phase. Therefore, the rubber composition in the epoxy phase reduces rapidly toward the equilibrium composition. As the composition of the epoxy continuous phase approaches the equilibrium composition, DG_N decreases again. Thus the nucleus size born in this

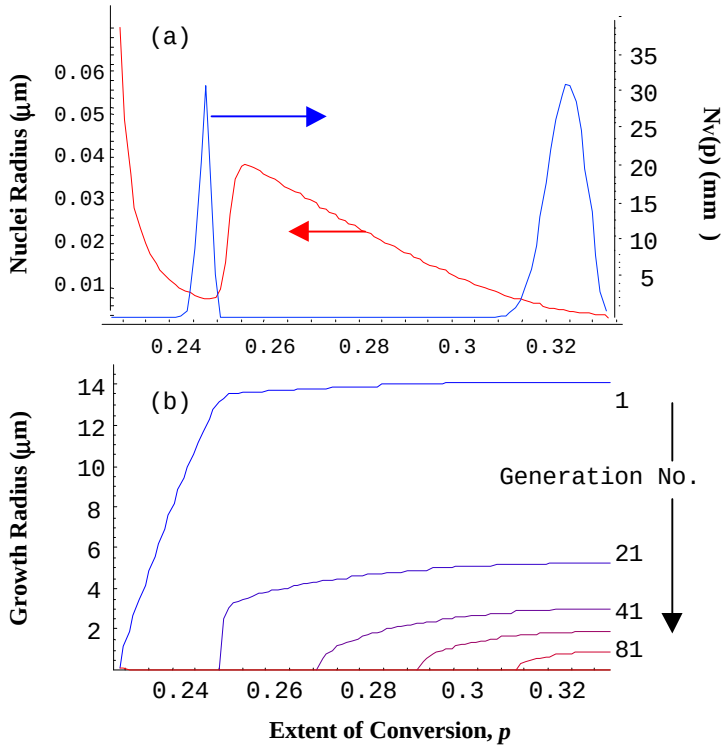

Figure 4-4. Size and number of nuclei generated at conversion (a) and growth of nuclei as function of conversion (b). Cure at 70 °C.

stage increases with the decrease in population. Then the system deviates again from the equilibrium curve and correspondingly generates more nuclei. Consequently, a bimodal type of particle size distribution may occur.

Although the growth rate of nuclei born at late conversion is greater than that of nuclei born at early conversion, there is no cross-over in terms of size between the old and young nuclei. This is because the total magnitude of growth allowed in the system at a given conversion is limited and thus is distributed between the old and young nuclei. Therefore, the oldest nuclei are the largest of all the nuclei if particles do not coalesce with each other. This situation is explained in Figure 4-4 (b). The growth of particles as well as the birth of a new generation of nuclei almost stops when the composition of the continuous phase is close to the equilibrium composition.

4.4.2. Influence of Temperature on Morphology Development

Figure 4-3 shows the trajectories of rubber compositions through conversion at two different cure temperatures. At a low cure temperature, 40 °C, the rubber composition in the continuous phase, ϕ_{2c}, follows the equilibrium curve, which implies that the phase separation rate is much faster than the polymerization rate. Correspondingly, the instantaneous rubber composition in the newly formed rubber rich phase, ϕ_{2N}, follows

in the conjugate part of the equilibrium curve. However, the average rubber composition in the dispersed phase is the weighted average for all particles present at the time (or the extent of conversion) of observation. Most of the phase separation has taken place by a conversion value of 0.23, and the particles generated at this conversion dominate the total volume of all particles. Therefore, the average composition of the dispersed phase does not change substantially after the conversion of 0.23.

In contrast to the low temperature cure, the composition, ϕ_{2c}, at a high cure temperature (160 °C) remains in the metastable region. At this temperature, the polymerization rate is faster than the phase separation rate. As a result of this, the rubber composition in the continuous phase cannot be changed significantly from the initial rubber composition and is therefore locked in a non-equilibrium state. Hence, the volume fraction of the dispersed phase must be negligibly small.

The trajectory of ϕ_{2c} at a median cure temperature would appear between the high and low temperature trajectory lines shown in Figure 4-3. The rubber composition in the continuous phase, ϕ_{2c}, after completion of phase separation should always be less than or equal to the initial rubber composition,ϕ_{2o}. Phase separation at low temperature starts at low conversion compared to phase separation at high temperature. Because of the strong dependency of viscosity on molecular weight, rapid approach to the equilibrium composition occurs at a low temperature cure.

The influence of cure temperature on the particle size distribution is demonstrated in Figure 4-5. As cure temperature increases, the distribution becomes narrower and it moves to smaller size. The number of particles increases to a maximum value and then decreases with an increase in the cure temperature. Below 100 °C, bimodal distribution is encountered. The population peak for small size particles disappears as cure temperature

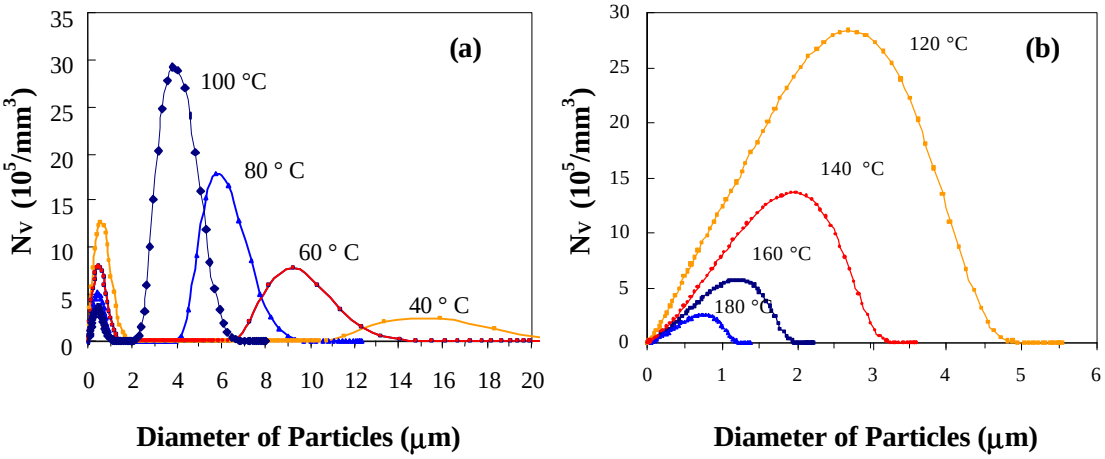

Figure 4-5. Effect of cure temperature on particle size distributions. (a) bimodal distributions and (b) unimodal distributions.

increases as shown in Figure 4-5 (a). These bimodal distributions appeared in the work of Gillham and Manzione[13] even though they did not remark on them. Above 100 °C, the number density of the particles decreases as temperature increases.

The effect of cure temperature on the final cured morphology is shown in Figure 4-6. While the number average radius has a maximum, the volume average radius continuously decreases as cure temperature increases. This is due to the presence of a bimodal distribution at low temperatures. The number of particles per unit volume passes through a maximum value at relatively high cure temperature (140 °C) and then decreases with an increase in temperature. The volume fraction of particles is more sensitive to changes in size than in the number density, i.e., $V_d \propto \bar{r}^{3} N_V$. In this relation, the volume average radius must be used in the case of a broad or bimodal distribution of particle size. As shown in Figure 4-6 (a)-(c), the volume fraction does not decrease as rapidly as the volume average radius does with an increase of temperature to 140°C. This is because the increase in the number density in the temperature prevents a considerable decrease in the volume fraction. However, at around 140°C, the volume fraction drops abruptly since the number density decreases above the temperature. At cure temperatures above 140 °C, the polymerization rate is so fast that the nucleation and growth processes are suppressed. This results in the generation of a low number of small rubber particles.

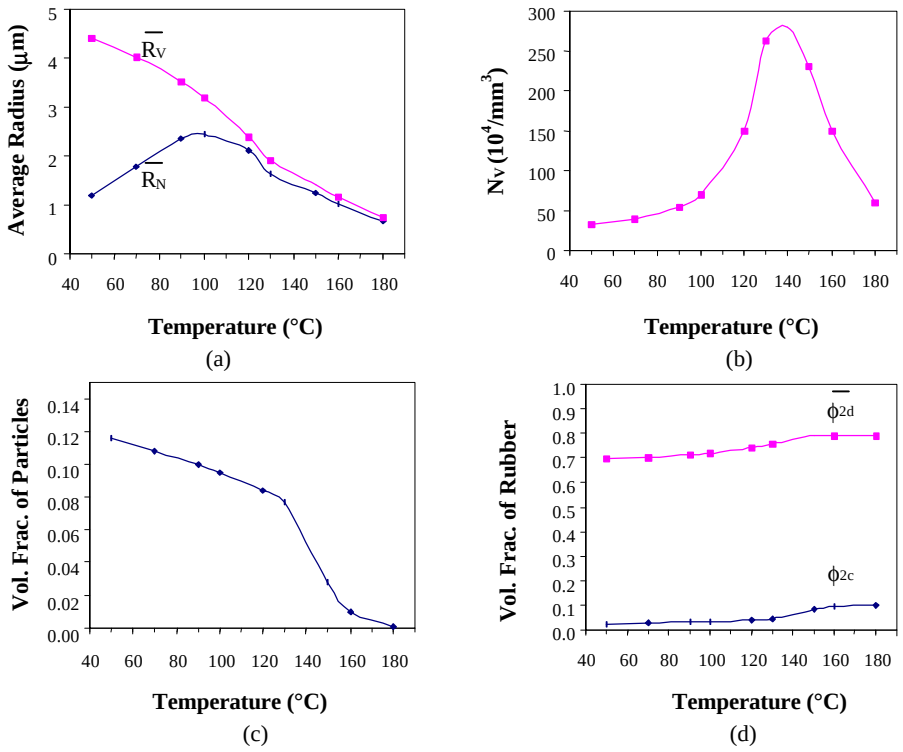

Figure 4-6. Effect of cure temperature on average particle sizes (a), number density (b) and volume fraction (c) of dispersed rubber particles and compositions of rubber in both of the phases (d).

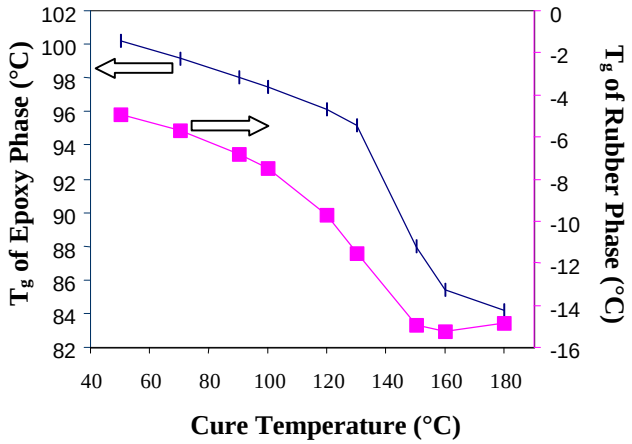

Figure 4-7. Glass transition temperature changes due to the rubber composition in both phases affected by different cure temperatures.

4.4.3. Glass Transition Temperatures

Since the whole equilibrium curve shifts down for lower cure temperature, the rubber composition in the continuous phase, ϕ_{2c} must be less at a low cure temperature than at a high cure temperature. Therefore, the glass transition temperature of the continuous phase will be depressed the least for a sample cured at the lowest temperatures due to the plasticizing effects of the dissolved rubber. This effect is shown in Figure 4-7. The extent of depression may be evaluated with the Fox equation:

$$\frac{1}{T_g} = \frac{W_R}{T_{gR}} + \frac{1 - W_R}{T_{gE}} \qquad (4\text{-}29)$$

where W_R is the weight fraction of the rubber component and T_g, T_{gR} and T_{gE} are glass transition temperatures of the epoxy-rubber mixture, pure rubber and pure epoxy, respectively.

Figure 4-6 (d) shows the changes in rubber compositions in both of the continuous and rubber phases as a function of cure temperature. Because of the amount of rubber dissolved in both phases even after the completion of phase separation, the glass transition temperatures of both phases would occur between those of the pure epoxy and the pure rubber. An estimate of the glass transition temperatures of both the continuous and rubber phases as a function of rubber composition can be obtained by using equation (4-29). For these calculations, it was assumed that the densities of the both epoxy and rubber were 1.0 g/cm^3. The glass transition temperatures of the neat epoxy thermoset and CTBN rubber were 105 °C and -35 °C, respectively, using values obtained from Manzione and Gillham's work[13]. The results are presented in Figure 4-7.

Many researchers have used the Fox equation and measured the glass transition temperatures of the rubber modified epoxy, neat epoxy and the pure rubber in order to back calculate the composition of rubber dissolved in the epoxy phase. This method appears to be somewhat inaccurate in estimating the rubber composition in the epoxy phase. Notice that a change in cure temperature from 50 °C to 180 °C leads to a change in the rubber composition in the epoxy phase from 2.2 % to 9.9 %. In this system, T_g is depressed by about 1 °C for each 10 °C change in cure temperature range of 50 °C to 100 °C. The maximum depression of about 8 °C may be detected for the piperidine-cured epoxy if cure temperature changes from 100 °C to 150 °C. It would be very difficult to measure the glass transition temperature accurately enough to discern the composition difference. Manzione and Gillham[13] mentioned that significant evaporation of piperidine occurs above 150 °C. A low cross link density also results in depression of T_g.

Gillham has shown how the time temperature transformation diagram can be modified to include the phase separation phenomena[14]. In this work, Gillham described that for the same weight percent rubber modifier loading, different isothermal temperatures varied the size and number density of the phase separated particles.

They observed that higher temperatures gave larger domains in a less dense phase separated medium as we expected in Figure 4-6 (a). Lower cure temperatures resulted in a higher population of smaller diameter rubber particles. Viscosity was suggested to be of primary importance in the morphological development. Gillham studied how viscosity influenced the domain formation, and related the varying extents of phase separation to the competing effects of thermodynamic compatibility, and diffusivity of the growing spheres[13]. It was explained how dispersed particles formed at a 90°C cure had phase-separated in a more viscous medium than those formed at a 150°C cure. Consequently, the corresponding cloud point of the 90 °C cure medium occurred at a later isothermal hold time than the cloud point from the 150 °C cure. This is true, but this does not tell if

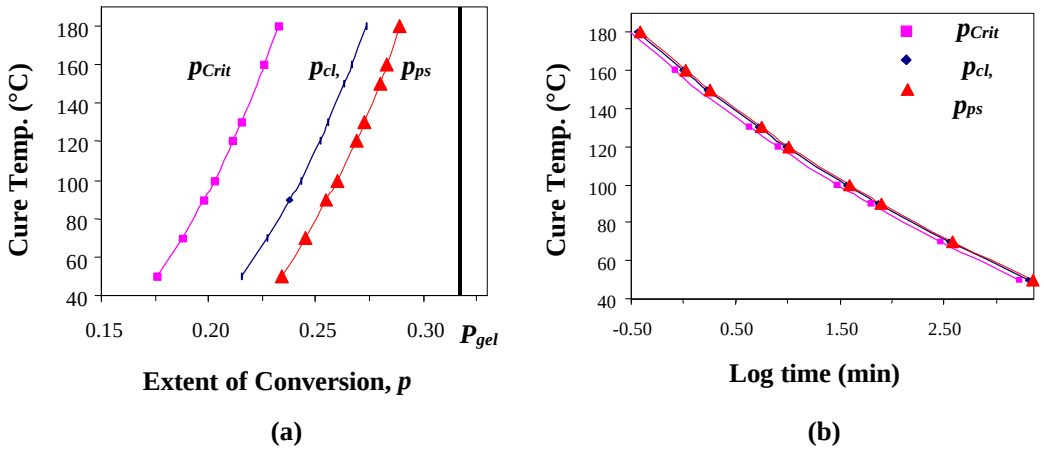

Figure 4-8. Contours of critical, equilibrium (binodal), and expected phase separation points in the conversion-temperature space.

the phase separation for low temperature cure occurred in a more viscous state or not. Their analysis scheme was too simple to explain other systems which show the opposite behavior of morphology to their observations: that is, small but numerous particles are formed at high temperatures of cure.

The critical, equilibrium, and actual onset curves for phase separation were plotted in the temperature-conversion domain and the temperature-time domain as shown in Figure 4-8. The onset point of phase separation was taken as the incipient point from the accumulated number density fraction plot as presented in Figure 4-9. Morphological development was essentially quenched as the gel point was reached. The phase separation "window" may be defined as the difference in time between the gel point and the cloud point:

$$\Delta t_{ps} = t_{gel} - t_{cl} \qquad \Delta p_{ps} = p_{gel} - p_{cl} \tag{4-30}$$

In this phase separation (Δp_{ps} or Dt_{ps}) window, the diffusivity decreases continually during the cure while viscosity increases with increasing network formation. Conversely, the increase in molecular weight associated with network formation is the major driving force for phase separation.

4.5. CONCLUSIONS

A model which can describe phase separation process during polymerization reaction has been developed on the basis of thermodynamics of a binary mixture combined with nucleation and growth rates. This model was applied to a rubber modified epoxy thermoset with a functionality of four. The morphological changes of this reaction system as a function of conversion were analyzed in the framework of the modified model.

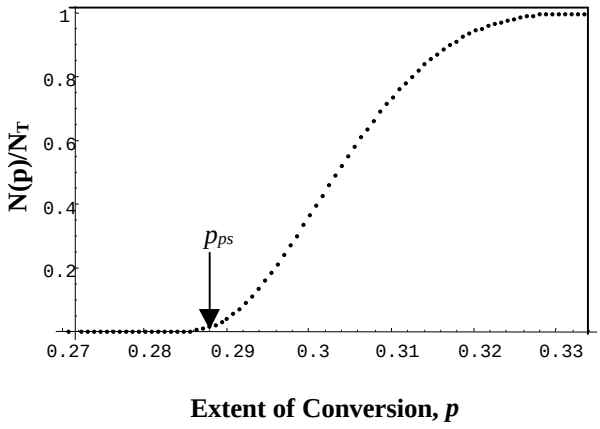

Figure 4-9. Accumulated number of particles as a function of p at cure temperature of 120 °C.

It should be noted that some simplification was made for the illustration of phase separation during the cure reaction in the calculation. The cure reaction was assumed to follow simple second order kinetics. When epoxy resins are cured with diamine curing agents, a hydroxyl group produced by the epoxide ring opening reaction catalyzes the other ring opening reaction. Therefore, the simple second order kinetic expression may be inadequate. Furthermore, the viscosity of the epoxy was assumed to be proportional to the second power of molecular weight for simplicity. In order to predict the morphological characteristics of other rubber modified thermosets, the Flory-Huggins interaction parameter, the reaction kinetics, and the viscosity dependence with respect to temperature as well as conversion should be well defined.

This model was restricted by the initial rubber composition so that phase separation could occur only in a metastable region. It is often found that the initial rubber composition is close to the critical composition, and the cure temperature is sufficiently high to speed up the polymerization reaction. In this case, the phase separation may occur through spinodal decomposition. It is also a possible for a system to phase separate by nucleation and growth in an early stage followed by the spinodal decomposition in a later stage or vice versa. These cases will be discussed qualitatively with some examples of micrographs. Combining the spinodal decomposition theory with the nucleation and growth mechanism may extend the applicability of this model to a high initial rubber composition.

This model also neglected the possibility of the coalescence. A statistical treatment can be used for setting the positions of nuclei in a three-dimensional space. It can be assumed that when particles collide to form a new larger particle, the new particle is located in the center of the colliding particles. The radius of the new particle can be calculated from the total volume of the colliding particles. Therefore, the assumption of neglecting the coalescence process can be avoided.

It is of interest to study a diglycidyl ether of bisphenol A (DGEBA) type of epoxy cured with stoichiometric amount of diaminodiphenyl sulfone (DDS) in the presence of ETBN rubber. Experimental measurements for this system are discussed in the next chapter in order to determine the input parameter values needed for prediction of the morphologies as well as to compare the calculated results with the experimentally observed morphologies. The correlation of fracture toughness with the morphology will be made in later chapters.

4.6. REFERENCES

1. S. Kunz-Douglass, W. R. Beaumont, M. F. Ashby, *J. Mater. Sci.*, **26**, 907 (1980).
2. a) A. J. Kinloch, In ***Rubber-Toughened Plastics***; C. K. Riew, Eds.; Advances in Chemistry 222; American Chemical Society: Washington D.C., 1989; p. 68.

   b) A. J. Kinloch, D. L. Hunston, *J. Mat. Sci. Lett.*, **6**, 131 (1987).
3. S. C. Kunz, J. A. Sayre, R. A. Assink, *Polymer*, **23**, 1897 (1982).
4. R. J. J. Williams, J. Borrajo, H. E. Adabbo, A. J. Rojas, In ***Rubber-Modified Thermoset Resins***; Riew, C. K.; Gillham, J. K., Eds.; Advances in Chemistry 208; American Chemical Society: Washington D.C., 1984; pp. 195-213.
5. A. Vazquez, A. J. Rojas, H. E. Adabbo, J. Borrajo, R. J. J. Williams, *polymer*, **28**, 1156 (1987).
6. K. Yamanaka, T. Inoue, *Polymer*, **30**, 662 (1989**)**.
7. K. Yamanaka, Y. Takagi, T. Inoue, *Polymer*, **60**, 1839 (1989).
8. K. Yamanaka, T. Inoue, *J. Mat. Sci.*, **25**, 241 (1990).
9. P. J. Flory, "Principles of Polymer Chemistry", Cornell University Press, Ithaca, N.Y., 1953.
10. W. H. Stockmayer, *J. Chem. Phys.* **11**, 45 (1943).
11. J. W. Cahn, J. E. Hilliard, *J. Chem. Phys.*, **28**, 258 (1958).
12. T. K. Sherwood, R. L. Pigford, C. R. Wilke, "**Mass Transfer**", McGraw-Hill, New York, **1975**, p. 215.
13. L. T. Manzione, J. K. Gillham, C. A. McPherson, *J. Appl. Polym. Sci.*, **26**, 889 (1981).
14. J. K. Gillham, in "**Role of the Polymeric Matrix in the Processing and Structural Properties of Composite Materials**", J. C. Seferis, L. Nicolais, Eds.; Plenum Press, New York, 1983, p. 133.

Chapter 5: KINETICS OF EPOXY-AMINE CURE

5.1. INTRODUCTION

The competition between the rates of polymerization and phase separation leads to different morphology of the final cross-linked network system. The resulting morphology as well as the chemical structure of the cured network will affect the physical properties of the cured material. In order to separate the effect of morphology from the effect of the state of the cured network on a physical property, it is essential for materials being compared to be cured to the same extent of cure. The study of cure kinetics will provide information about proper cure schedules (cure times and temperatures) to make the same cross-linking state of the cured materials. In order to predict the morphology developed by the phase separation of rubber rich phase during the polymerization of epoxy resin with amines, it is necessary to know the reaction kinetics of the cross-linked polymer system. It is these reasons, in addition to exploring the reaction mechanism, that cure kinetics is worth studying .

Curing thermosetting materials generally involves the transformation of low molecular weight liquids to amorphous networks with infinite molecular weight by means of exothermic chemical reactions. The chemo-rheological changes during the reaction can be rationalized using the isothermal time-temperature-transition diagram[1-3]. The state of the material is governed by chemical conversion and temperature. Knowledge of the cure rate and its dependence on temperature and conversion is important for predicting the course of the reaction for a certain thermal treatment.

When a thermosetting polymer is cured at a temperature substantially below the glass transition temperature of the fully cured network, $T_{g\infty}$, the glass transition temperature of the growing network, T_g, will rise to the cure temperature, T_{cure}. The accompanying transition of a liquid state or rubbery state to a glassy state is called vitrification[3]. The chemical kinetics in the region near vitrification is often complicated by diffusion and/or mobility control. In principle, the reaction can proceed until T_g exceeds the cure temperature to a point where all chain movement ceases, so that the configurational entropy of the chain approaches zero, and the reaction arrests due to the "complete" absence of mobility. This leads to a final conversion lower than unity in diffusion-controlled conditions. Note that the ultimate conversion can also be lower due to topological limitations, namely the fact that remaining reactive groups cannot meet and react even in the absence of any diffusion hindrance. In any case, reaching this ultimate conversion would take an infinite time.

5.1.1. Mechanism of Epoxy-Amine Cure

In order to investigate the reaction kinetics, a suitable kinetic expression should be selected so that experimental data can be fitted into it to find the kinetic parameters. The cure of epoxy resins has been considered an autocatalytic reaction and can be described by the semi-empirical rate equation[4-6]

$$\frac{da}{dt} = \left(k + k'a^{m}\right)(1-a)^{n} \qquad (5\text{-}1)$$

where k and k' are the apparent kinetic rate constants for the non-catalyzed and the autocatalyzed reaction paths, respectively, and m and n are the reaction orders. The hydroxyl groups in DGEBA molecules are associated in the epoxide ring opening process by the amine group, and the hydroxyl group is generated in each ring opening reaction. The extent of conversion, α, can be defined in several ways as will be discussed later. For the purpose of illustration, we may define the extent of conversion, α, as

$$a = \frac{[E]_0 - [E]}{[E]_0} \qquad (5\text{-}2)$$

where [E] denotes the concentration of epoxide group at time t and the subscript 0 denotes time t=0.

Looking carefully into the reaction schemes for the epoxy cure would give better understanding of why and how the semi-empirical rate equation (equation (5-1)) can be used for describing the epoxy cure reaction. Major possible reaction paths for the epoxy cure can be drawn as

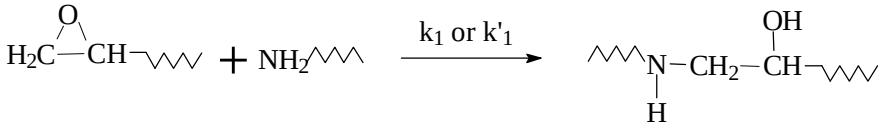

(5-3)

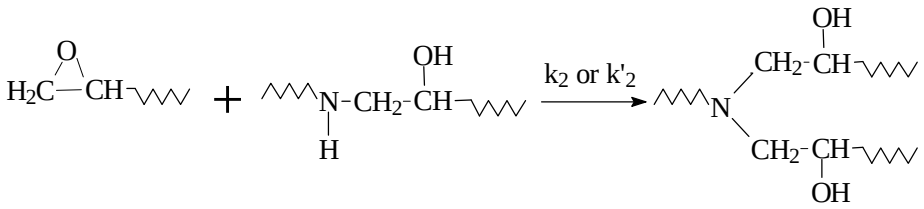

(5-4)

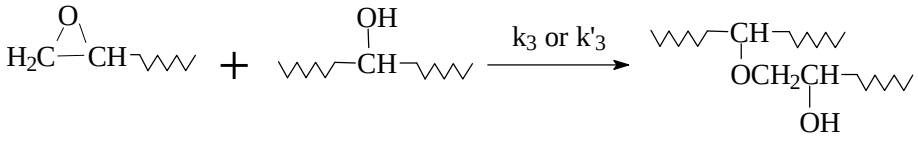

(5-5)

The primary amine reaction with an epoxide yields a secondary amine via catalyzed or non-catalyzed reaction paths, as stated in equation (5-3). The secondary amine produced in reaction step (5-3) can react further to form tertiary amine (equation (5-4)). The epoxide ring opening reaction can take place with amines or hydroxyl groups present in DGEBA epoxy molecules. All of these reactions are either catalyzed or non-catalyzed by hydroxyl groups, which are present in the initial epoxy molecules, or produced during the ring opening reaction. Other possible reaction paths may be the homopolymerization of epoxy groups by Lewis base (i.e., tertiary amines) or Lewis acid catalysts (i.e., BF_3 complexed with an amine). However, this reaction will be insignificant because the tertiary amine produced by the reaction step (5-4) is sterically hindered[7].

The etherification reaction (equation (5-5)) may also be neglected for stoichiometric mixtures of epoxy resins with aliphatic diamines since the reactivity of the diamines to the epoxide rings is much stronger than the hydroxyl groups[7,8]. Horrie *et al.* set forth the reaction scheme using only equations (5-3) and (5-4) and assuming the ratio of the secondary amine reaction rate to the primary amine reaction rate is constant and independent of temperature.

$$\frac{k_2}{k_1} = \frac{k_2'}{k_1'} = g \tag{5-6}$$

By denoting the concentrations of primary amine, secondary amine and hydroxyl group at reaction time t as $[A_1]$, $[A_2]$, and $[C]$, respectively, and the epoxide concentration consumed after time t as x, the rate for disappearance of epoxide group is written as

$$\frac{dx}{dt} = \left(k_1[C]_0 + k_1'x\right)\left([A_1] + g[A_2]\right)\left([E]_0 - x\right) \tag{5-7}$$

Since the hydroxyl group is produced for each epoxide ring opening, the concentration of hydroxyl group at time t is expressed as

$$[C] = [C]_0 + [E]_0 - [E] = [C]_0 + x \tag{5-8}$$

The relation between $[A_1]$ and $[A_2]$ can be found from the mass balance:

$$[A_1]_0 = [A_1] + [A_2] + [A_3] \tag{5-9}$$

$$[E]_0 = [E] + [A_2] + 2[A_3] \tag{5-10}$$

where $[A_3]$ is the concentration of tertiary amine. Eliminating $[A_3]$ in equations (5-9) and (5-10) and replacing $[E]_0$-$[E]$ by x, one obtains

$$[A_1] + [A_2]/2 = [A_1]_0 + x/2 \tag{5-11}$$

When the reactivity of each hydrogen on the primary amine is equal to the reactivity of a hydrogen on the secondary amine, the ratio of rate constants γ becomes 0.5. Since the

basicity of secondary amine is usually considered to be close to that of primary amine, it is not a bad approximation that the ratio γ is close to 0.5 and can be written as

(5-12) $$g = 0.5 + \Delta g$$

The value for aromatic diamines generally falls in the range between 0.38 and 0.46[9-11]. Substitution of equations (5-11) and (5-12) into equation (5-7) leads to

(5-13) $$\frac{dx}{dt} = \left(k_1[C]_0 + k_1'x\right)\left([E]_0 - x\right)\left([A_1]_0 - \frac{x}{2}\right)\left(1 + \frac{2[A_2]\Delta g}{2[A_1] + [A_2]}\right)$$

The term $\frac{2[A_2]\Delta g}{2[A_1] + [A_2]}$ in equation (5-13) is negligibly small compared to unity. As the reaction proceeds, $[A_1]$ monotonically decreases from $[A_1]_0$ at initial reaction time to zero at the time of completion for stoichiometric reaction, while $[A_2]$ increases to a maximum value and decreases to 0 at the completion. Since $[A_1] >> [A_2]$ at the initial stage of reaction, the term is so small as to be neglected. When $[A_1] = [A_2]$, the value becomes 0.67 Δγ. Complete reaction will force it to approach 2Δγ since $[A_1] = 0$. Therefore, the term can be neglected for the system with a small value of Δγ.

Since $[A_1]_0=2[E]_0$ for the stoichiometric reaction and if we ignore the term $\frac{2[A_2]\Delta g}{2[A_1] + [A_2]}$ in equation (5-13), $\left([A_1]_0 - \frac{x}{2}\right) = \frac{[E]_0}{2}(1 - a)$. Hence equation (5-13) reduces to a form of equation (5-7) with m=1 and n=2:

(5-14) $$\frac{da}{dt} = \left(K + K'a\right)(1 - a)^2$$

where $K' = \frac{k_1'[E]_0^2}{2}$ and $K = \frac{k_1[E]_0[C]_0}{2}$.

Horie *et al.* analyzed their kinetic data obtained from isothermal DSC experiments[4]. Assuming equation (5-14) represent the true kinetic behaviors of the materials that they employed, the plot of $da/dt/(1-\alpha)^2$ against α was fitted to a linear equation. The slope and the intercept correspond to K and K', respectively. Repeating the same procedures at different temperatures, they obtained the pre-exponential factors and activation energies from the Arrhenius plot of rate constants against temperature. It should be pointed out that the rate equation was derived under the assumptions of no etherification and no diffusion control effect (see later sections). Therefore, discrepancies of experimental data from the proposed reaction kinetics, particularly at high conversion, are inevitable. When the data are fitted to the linearized rate equation where $m+n=3$, the discrepancies due to diffusion, unequal reactivity and other side reactions will be distributed to other kinetic parameters such as the two apparent rate constants that contain the pre-exponential factors and activation energies.

Riccardi and Williams derived a rate equation that took into account the etherification. They claimed that the etherification becomes significant at high temperature cure of DGEBA/DDS system[10]. In their derivation, the concentration of amine hydrogen was used rather than that of amine. Therefore, the concentration of primary amine is half of that of the primary amine hydrogen and as a result the reactivity ratio between secondary and primary amine hydrogen becomes unit if both primary and secondary amines have the same reactivity. However, in the analysis of their data, they assumed the value of 0.4 as was quoted in the literature[9] for aromatic diamines. For their analysis, it must have been 0.8 because the literature value was based upon the amine concentration. They fixed the reaction orders as 2 with respect to (1-α) and 1 with respect to α, and fitted the isothermal experimental data to their derived rate equation. Therefore, the errors must be contained in the estimated rate constants at the cure temperature and consequently in the estimation of activation energies and pre-exponential factors.

5.1.2. Diffusion Controlled Reaction Regime

Since the extent of conversion was defined as a function of the concentration of reacting group shown in equation (5-2), the reaction kinetics expressed by equation (5-7) or (5-13) explains only chemically controlled reactions. As the reaction progresses at high conversion, the diffusion control effect should be taken into account. Curing thermosetting materials generally involves the transformation of low molecular weight liquids to amorphous networks with infinite molecular weight by means of exothermic chemical reactions. Van Assche *et al.*[6,12] have introduced a mobility factor to obtain the pure kinetic rate from the rate observed by quasi-isothermal modulated DSC that is obliterated by diffusion control effect at late conversion. Barton[13] have used a kinetic equation to take into account the diffusion control of cure reactions:

$$\frac{da}{dt} = \left(A_0 + A_1 a + A_2 a^2\right)(1-a)^n \qquad \text{(5-15)}$$

The discrepancies occurred in isothermal experiments are mainly due to the effect of the diffusion control. Many researchers have tried to modify the kinetic equation for isothermally measured data to describe the late reaction behavior to take account for the effect of the diffusion control. The isothermal technique may show a curing reaction to converge at maximum a certain degree of conversion far less than one. In contrast, since the delayed reaction due to the diffusion control is contained in the residual reaction exotherm, the degree of conversion defined by this technique runs from zero to 1. Equation (5-1) may be used to describe the whole conversion range if the reaction orders are not constrained to 1 and 2 for *m* and *n*.

This chapter investigates the reaction kinetics for the system of neat epoxy, DGEBA/DDS, and rubber modified epoxy, DGEBA/DDS/10 % ETBN, using differential scanning calorimetry techniques. The estimated kinetic parameters for these systems can be used to construct the time-temperature-transformation diagrams which useful information can readily obtained from. The phase transition phenomena can be incorporated in the TTT diagram by measuring the cloud points. The measurements of

cloud points were performed by monitoring the light intensity change due to phase separation during the reaction as a function of time and temperature. A dynamic mechanical analyzer was used to measure the time to gelation and time to vitrification at different temperatures. These data were compared with those obtained from DSC data, which might verify whether the analysis tool employed for the reaction kinetics is suitable or not.

5.2. ANALYSIS TECHNIQUES FOR DSC

The reaction kinetics can be explored using several techniques: for example, differential scanning calorimetry (DSC), Fourier-transform infrared spectroscopy (FTIR), solid-state ^{13}C nuclear magnetic resonance (NMR), or size exclusion chromatography (SEC). The fundamental concepts are the same in the sense that all techniques monitor the changes occurred during the reaction as a function of time and temperature. For instance, DSC measures the heat generated during the cure reaction at certain temperature and time. It is assumed that the heat generated is proportional to the consumption of epoxy equivalent at time *t*. The change (ΔH in DSC) can be normalized by the total change (or total ΔH in DSC) from the initial state to the final state to define the extent of conversion at a certain time.

5.2.1. Isothermal Technique

One way to explore the extent of conversion as a function of time is to monitor the heat change occurring during the reaction as a function of time at a constant temperature at which unreacted samples are reacting in the DSC sample cell. This is a direct method for measuring the heat generated with time as the low molecular weight resin transforms to an infinite crosslinked three-dimensional network. If the change is measured from the initial state, the extent of conversion, α, can be defined as

$$a = \frac{\Delta H(T,t)}{\Delta H_0} \qquad (5\text{-}16)$$

where $\Delta H(T,t)$ is the heat generated at the isothermal temperature, T, till time, t, and ΔH_0 is the total maximum heat obtained to complete the reaction.

For the isothermal technique, difficulties arise from the uncertainty of the measured total heat of reaction[14]. The heat flow at the initial reaction state is obliterated by temperature equilibration of the DSC cells. Furthermore, the rate of the reaction is largely controlled by a diffusion process at the high conversion and thus the heat flow is substantially leveled off. Because the total heat increases with an increase in the isothermal temperature, ΔH_0 is practically obtained from the integrated area of the exothermic peak in the temperature scanned thermogram. The isothermal run of DSC at a certain temperature, T, provides $\Delta H(T,t)$ by integrating the thermogram from time $t = 0$

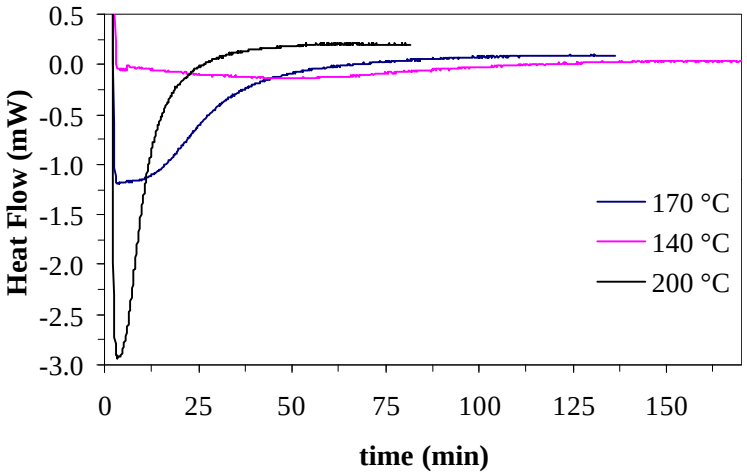

Figure 5-1. Isothermal thermograms of DGEBA/DDS/10% ETBN with stoichiometric ratio of DDS to epoxy.

to t. The problem is that $\Delta H(T,t)$ for completion at an isothermal temperature, especially at low temperatures, is much less than ΔH_0. Such an observation is interpreted by some researchers as being the dominant effect of diffusion at a late stage of the reaction[13,15]. Some typical isothermal thermograms are presented in Figure 5-1.

The isothermal mode offers the advantage of greater simplicity of interpretation of the data, leading to greater confidence in the values of derived kinetic parameters. Nevertheless, an isothermal method becomes unreliable for fast cures because one or two minutes are needed for the sample and test cell to heat up to the desired temperature, and the initial portion of the exotherm is partially obliterated by the heat absorbed as the sample warms up. Furthermore, the total heat of reaction (ΔH_0) varies with cure temperature, 107 J/g at 140°C to 250 J/g at 200°C for DER331/DDS/ETBN system. It is recognized that undercure may contribute to the low values at lower temperatures. However, the subsequent scans of the isothermally cured samples with a heating rate of 10°C/min yielded the residual exotherms (81 J/g for 140°C cured sample and 13 J/g for 200°C cured one). Thus this only partially explains the large differences. It is also possible that the cure mechanism changes with temperature.

5.2.2. Dynamic Temperature Scan

The second technique is a dynamic scanning mode which monitors heat flows as temperature varies linearly with time. The utilization of this dynamic technique usually involves the assumption of a constant specific heat or a linear variation of specific heat with scanning temperature. In the dynamic scanning mode, both the temperature and degree of cure varies simultaneously[16,17]. Also the reaction mechanism is assumed not to change with conversion in the range of reaction temperature. The estimated parameters

using this method will be compared later with the ones estimated by the residual exotherm technique.

5.2.3. Residual Isothermal Technique

The reaction kinetics can be explored using a residual exotherm technique. In this technique, samples are cured isothermally in an oven for times ranging from zero to the time required for "completion". Each partially cured sample is then scanned in the DSC cell at a certain rate. From the measurements of the area enclosed by the thermogram and the base line, the residual heat evolved to the completion of the reaction, $\Delta H_R(T,t)$, can be determined and thus the extent of conversion, α, can be defined as

$$a = 1 - \frac{\Delta H_R(T,t)}{\Delta H_0} \qquad (5\text{-}17)$$

where $\Delta H_R(T,t)$ is the residual heat evolved to the completion of the reaction for the partly cured sample for the period of time, t, at an isothermal cure temperature, T.

It is assumed that the reaction undergoes to completion when any apparent exothermic peaks do not appear in a DSC thermogram, even if some reactive groups remain unreacted after the scan due to their topological limitation in the cross-linked network. Therefore, it is possible to have the extent of cure equal to unit when the thermogram of a sample did not show an exothermic peak.

Some typical thermograms as a function of time are provided in Figure 5-2, where the exothermic reaction peaks appear in single and smooth curves. This indicates that the reactivities of primary to the epoxide ring can be treated the same as that of secondary amine in the cure temperature range employed. The measured data points of conversion and time, (α, t), are shown in Figure 5-3 along with curves that were computed from the integrated kinetic equation. One of the advantages of using this technique is that the glass transition temperature can be obtained simultaneously with the reaction exotherm at a certain time and temperature.

Since we defined the extent of conversion as the relative residual heat for partially cured samples rather than the consumption of reactive components, the extent of conversion is dependent not only on the concentration of the reactants, but the mobility of the reacting species. The complete reaction is defined as a state that does not give off heat even when it is rescanned in the DSC within a temperature range excluding any significant oxidative or other chemical reactions. In the analysis of the experimental data, the reaction orders were no longer restricted and the non-catalytic rate constant were ignored because the autocatalytic reaction is dominant in the presence of hydroxyl group. In this respect, many researchers[18,19] have used the following rate expressions to analyze their data into;

$$\frac{da}{dt} = k a^m (1-a)^n \qquad (5\text{-}18)$$

Table 5-1. Epoxy formulations used in this investigation

System ID	DER-331 (g)	DDS (g)	KELPOXY (g)
NT-xxx	75.08	24.92	0
RES-xxx	52.88	22.12	25.00

where *k* is the apparent rate constant, *m* is the reaction order that is related to the effectiveness of catalytic reaction, and *n* is the reaction order which is related to depletion of epoxide ring and amine groups.

5.3. EXPERIMENTAL

5.3.1. Sample Preparation

The formulation for rubber modified epoxy was adjusted to provide 10 wt % rubber in the whole system (DGEBA/DDS/ETBN) and to keep a stoichiometric proportion of DDS with respect to the sum of epoxides coming from DGEBA and ETBN. The formulations for rubber modified epoxy as well as for neat epoxy are given in Table 5-1. A bulk mixture of KELPOXY and DGEBA was made in an oil bath at 90 °C with nitrogen purge. It was readily mixed to a homogeneous solution. A stoichiometric amount of DDS was added into the mixture and carefully stirred at 130°C until homogeneous solution was achieved. For the DSC samples, 3-5 g of the mixture was prepared and it took less than 10 min to make a homogeneous solution. This period of mixing was ignored in the kinetic experiments.

5.3.2. DSC

Both Perkin-Elmer DSC-7 and TA 2920 were used to measure the glass transition temperatures and residual heat of the partially cured samples at 10°C/min under nitrogen atmospheres. About 10 mg of samples was placed in DSC pans, and they were cured in a convection oven preheated at a desired temperature for predetermined time. The samples cured for shortest times were tested first while the other was cured in the oven. If a sample was taken out the oven before it was ready for the DSC scanning, it was quenched in the liquid nitrogen and stored in a refrigerator (-25°C). For unreacted samples, the aluminum sealed pans from SEIKO were used to prevent contamination of the DSC cell. The glass transition temperatures were taken from the point where the distance from the baseline of the glass region is equal to that of the melt region. The area of exothermic peak was integrated from the straight baseline.

5.3.3. DMTA

A Netzsch dynamic mechanical thermal analyzer (DMTA) was employed to confirm the reaction kinetics determined from DSC residual heat measurements. Unreacted liquid samples were coated on a braid of glass fibers. The samples were cured at selected isothermal temperatures during DMTA run using the dual cantilever bending mode at multifrequency. The instrument was preheated about 20 °C to 30 °C above the selected temperatures because the oven temperature dropped while the sample was mounted to the sample holder.

5.3.4. Light Transmission Device

The homogeneous mixture of rubber with epoxy resin takes phase separation during cure. Since the clear sample turns to opaque, using light transmission device allows one to obtain the time for it to become cloud. An optical microscope (Olympus BX50) attached with an optometer was used to obtain cloud points. The sample was placed in a hot stage that controlled temperature. The light intensity in a unit of voltage was collected as a function time at an isothermal temperature in a computer. The decrease in the intensity of the transmitted light indicates phase separation.

5.4. RESULTS AND DISCUSSION

Some typical thermograms as a function of time are provided in Figure 5-2, where the exothermic reaction peaks appear in single and smooth curves. This indicates that the reactivities of primary and secondary amine with the epoxide ring (equations (5-2) and (5-3)) can be treated to be equal in the reaction system employed. The measured data points of conversion and time, (α, t), are shown in Figure 5-3 along with curves that were drawn from the integrated kinetic equation with determined parametric values. The analytical methods will be explained in the following paragraph.

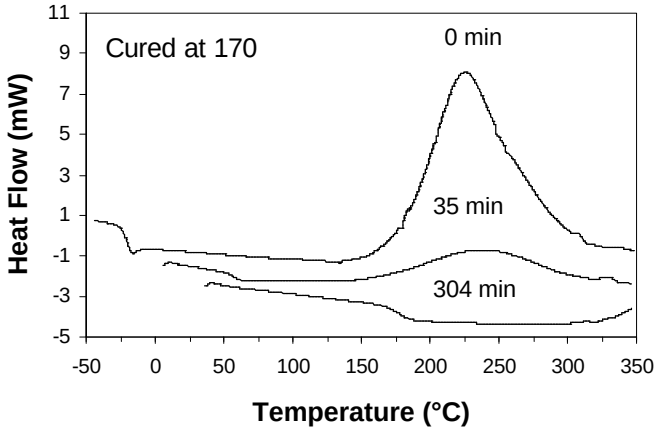

Figure 5-2. Thermograms for partially cured samples of DGEBA/DDS at 170 °C.

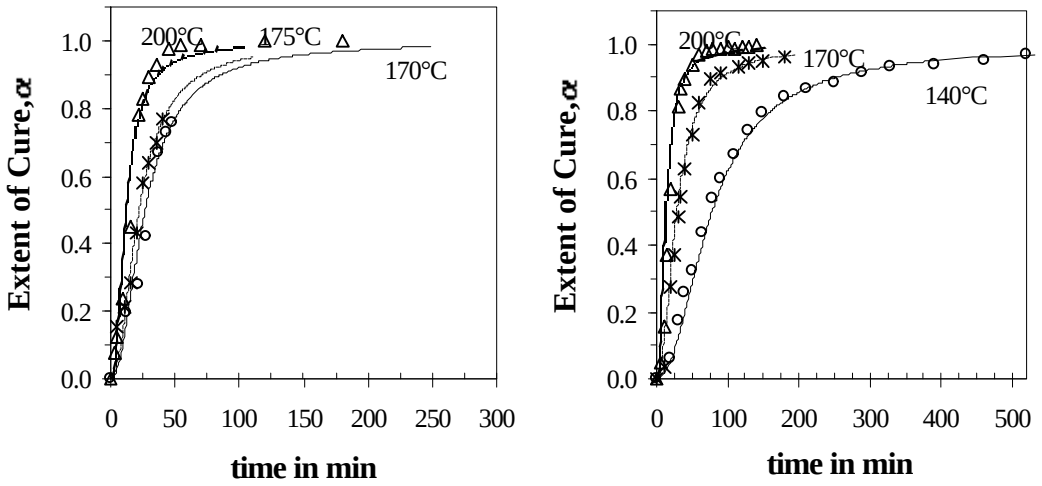

Figure 5-3. Isothermal curves for (a) neat epoxy and (b) rubber modified epoxy.

The purpose of the cure kinetic experiment is to determine the kinetic parameters (*k*, *m* and *n*) from the experimental data of α and *t*. Since equation (5-18) is in a form of differentials, the rate, *da/dt*, at a given time is required to determine the kinetic parameters. The value of rate, r_i, at time t_i was obtained by taking the derivative of polynomial fitted with the experimental data of conversion, α_i, and time, t_i. Taking the logarithm on both sides of equation (5-18) and replacing ln r, ln α, and ln (1-α) with the measured data yields a system of linear equations

$$\ln r_i = \ln k + m \ln a_i + n \ln(1 - a_i) \qquad (5\text{-}19)$$

where *i* is the index of experimental data points which runs from 1 to the number of data points measured. Solving the system of equations with a data set for a cure temperature using the least squares method would provide the values of *k*, *m* and *n* at a given temperature.

The temperatures selected in this experiment were 140°C, 170°C, and 200°C. At each temperature, the values for *k*, *m*, and *n* were determined. The best fitted values were slightly dependent on temperature. The isothermal curves with these values are presented as black solid curve in Figure 5-4. At each temperature, this calculated curve is closest to the experimental data points. However, the parameter values for one temperature did not fit the data points for the other temperature. The values determined are presented in Table 5-2.

Assuming the reaction mechanism of the curing reaction does not change in the range of temperature, *m* and *n* can be considered as invariant to the temperature and *k* is the only temperature dependent parameter. The values of *m* and *n* that were determined independently at three different temperatures were slightly different, as shown in Table 5-2. The values of *m* and *n* were varied in the range of the predetermined values until all

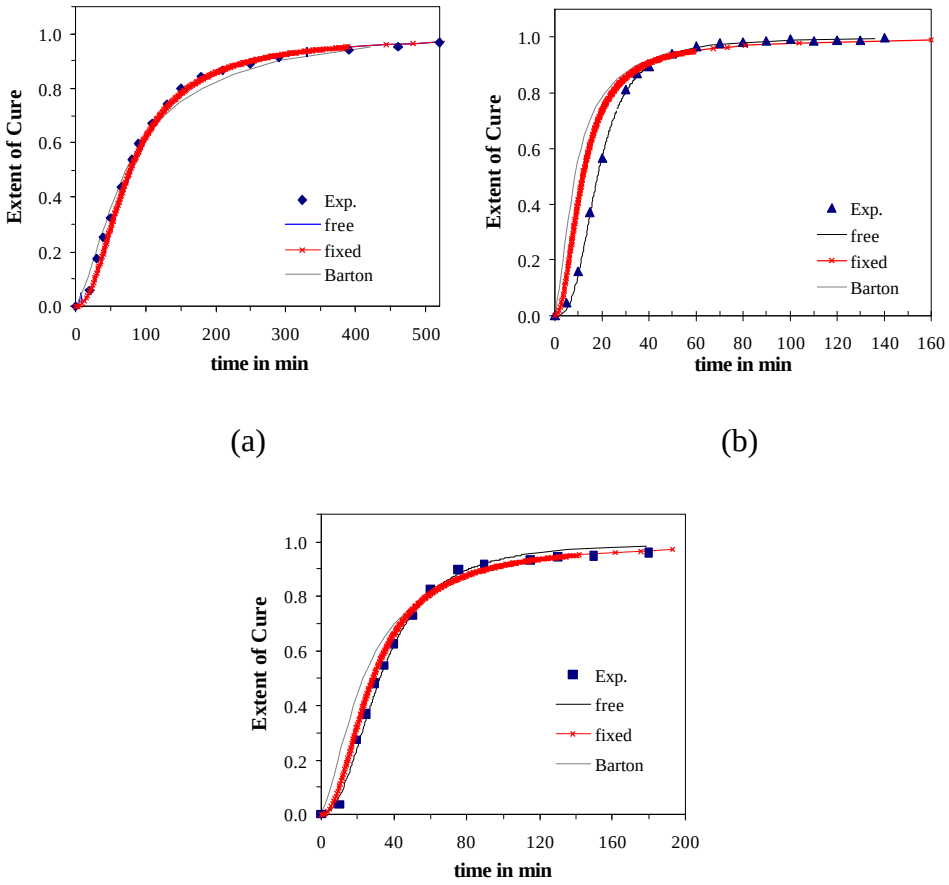

Figure 5-4. Isothermal conversion-time curves determined from various methods at (a) 140 °C, (b) 170 °C, (c) 200 °C. Dots represents experimental data, solid lines are computed from three different methods (see text).

the isothermal curves (α - t) fit the experimental data well. Fixing the reaction orders as the best values, the rate constant k at different temperatures was determined. The isothermal curve is represented by a solid curve with a cross in Figure 5-4. The best fitted values of m and n for neat and rubber modified epoxy are presented in Table 5-3 along with the activation energy, E_a and the pre-exponential factor, A.

The gray curves in Figure 5-4 determined from dynamic scan of unreacted samples with 5 different heating rates, 5 °C/min, 7 °C/min, 10 °C/min, 15 °C/min, and 20 °C/min. The analysis was performed according to the technique described by Barton[20].

The dependence of the rate constant k on the cure temperature can be analyzed in the Arrhenius expression,

Table 5-2. Kinetic parameter values determined from the best fit to equation (5-19) independently of temperature.

Cure Temperature	k (min^{-1})	m	n
140 °C	0.0287	0.545	1.632
170 °C	0.0679	0.553	1.371
200 °C	0.1654	0.662	1.417

Table 5-3. Reaction kinetic parameters for neat epoxy and the rubber modified epoxy

	m	n	A (min^{-1})	E_a (KJ/mol)
Neat Epoxy	0.54	1.64	$3.5x10^4$	47.5
Rubber Modified Epoxy	0.54	1.64	$8.3x10^4$	51.0

$$k = A\exp\left(-\frac{E_a}{RT}\right) \tag{5-20}$$

Figure 5-5 shows the plot of ln k versus 1000/T where the slope and the intercept provide the activation energy and the pre-exponential factor. Therefore, the reaction kinetics for the rubber modified epoxy system can be expressed in the following equation:

$$\frac{da}{dt} = 8.3\times10^4 \exp\left(-\frac{51.0}{RT}\right) a^{0.54}(1-a)^{1.64} \tag{5-21}$$

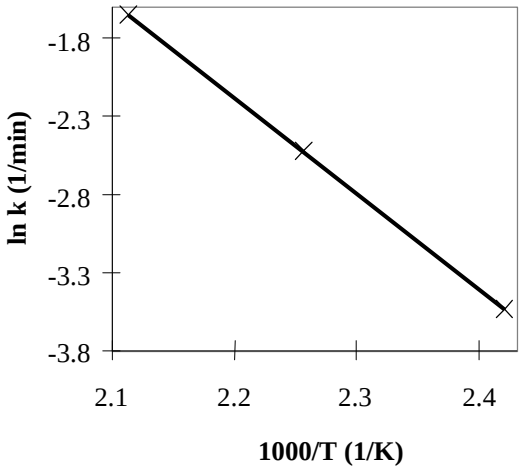

Figure 5-5. Arrhenius plot for the cure reaction of DGEBA/DDS/ETBN. ln k = -6.1392 (1000/T) + 11.326, $R^2 = 1$

5.4.1. Modeling the TTT Diagram

The glass transition was simultaneously obtained with the residual exotherm at different time. Several authors[21-23] proposed equations that describe the glass transition temperature as a function of conversion. However, some of the equations do not describe the dependence of T_g on the extent of reaction in highly crosslinked thermosetting system.

Aronhime and Gillham[22] assumed that the glass transition is a function of molecular weight before gelation. After gel point, the system can be treated as a miscible binary mixture of sol and gel fraction. Thus the glass transition temperature after the gel point is dependent on the molecular weight and the sol fraction. As reaction proceeds the molecular weight increases and thus the glass transition temperature increases. For the post gel region, the glass transition temperature increases not only because of the increase in the molecular weight but because of the depletion of sol fraction as reaction proceeds. Their concept was plausible, but their treatment was not as good as Macosko's treatment[24] which is based on the same concepts. Figure 5-6 presents the results of fitting data for the neat epoxy system to their equations. The Macosko equation thus describes our cross-linking system very appropriately.

The Macosko equation is

$$T_g = \frac{\left(\frac{1}{\frac{1}{T_{go}} - aa}\right)}{1 - \frac{bX}{1 - cX^2}} \qquad (5\text{-}22)$$

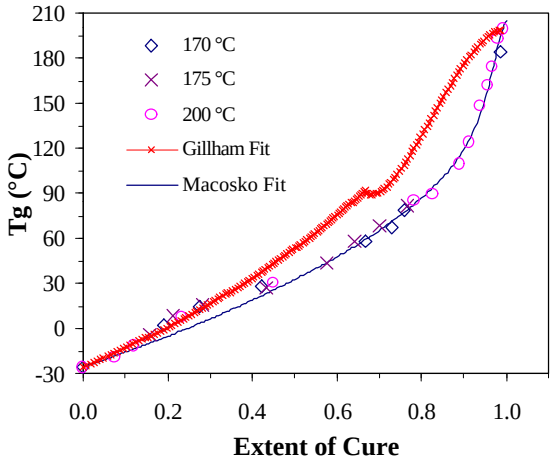

Figure 5-6. Gillham equation and Macosko equation fit to data for DGEBA/DDS.

where T_g is the glass transition temperature at the extent of conversion α, T_{go} is the glass transition temperature of the unreacted mixture, X is a measure of the cross-link density which was described in Chapter 2:

$$X = \begin{cases} 0 & \text{for } p \le p_{gel} \\ \left(\frac{3}{2} - \sqrt{\frac{1}{p^2} - \frac{3}{4}}\right)^3 \left(\frac{5}{2} + 3\sqrt{\frac{1}{p^2} - \frac{3}{4}}\right) & \text{for } p > p_{gel} \end{cases} \tag{5-23}$$

The coefficients a, b, and c can be determined from fitting our glass transition data measured as a function of conversion. With the determined values of a, b, and c, the computed glass transition temperatures were plotted as a function of conversion shown in Figure 5-7. Both plots for neat and rubber modified epoxies are consistent with most of the experimental measurements.

Equation (5-22) describes the glass transition as a function of conversion and integration of equation (5-21) describes the conversion as a function of temperature and time. Since the definition of vitrification is the time where glass transition temperature reaches the cure temperature, we can numerically solve the following equation for time to vitrification:

$$T_{cure} = T_g\left(a\left(t_{vit}, T_{cure}\right)\right) \tag{5-24}$$

Therefore the vitrification curve can be plotted in the space of log time and temperature to construct TTT diagram.

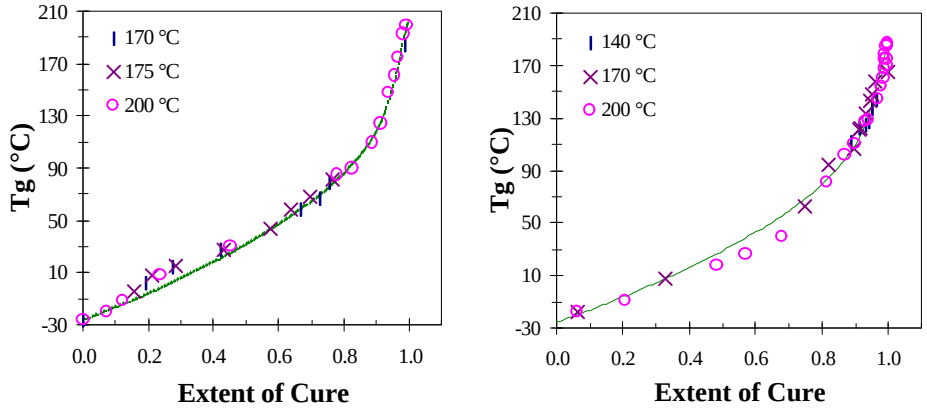

(a) (b)

Figure 5-7. Variation of glass transition as a function of conversion for (a) neat epoxy and (b) rubber modified epoxy.

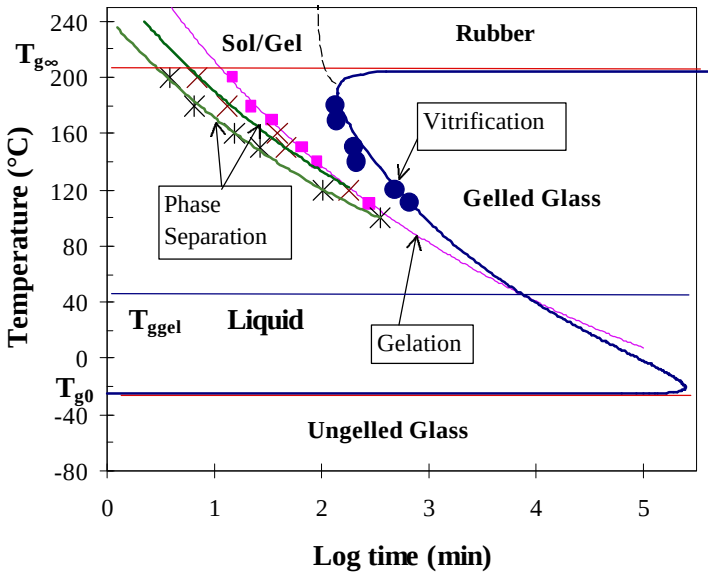

Figure 5-8. TTT diagram for DGEBA/DDS/ 10% ETBN. Points were measured using DMTA. Phase separation points were measured using light transmission device.

The calculation of the time to gelation is straightforward since the reaction kinetics is defined and the theoretical gel point is 0.577 for DGEBA/DDS system from the Flory-Stockmayer theory or Macosko branching theory. The computed vitrification curve and gelation curve is shown in Figure 5-8. Experimental measurements of gel points and vitrification points were obtained from DMTA experiments. The uncured samples were cured during the DMTA run. A typical isothermal mechanical spectrum is shown in Figure 5-9. Performing the test at multifrequency makes the identification of gel point and vitrification point apparent since the gelation is independent of frequency whereas vitrification is dependent on frequency. As shown in Figure 5-8, the theoretical curves are consistent with the experimental data. The TTT diagram also includes the cloud points measured at several isothermal temperatures using the light transmission device. The lines connecting the cloud points are shown for the sake of visual clarity.

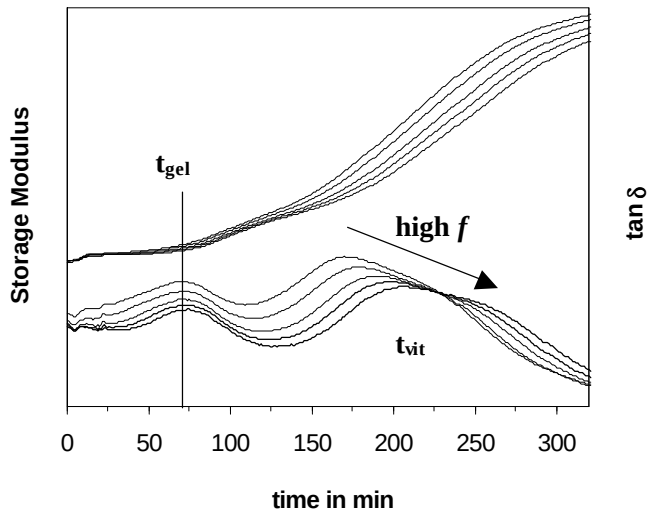

Figure 5-9. Typical DMTA spectrum of DGEBA/DDS/ETBN cured isothermally at 140 °C showing time to gelation and time of vitrification. Multiple frequency was used from 0.1 Hz to 10 Hz.

5.5. CONCLUSION

The cure reaction was analyzed based upon the autocatalytic reaction kinetic expression. When epoxy resins are cured with diamine curing agents, the hydroxyl groups produced by epoxide ring opening reaction catalyze the other ring opening reaction. Using the kinetic parameters determined from the residual heat measurements, the TTT diagrams were constructed based on the Macosko equation for vitrification and Flory-Stockmayer equation for gelation. This diagram covers a broad range of time that cannot be practically obtained from normal experiments. The gel points and vitrification points measured with DMTA verify the validity of the constructed TTT diagram.

5.6. REFERENCES

1. L. T. Manzione, J. K. Gillham, C. A. McPherson, *J. Appl. Polym. Sci.*, **26**, 889 (1981).
2. L. T. Manzione, J. K. Gillham, C. A. McPherson, *J. Appl. Polym. Sci.*, **26**, 907 (1981).
3. M. T. Aronhime, J. K. Gillham, *J. Coat. Technol.*, **62**. 35 (1984).
4. K. Horie, H. Hiura, M. Sawada, I. Mita, H. Kambe, *J. Ploym. Sci.*, A-1, **8**, 1357 (1970).
5. A. Moroni, J. Mijovic, E. M. Pearce, C. C. Foun, *J. Appl. Polym. Sci.*, **32**, 3761 (1986).
6. G. Van Assche, A. Van Hemelrijck, H. Rahier, B. Van Mele, *Thermochimica Acta*, **286**, 209 (1996).
7. L. Schechter, J. Wynstra, R. P. Kurkjy, *Ind. Eng. Chem.*, **48**,94 (1956).
8. K. Dusek, M. Ilavsky, S. Lunak, *J. Polym. Sci. Polym. Symp.*, **53**, 29 (1976).
9. K. Dusek, *Polym. Mat. Sci. Eng. Proc.*, **49**, 378 (1983).
10. C. C. Riccardi, R. J. J. Williams, *J. Appl. Polym. Sci.*, **32**, 3445 (1986).
11. S. Paz-Abuin, A. Lopez-Quintela, M. Varela, M. Pazos-Pellin, *Polymer*, **38**, 3117 (1997).
12. G. Van Assche, A. Van Hemelrijck, H. Rahier, B. Van Mele, *Thermochimica Acta*, **268**, 121 (1995).
13. J. M. Barton, *Polymer*, **21**, 603 (1980).
14. R. A. Fava, *Polymer*, **9**,137 (1968).
15. B. G. Min, Z. H. Stachurski, J. H. Hodgkin, *Polymer*, 34(23), 4908 (1993).
16. S. Y. Choy, *SPE J.*, **26**, 51 (1970).
17. R. B. Prime, "**Analytical Calorimetry**", Vol. 2, R. S. Porter, J. F. Johnson, ed., 201, Plenum Press, New York (1970).
18. S. Y. Pusatcioglu, A. L. Fricke, J. C. Hassler, *J. Appl. Polym, Sci.*, **24**, 937 (1979).
19. K. R. Kamal, S. Sourour, *Polym. Eng. Sci.*, **13**, 59 (1973).
20. J. M. Barton, *J. Macromol. Sci.-Chem.*, A8 (1), 25 (1974).

21. C. C. Riccardi, H. E. Adabbo, R. J. J. Williams, *J. Appl. Polym. Sci.*, **29**, 2481 (1984).

22. M. T. Aronhime, J. K. Gillham, *J. Coat. Tech.*, **56**, 35 (1984).

23. H. Stutz, K. H. Illers, J. Mertes, *J. Polym. Sci., Part B*: *Polym. Phys.*, **28**, 1483 (1990).

24. A. Hale, C. W. Macosko, H. E. Bair, *Macromolecules,* **24**, 2610 (1991).

Chapter 6: PREDICTION AND OBSERVATION OF MORPHOLOGY

6.1. INTRODUCTION

We have refined a model to predict morphology changes that occur during non-linear polymerization. We have also developed a technique to construct a three dimensional distribution from the measurements. There have been experimental difficulties to verify whether the system phase separates through a spinodal decomposition or a nucleation growth mechanism when homogeneous binary blends are phase separated due to the chain growth of a component. The morphology by the nucleation and growth mechanism causes to form nuclei that are growing to coalesce with other particle phases. In contrast, the spinodal decomposition mechanism leads to initially form co-continuous interwoven structure of one phase to the other and ripening process results in a structure of one particle phases dispersed in a matrix phase. Because the phase separation ends in a non-equilibrium state, both mechanisms may render the same morphological features. Inoue *et al.*[1] proposed that the CTBN rubber particles dispersed in epoxy matrix were accomplished by spinodal decomposition during the cure. On the other hand, Williams *et al.*[2] suggested that the phase separation for such system occurred through nucleation and growth mechanism. Both groups have used similar chemical systems for their experiments. In order to resolve this discrepancy, careful study is required.

In Chapter 4, the computational techniques are presented in detail for the system of DGEBA/piperidine/CTBN. The computation results are qualitatively consistent with the experimental observation and explained the phase separation behavior of the system. In Chapter 4, the reaction kinetics, viscosity and cloud points measurements are presented. In this chapter, we will present the phase behavior predicted for DGEBA/DDS/ETBN system. Also the comparison of the morphological parameters measured experimentally with those predicted by the model will be made.

6.2. THEORETICAL PREDICTION

The changes made in the prediction of morphology of the DGEBA/DDS/ETBN system are presented here. The free energy change of mixing per unit volume, DG_V^M, was expressed by equation (1) in Chapter 4 in terms of the following parameters:

1) T: Temperature
2) $\overline{V_1}$: The molar volume of the epoxy resin
3) ϕ_2: The volume fraction of the rubber component
4) z: The ratio of molar volumes of rubber to that of epoxy resin

5) χ: The Flory-Huggins interaction parameter per mole of epoxy solvent

The parameters, $\overline{V_1}$, z, and χ change with the conversion due to the chain extension[3,4]. These parameters can be related to the degree of conversion through the average molecular weight of non-linear polymers as described in Chapter 2.

6.2.1. DGEBA-DDS Non-linear Polymerization

When epoxy resin is reacted with DDS, the main reaction to form the three dimensional network is ring opening by the amine group. We assume no etherification by the hydroxyl group that is present in the epoxy resin in the cure temperatures employed. Also we assume that the reactivity of the primary amine is equal to that of the secondary amine and that intramolecular reactions do not occur. Since the epoxy monomer has two epoxide rings per molecule and DDS contains two amine group, the functionality of this system can be regarded as two for DGEBA molecule and four for DDS (A_4+B_2). Therefore, the step growth polymerization of DGEBA/DDS can be characterized by the Flory-Stockmayer statistical approach[5, 9] or Macosco approach[4] with the following parameters:

(6-1) $$p_{gel} = \frac{1}{\sqrt{g(f-1)}} = \frac{1}{\sqrt{3}}$$

where f is the functionality of DDS, and γ is the ratio of total amine groups to total epoxy groups. Then, the gel point is p = 0.577 for the system when a stoichiometric mixture (γ = 1) is polymerized. The number average molecular weight and the weight average molecular weight can be expressed as a function of conversion, p,

(6-2) $$\overline{M_N}(p) = \frac{M_A + 2M_E}{(3-4p)}$$

(6-3) $$\overline{M_W}(p) = \frac{(1+p^2)M_A^2 + 2(1+3p^2)M_E^2 + 8aM_AM_E}{(M_A + 2M_E)(1-3p^2)}$$

(6-4) $$\overline{M_N}(0) = \frac{M_A + 2M_E}{3}$$

(6-5) $$\overline{M_W}(0) = \frac{M_A^2 + 2M_E^2}{M_A + 2M_E}$$

where M_A and M_E represent the molecular weights of DDS and DGEBA, respectively.

6.2.2. Phase Separation Thermodynamics

The molar volume of DGEBA/DDS increases as polymerization progresses. Because the phase separation is quenched in the liquid state before gelation, we may assume that the density for unreacted monomers is equal to that for chains. Then the molar volume of a epoxy non-linear chain at a certain extent of conversion, *p*, may be written as:

$$\overline{V_1} = \overline{V_{1o}} \frac{\overline{M_N}(p)}{\overline{M_N}(0)} = \frac{\overline{V_{1o}}}{\left(1 - \frac{4}{3} p\right)} \tag{6-6}$$

where symbol *o* denotes the unreacted mixture of monomers (DGEBA and DDS). We can treat these two reacting species as an epoxy component. Therefore, the initial molecular weight for epoxy is $\overline{M_N}(0)$. The molar volume ratio of rubber molecule to epoxy molecule at conversion *p* is expressed as

$$z = \frac{\overline{V_2}}{\overline{V_1}} = \frac{\overline{V_2}}{\overline{V_{1o}}}\left(1 - \frac{4}{3} p\right) = z_o\left(1 - \frac{4}{3} p\right) \tag{6-7}$$

As shown in equation (2-55)in Chapter 2, the interaction parameter can be expressed as

$$c = c_o \frac{\overline{V_2}}{\overline{V_{1o}}} = \frac{c_o}{1 - \frac{4}{3} p} \tag{6-8}$$

The molar volume of the unreacted DGEBA/DDS mixture, V_{1o}, was calculated as

$$\overline{V_{1o}} = \frac{\overline{M_N}(0)}{r_E} = 286.5\, cm^3/mol \tag{6-9}$$

where the density of the DGEBA/DDS mixture, r_E, was taken to be 1.16 g/cm^3. Since the molecular weight of the rubber remains constant through the reaction, the molar volume of the rubber is computed from the number average molecular weight and the density of the rubber, 0.96 g/cm^3. Therefore, the molar volume ratio of rubber to epoxy, z_o, was set equal to 11.45 in this computation. The interaction parameter at the initial state was adopted from Williams work[6] defined as χ_o= 0.336 + 69.457/T(K).

Substitution of equations (6-6), (6-7), and (6-8) into the Flory-Huggins equation leads to the free energy of mixing per unit volume expressed as a function of the conversion

$$\Delta G_V^M = \frac{RT}{\overline{V_{1_o}}}\left[\left(1 - \frac{4}{3} p\right)(1 - f_2)\ln(1 - f_2) + \frac{f_2}{z_o}\ln f_2 + c_o f_2 (1 - f_2)\right] \tag{6-10}$$

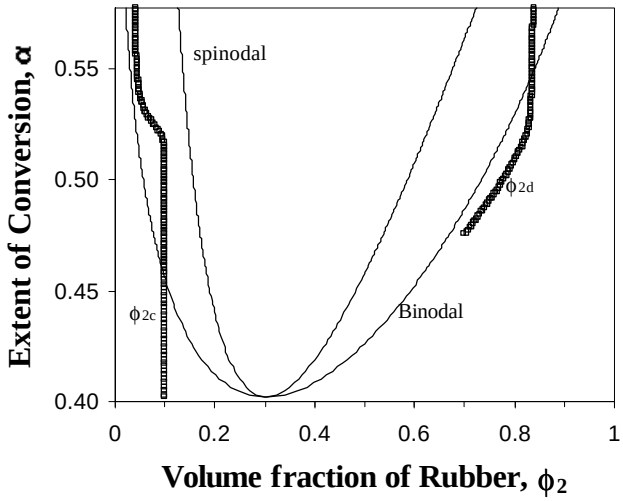

Figure 6-1. Phase diagram of degree of cure as a function of volume fraction and trajectory of rubber compositions in both phases at 220 °C. f_{2d} is the average volume fraction of rubber in rubber phase.

where the subscript *o* denotes the unreacted mixture of monomers. The only parameters that vary during an isothermal reaction are the volume fraction of rubber, ϕ_2, and the extent of conversion, *p*.

Equation (6-10) describes the stability of the solution as a function of conversion at a certain temperature and defines the equilibrium compositions and spinodal compositions. Figure 6-1 shows the equilibrium and spinodal curves as a function of conversion at cure temperature of 220 °C. As the epoxy monomers polymerize, the free energy of mixing increases due to the decrease in the absolute value of the entropic contribution. At the binodal conversion of 0.455 (= p_{cl}), the solution is supersaturated when 10 vol % of ETBN is initially mixed and cured at 220 °C.

6.2.3. Kinetics of Phase Separation

Further reaction above conversion *p* will force the system into the metastable region. In order to make a finite size of a new dispersed phase from the metastable solution, the surface free energy of the dispersed phase in the matrix phase should be less than or equal to the free energy change for the formation of a new phase. The free energy change for the formation can be computed from the plot of equation (6-10) as a function of the rubber composition, ϕ_2 at a certain conversion, *p*. There is a maximum value (ΔG_c) for the free energy change for forming a new spherical phase with a critical size of r_c. The particles with a radius less than r_c are re-dissolved into the matrix phase, and the particles greater in size than r_c can grow further. Therefore, the nucleation rate can be expressed as

the product of the rate of composition fluctuations and Boltzmann factor with energy barrier of ΔG_c.

$$\frac{dN}{dt} = F_0 D \exp\left(-\frac{\Delta G_c + E_F}{RT}\right) \quad (6\text{-}11)$$

where F_0 is a proportionality constant, D is the diffusion coefficient of rubber in the epoxy, and E_F is the energy barrier for the composition fluctuation.

The growth of nuclei born at a certain degree of cure, $p > p_{cl}$, depends on the viscosity of the old dispersed particles (old generation nuclei) as well as the number of particles and the departure from equilibrium of rubber in the continuous phase, $\left(f_{2c} - f_2^a\right)$. We will denote the departure from equilibrium as DE. The growth rate, which is defined as the increase in volume fraction per unit time, is proportional to the interfacial area per unit volume and the driving force $\left(f_{2c} - f_2^a\right)$. That is,

$$\frac{dV}{dt} = 4\pi r^2 k_f N_V \left(f_{2c} - f_2^a\right) = 4\pi r^2 N_V \frac{dr}{dt} \quad (6\text{-}12)$$

where N_V is the number of particles per unit volume, and k_f is a mass transfer coefficient. Since the mass transfer coefficient for a sphere in a stagnant medium[7] is given by $k_f = \frac{D}{r}$, the growth rate of radius can be written as:

$$\frac{dr}{dt} = \frac{D}{r}\left(f_{2c} - f_2^a\right) \quad (6\text{-}13)$$

The diffusion coefficient can be related to the viscosity of the epoxy matrix using the Stokes-Einstein equation, $D = \frac{D_0 T}{\eta}$. The viscosity of the epoxy matrix increases as polymerization proceeds at a constant cure temperature due to the increase in molecular weight. Viscosity also decreases with temperature. Both the molecular weight and the temperature effect on the viscosity are usually expressed with the following equation:

$$\eta(T, p) = \eta_o \left(\frac{\overline{M_w}(p)}{\overline{M_w}(0)}\right)^{3.4} \exp\left[\frac{E_\eta}{RT}\right] \quad (6\text{-}14)$$

The viscosity was measured in the temperature range of 25 °C to 70 °C as soon as DGEBA was mixed with DDS so that the molecular weight effect could be neglected. Arrhenius analysis yields η_o =7.60 x 10^{-7} Pa s and E_η = 33.6 KJ/mol. The value of E_η was consistent with literature values for similar systems[8,9]. Because the molecular weight changes during polymerization, molecular weight can be expressed in terms of conversion as in equation (6-2). Equation (6-14) can also be written in terms of conversion.

The DGEBA/DDS mixture would show a viscosity close to that of room temperature water in order of magnitude at around 260 °C if it did not react. The viscosity of the unreacted mixture at such a high temperature can be estimated from equation (6-14) using the values of activation energy for the viscosity and the pre-exponential factor. Since the diffusion coefficient of water at room temperature is on the order of 10^{-9} m^2/s, that of the DGEBA/DDS mixture may be estimated as 10^{-9} m^2/s at 260 °C and thus the value for D_o was estimated $1.5x10^{-15}$ N/K using the Stokes-Einstein relationship. The surface tension of rubber on epoxy was assumed to be independent of the conversion and temperature and was set to 0.8 mJ/m^2. These values are close to those roughly estimated from other researchers[10-12].

The cross linking polymerization for the rubber modified epoxy system was analyzed with the experimental data measured from DSC residual exotherm techniques based on the autocatalytic reaction kinetics

$$\frac{dp}{dt} = A\exp\left(-\frac{E_a}{RT}\right)p^m(1-p)^n \qquad (6\text{-}15)$$

The reaction kinetic parameters, A, E_a, m, and n, were obtained by fitting the DSC data to equation (6-15)

1) the pre-exponential factor, $A = 8.3x10^4$ min^{-1}
2) the reaction activation energy, E_a = 51 KJ/mol
3) the reaction order for the autocatalytic term, m = 0.54
4) the reaction order for consumption of reacting species, n = 1.64

Substitution of equations (6-14) and (6-15) into the nucleation rate and growth rate expressions in equations (6-11) and (6-13) leads to the nucleation rate and the growth rate rewritten in terms of conversion

$$\frac{dN}{dp} = \frac{F_o D_o T}{Ah_o}\left(\frac{\overline{M_w}(p)}{\overline{M_w}(0)}\right)^{-3.4} p^{-m}(1-p)^{-n}\exp\left[\frac{E_a - E_h - E_F - \Delta G_c}{RT}\right] \qquad (6\text{-}16)$$

$$r\frac{dr}{dp} = \frac{D_o T}{Ah_o}\exp\left[\frac{E_a - E_h}{RT}\right]\left(\frac{\overline{M_w}(p)}{\overline{M_w}(0)}\right)^{-3.4} p^{-m}(1-p)^{-n}\left(f_{2c} - f_2^a\right) \qquad (6\text{-}17)$$

where f_2^a is the equilibrium rubber composition of the epoxy rich phase and f_{2c} is the actual rubber composition of the epoxy rich phase. For isothermal cure, F_o, D_o, h_o, A, D_o, E_a, E_h, and T are independent of conversion p. Other parameters, E_F, ΔG_c, and f_{2c}, are dependent on conversion p and f_{2c}. These values can be determined from the thermodynamics, *i.e.* free energy of mixing curve, if f_{2c} is determined at a given p.

Since f_{2c} is equal to f_{2o} at the binodal point, the rubber composition in the dispersed phase, f_{2N}, can be determined from the free energy of mixing curve (equation (6-10)). Solving equations (6-16) and (6-17) simultaneously yields the number and size of particles at binodal conversion p_{cl}, where the number of nuclei is is zero but its size is infinite. This implies that the system is supersaturated at p_{cl} and no phase separation occurs. Because the reaction continues to proceed and the equilibrium composition is shifting toward a composition lower than the previous equilibrium composition, therefore the homogeneous solution with $f_{2c} = f_{2o}$ now falls in the meta-stable region.

At this conversion, since the free energy curve is defined and the composition of the continuous phase f_{2c} is known, the thermodynamic parameters, E_F, ΔG_c, f_2^a, and f_{2N}, can be determined from the free energy of mixing curve (equation (6-10)). Again from equations (6-16) and (6-17), the number and size of nuclei is determined. Since the initial composition is known and the rubber composition, size and number of newly formed phase is computed at this conversion, the new composition of epoxy phase can be determined from the mass conservation law. Therefore repeating the above procedures until the conversion reaches the gel point provides the trajectory of rubber composition in both phases, along with the number density of rubber particles and the growth of nuclei.

By increasing conversion by small increments from p_{cl}, one can numerically solve the differential equations (6-16) and (6-17) for the number density and the radius of the dispersed particles using the Euler method. Once the number density and the radius of the dispersed particles are determined, the actual composition f_{2c} in the continuous phase at the given conversion can be computed from the mass conservation law.

6.3. MORPHOLOGY MEASUREMENTS

6.3.1. Formulation and Cure Cycle

The formulation was adjusted to provide 10 wt % rubber (ETBN) in the whole system (DGEBA-DDS-KELPOXY) and to keep a stoichiometric proportion of DDS with respect to the sum of epoxides coming from DER-331 and KELPOXY. Since KELPOXY is a mixture of DGEBA of 60wt % and ETBN of 40 wt %, making 10 wt % of ETBN in DGEBA-DDS requires mixing 25 wt % of KELPOXY in the solution. The formula for making W_T grams of sample is

$$W_A = \frac{rM_A}{M_{KEL}}\left(\frac{(1-2.5w_R)M_{KEL} + 2.5w_R M_E}{M_E + rM_A}\right)W_T$$

$$W_{KEL} = 2.5w_R W_T$$

$$W_E = W_T - W_A - W_{KEL}$$

WHERE

W_T: total weight of sample

w_R: weight fraction of ETBN in total sample; 10 wt %

Table 6-1. Epoxy formulations used in this investigation

System ID	DER-331 (g)	DDS (g)	KELPOXY (g)
R-or SESxxx	52.88	22.12	25.00
RENxxx*	56.67	18.33	25.00

* REN-xxx : DDS/EPOXY ratio was 0.8 in weight, the other two systems were mixed in stoichiometric ratio.

r: mole ratio of DDS to DGEBA; 2 for stoichiometric mixture

W_A: weight of amine (DDS) M_A: Molecular weight of amine (DDS)

W_E: weight of epoxy (DGEBA) M_E: Molecular weight of epoxy

W_{KEL}: weight of KELPOXY M_{KEL}: Molecular weight of KELPOXY

The epoxy formulations are given in Table 6-1. A bulk mixture of KELPOXY and DER-331 was made by mechanical stirring in an oil bath at 90 °C with a nitrogen purge. A homogeneous solution was achieved in about 5 min and degassed to remove trapped air. DDS was added into the mixture and mechanically stirred at 130°C under vacuum until DDS dissolved completely. For the fracture test specimens, it took about 30 min to get a visibly clear solution of about 30g. The solution was poured into a preheated silicone rubber mold at 130 °C and degassed in a vacuum oven at this temperature at 29 in Hg until no air bubbles escaped. The fractured samples were microtomed for SEM analysis. In later sections, it will be demonstrated that the sample preparation time may affect the final morphologies.

As soon as mixing and degassing were completed, samples were cured in a regulated convection oven at various temperatures until they passed the gel point and were post-cured at 220 °C for 1 hr to get the maximum conversion of the epoxy-diamine matrix. The time to gelation at a certain temperature was determined from the kinetic experiments and confirmed by DMA experiments.

6.3.2. SEM

The specimens were microtomed under cryogenic condition. The microtomed surface roughness was at maximum 0.05 μm. The microtomed specimens were stained with OsO_4 for 6 hours and then sputter coated with gold to enhance the contrast between the rubber particle phase and the matrix phase. The surfaces of the specimens were examined in the scanning electron microscope (SEM). Although transmission electron microscopy (TEM) of thin films of specimens provides clearer micrographs than the SEM micrographs of the surfaces, SEM was selected to take two dimensional pictures of the specimen for the following two reasons. Microtomed thin films show more distorted particles due to the shearing force of the microtoming knife than SEM specimens. The other reason is that magnification of SEM is more suitable for a micrograph to include

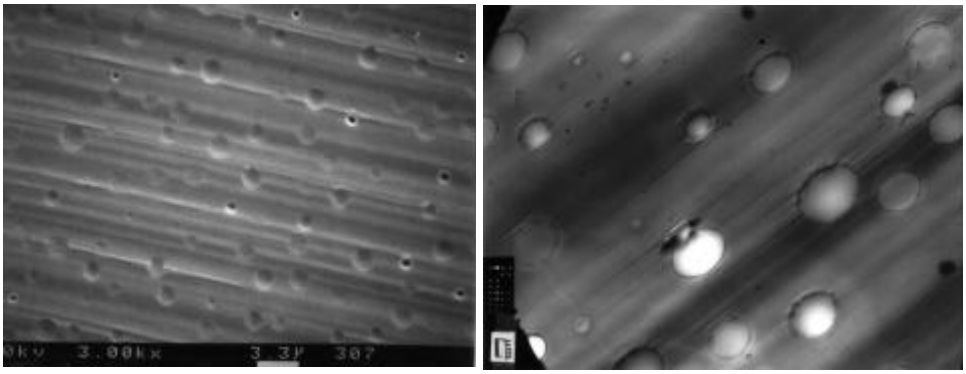

(a) cure at 200 °C (b) Cure at 100 °C

Figure 6-2. (a) SEM micrograph of a surface and (b) TEM micrograph of a microtomed thin film for cured DGEBA/DDS/10 % ETBN.

many large particles than that of TEM. Typical SEM and TEM micrographs are shown in Figure 6-2.

The two-dimensional particle size distributions were obtained by measuring 500-700 particles using the image analyzer and converted to the three-dimensional particle size distributions using the method described in chapter 3. The number, the area, and the volume average radii, $\overline{R_N}$, $\overline{R_A}$, and $\overline{R_V}$, respectively, were calculated from the 3-D distribution:

$$\overline{R_N} = \frac{\sum_{i=1}^{m} N_V(i) R_i}{\sum_{i=1}^{m} N_V(i)}, \quad \overline{R_A} = \left(\frac{\sum_{i=1}^{m} N_V(i) R_i^2}{\sum_{i=1}^{m} N_V(i)} \right)^{\frac{1}{2}}, \text{ and } \overline{R_V} = \left(\frac{\sum_{i=1}^{m} N_V(i) R_i^3}{\sum_{i=1}^{m} N_V(i)} \right)^{\frac{1}{3}} \tag{6-18}$$

where $N_V(i)$ is the number of particles with radius of R_i in a unit volume of the material. The volume fraction V_f is defined as the total volume of spheres that is contained in the unit volume of the material so that

$$V_f = \frac{4\pi}{3} \sum_{i=1}^{m} N_V(i) R_i^3 \tag{6-19}$$

The surface density S_V expresses the ratio of total surface area of spheres to the volume of the material. Therefore,

$$S_V = 4\pi \sum_{i=1}^{m} N_V(i) R_i^2 \tag{6-20}$$

Another useful description of structure is the mean free distance λ between particles. This gives the average surface-to-surface distance between each particle and all of its

neighbors. This mean free distance is directly related to the volume-to-surface ratio of the matrix in which the particles are embedded[13]:

$$\lambda = 4\frac{1-V_f}{S_V} \qquad (6\text{-}21)$$

The volume fraction of rubber particles can be estimated from the number per unit volume and radii of particles which can be converted by statistical treatment of the number per unit area and radii of circles which appeared on the micrographs[13-15]. Construction of a precise distribution of three-dimensional particle size requires that a sufficient number of same size circles on the micrographs be measured. The distance between two consecutive microtomed sections should be large enough not to cut the same particles two or more times. Otherwise, the two-dimensional distribution may over-count the number of circles in a group. Furthermore, the size of the small circles should be large enough so that a sufficient number of pixels in an image analyzer represent them. Also, the number of large circles should be numerous enough on a micrograph to reduce cost and time.

6.4. RESULTS

6.4.1. Comparison of Prediction and Observation

The RES130 and RES200 samples were prepared with much caution. The mixing and degassing time of DGEBA/ETBN with DDS was greatly reduced using small samples. The time of this process was about 10 min at 130 °C which corresponds to the extent of

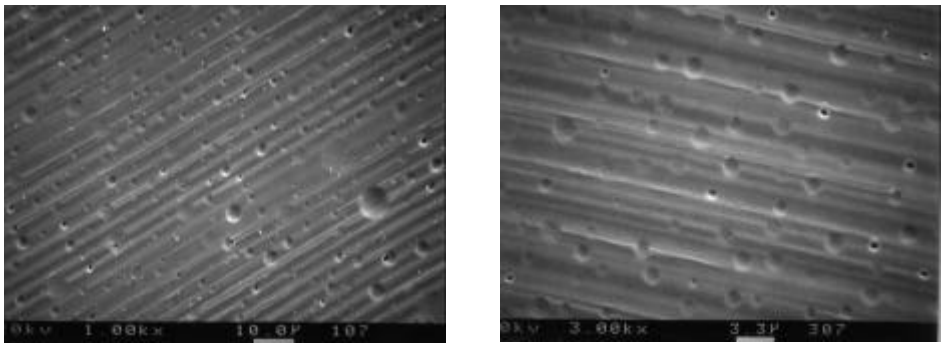

(a) Cured 130 °C (b) Cured 200°C

Figure 6-3. SEM micrographs of RES130 (a) and RES200 (b). Rapid transfer to predetermined cure temperatures.

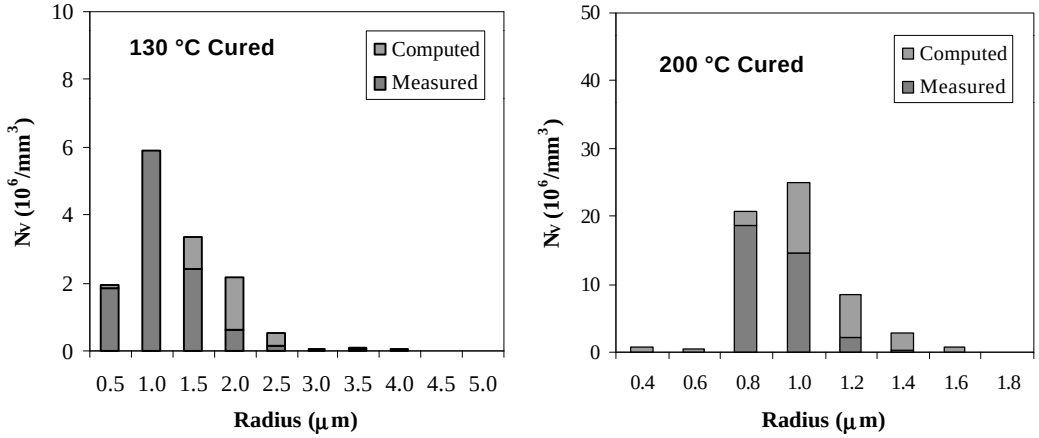

Figure 6-4. Comparison of computed particle size distributions with expermentally measured ones for RES130 and RES200 samples.

conversion of 0.002. As soon as the sample preparation was finished, the samples were rapidly transferred to an oven preheated at the cure temperature. Thus the time of preparation did not affect the phase separation process. Typical SEM micrographs are shown in Figure 6-3.

The radius and the number of particles in many micrographs were counted to construct the two dimensional distributions of circular particle size. These 2-D size distributions were converted to 3-D particle size distribution using the technique described in Chapter 3. These 3-D distributions are compared to the distribution predicted by the phase separation model. Since the group size of the particle size distribution is dependent on the number of particles measured and the magnification of micrographs, it is varied for different cure samples. It is not practically feasible to obtain a particle size distribution (histogram) with a small group size where a smooth distribution curve appears. On the other hand, it is feasible to manipulate the model computation of the small size group. Therefore, the dense and smooth distribution computed was regrouped as histograms in Figure 6-4.

The value for the parameter, F_o, was adjusted until the predicted particle size distribution was close to the measured particle size distribution for sample RES200 cured at 200°C. The selected value at the temperature was fixed to predict the morphology developed at the other cure temperatures. Figure 6-4 shows consistency between computed and measured histograms for the samples cured at two different temperatures (130°C and 200°C).

6.4.2. Importance of Sample Preparation

In contrast to the rapid transferred samples, slow transferred samples were mixed at 130 °C for about 30 min and degassed for about an hour or so until all the air bubbles

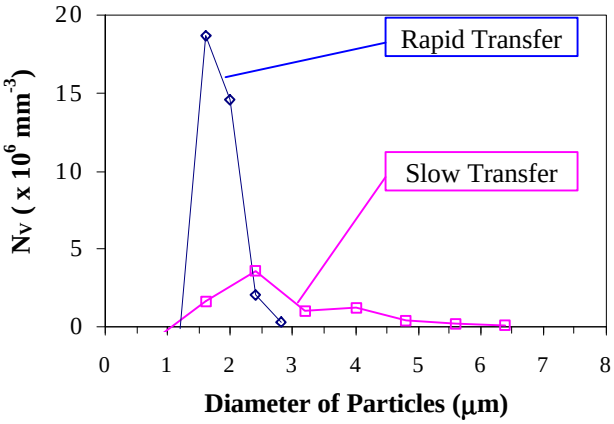

Figure 6-5. Two different particle size distributions induced by different sample preparations even when cured at the same temperature, 200 °C/

were removed before the samples were placed in an oven at the predetermined temperatures. The time of sample preparation cannot be ignored for these "slow transfer" samples since 90 min at 130 °C corresponds to the extent of conversion close to the point where phase separation occurs. The "slow transfer" sample shows broader distribution with a larger diameter than the "rapid transfer" sample cured even at the same cure temperature of 200 °C as shown in Figure 6-5. Other morphological parameters are also quite different and it is presented in Table 6-2. Since the samples for SES130 and RES130 were prepared at the same temperature as the cure temperature, 130 °C, they show the same values for the morphological parameters in Table 6-2.

6.4.3. Influence of Temperature on Morphology

In Figure 6-1, the trajectory of actual rubber compositions in both continuous and dispersed phases is shown as the reaction progresses at the cure temperature of 220°C. The extent to which the equilibrium composition is approached by the composition of the reaction is slow in comparison to phase separation, the composition of each phase will evolve through the path close to the binodal curve, as illustrated by the ϕ_{2c} curve at late

Table 6-2. Morphological parameters for slow and rapid transferred samples

Transfer	Temp (°C)	R_N (μm)	R_V (μm)	V_f	S_V (μm)	λ (μm)	$N_V(10^6$ $mm^{-3})$
Slow/Rapid	130	1.15	1.47	0.15	0.23	15.03	11.07
Slow	160	1.72	2.01	0.14	0.18	19.77	4.00
Slow	200	1.51	1.65	0.14	0.23	14.95	7.00
Rapid	200	0.91	0.93	0.12	0.38	9.34	35.57

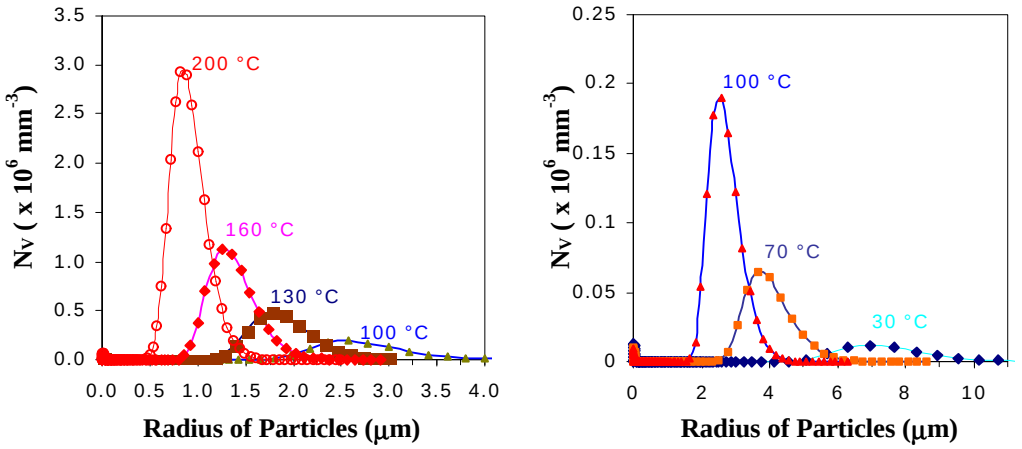

(a) High Temperature Range (b) Low Temperature Range

Figure 6-6. Effect of cure temperature on particle size distributions

continuous phase depends on the ratio of the rates of both phase separation and polymerization. This is because the cure reaction establishes a new equilibrium composition while the system moves toward the old equilibrium composition. If the cure conversion in Figure 6-1. If the cure reaction is fast relative to the phase separation, there will be insufficient time for the rubber composition to follow the binodal curve. This is illustrated by the ϕ_{2c} curve at early conversion in Figure 6-1.

The effect of cure temperature on the particle size distribution is depicted in Figure 6-6. The cure temperature range was selected from 30°C to 200°C, in which experimental observation is possible without degrading the sample. The distribution becomes sharper and unimodal with the increase in the cure temperature within the range of inspection as it displays part of the behaviors shown in the system of DGEBA/piperidine/CTBN discussed in Chapter 4 (see Figure 4-6 in Chapter 4). The number average radius decreases, while the number density increases with an increase in the cure temperature.

Since low cure temperatures emphasize the frequency of small particles, the number average radius is affected by the small particles more than the volume average radius. As the temperature increases, the distribution peak for small particles disappears while the distribution peak for large particles shifts to low radius. However, this kind effect does not occur in DGEBA/DDS/ETBN as significantly as DGEBA/piperidine/ CTBN exhibited. Consequently, the temperature range (100°C – 220°C) practically employed for DGEBA/DDS/ETBN system leads to the opposite behaviors of morphology to DGEBA/piperidine/CTBN system within the temperature range (90°C – 150°C).

The equilibrium and spinodal curves shift to higher conversion as the cure temperature increases as depicted in Figure 6-7. Therefore, the phase separation of the rubber at high cure temperatures begins later than at low cure temperatures. If phase

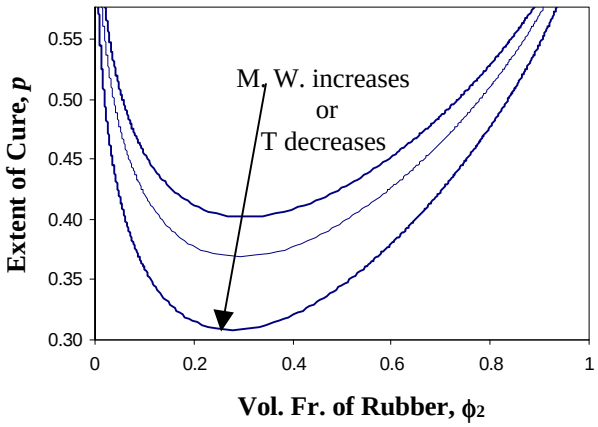

Figure 6-7. Influence of molecular weight of rubber or temperature on the equilibrium curve. Spinodal curves were omitted for visual clarity.

separation arrests at the gel point, then the potential "window" of phase separation will always be larger at low cure temperature. However, the size of this window does not always decide the overall particle size and population.

Since ΔG_N is zero at the incipient point of phase separation (conversion at binodal), p_{cl}, the critical size of nuclei approaches infinity, but the number of nuclei formed with this size is equal to zero. Further progress of the reaction from the p_{cl} increases DG_N from zero, although the magnitude of this depends on how far the rubber composition in the continuous phase, ϕ_{2c}, is located from the equilibrium composition, ϕ_2^{α}. Because DG_N increases with an increase in the level of non equilibrium state, $(\phi_{2c} - \phi_2^{\alpha})$, the nuclei size usually decreases while the number of nuclei generated increases as conversion increases if the viscosity does not change with conversion.

If the viscosity of the matrix is sufficiently high to keep the continuous phase composition close to the initial composition of rubber, the departure from equilibrium state becomes larger as reaction progresses because the equilibrium composition of the continuous phase is changing to a lower composition. Thus, DG_N increases with conversion. Consequently, smaller but more numerous particles are generated as the reaction progresses and this process is quenched at the gel point. Consequently, the lower temperature cure generates larger and more numerous particles than high temperature cure simply because the lower temperature cure has a larger "window" of phase separation than a high temperature of cure. This is the case depicted in Figure 5 (b) in Chapter 3.

If the viscosity is sufficiently low to change the composition of the parent phase to the equilibrium composition faster than the polymerization reaction, then larger but smaller numbers of nuclei will be generated than in the earlier conversion. This is because the new composition of the continuous phase is closer to the equilibrium composition than the old composition of the continuous phase and thus less value of ΔG_N for new nuclei results

than that for the old nuclei. This will happen at early conversion when the activation energy for the viscosity is lower than that for the reaction. A lower activation energy for viscosity means that viscosity changes are more sensitive to temperature changes than polymerization. Therefore, a temperature increase leads to a composition of the continuous phase further away from the equilibrium composition and thus ΔG_N increases. Consequently, even if a higher cure temperature will phase separate at a later conversion than a low cure temperature, more numerous but smaller particles will be generated at high cure temperature than at a low cure temperature. Since the system of DGEBA/DDS/ETBN has lower activation energy for viscosity than that of the reaction, it indicates that particle size decreases and the number of particles increases with increasing temperature of cure. The behavior is shown in Figure 6-6.

Figure 4-5 (a) and Figure 6-6 indicate that the frequency for a small particle size group is pronounced relatively to a large particle size group with the decrease in the cure temperature. However, Figure 6-6 does not show as significantly such effect as Figure 4-5 (a) in chapter 4. These small particles were born in a late stage of conversion. Because the phase separation rate is faster than polymerization rate at low cure temperature, the composition of the parent phase, ϕ_{2c}, quickly approaches the equilibrium composition and then traces the equilibrium curve until the viscosity builds up enough to keep its composition far away from the new equilibrium composition. At this conversion, phase separation resumes and the nuclei generated have less time to grow than the nuclei generated in early conversion. Consequently, a bimodal distribution results. As temperature increases, the peak for the small particle size group disappears. This can be seen clearly in Figure 4-5 (a) in Chapter 4.

In the system of DGEBA/DDS/ETBN, the possibility of having a bimodal distribution may be ignored. The reason for this is that the peak for the small particle size group in the particle size distribution is negligibly small except for the one for 30 °C, which is not a normal temperature used for curing this system. Consequently, the low cure temperature has generated different sizes of nuclei in a broader range of conversion than the high cure temperature. Therefore, a broad particle size distribution is achieved at low cure temperatures. The number of particles increases to a maximum and then decreases with increasing cure temperature.

6.4.4. Morphological parameters

The effect of cure temperature on the final morphology is shown Figure 6-8. The volume average radius decreases as cure temperature increases. The number average radius, however, shows a maximum value because of the presence of the bimodal distribution at low cure temperatures. As explained in the previous section, the number of particles per unit volume increases with the increase in the cure temperature within the range of observation. The volume fraction of particles is almost insensitive and slightly decreases with temperature.

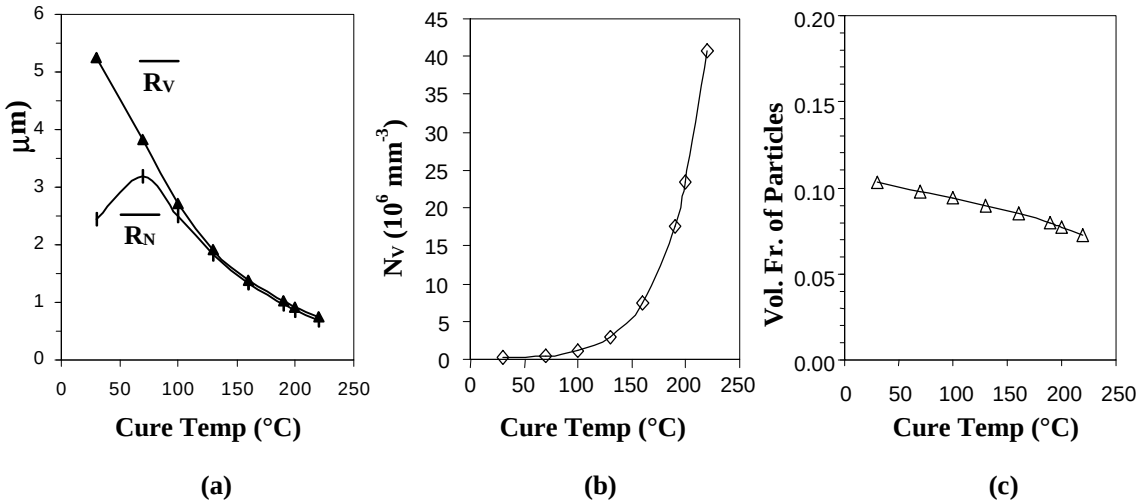

Figure 6-8. Effect of cure temperature on average particle size, volume fraction and number of dispersed rubber particles.

6.4.5. Spinodal or Nucleation Growth?

Spinodal decomposition requires a system to have the initial rubber composition close to the critical composition so that the initial rubber composition enters directly in the unstable region without changing its composition. Also, the rate of cure should be considerably high to increase the possibility for the system to land in the unstable region. The last requirement for the spinodal decomposition is that the cure temperature must be low to shift the spinodal and equilibrium curves down to lower conversion and to move them to a lower rubber composition. Because the initial rubber composition should be relatively low (5-20 %) for the toughening epoxy thermoset, phase separation is usually considered to occur through the binodal decomposition. If a much high molecular weight of toughener compared to the initial molecular weight of thermoset resin is incorporated, the phase diagram is skewed to lower composition. This situation is shown in Figure 6-7. A high molecular weight toughener may create a phase-inverted morphology or co-continuous morphology by spinodal decomposition.

When phase separation takes places in the unstable region, it is believed that a co-continuous morphology results at the early stage as shown in Figure 6-9[16]. Inoue has studied the phase separation process for epoxy resin modified with commercial polyethersulfone (ICI Victrex 4100G)[17] and liquid rubbers (CTBN and ATBN)[18], utilizing light scattering, scattering electron microscopy, and torsional braid analysis. Curing at high temperature with composition of rubber varying from 11 %wt to 23 %wt exhibited resulting morphologies that a bimodal distribution of spherical domains was dispersed in the matrix. Low temperature cures with 23 %wt of rubber produced a co-continuous binary phase structure (interconnected globule structure). However, the micrograph was taken from a fracture surface using a scanning electron microscopy that would distort the

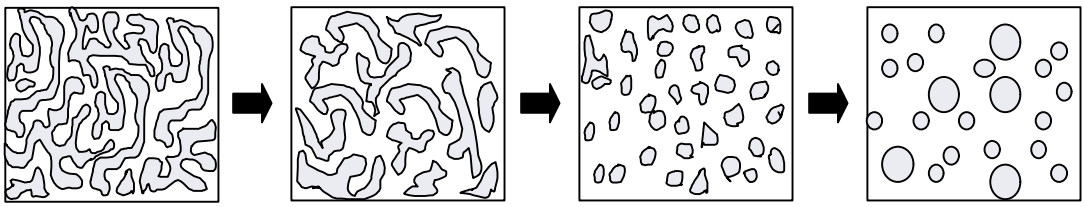

(a) (b) (c) (d)

Figure 6-9. Schematic representation of evolution of co-continuous structure as a function of conversion of cure.

image of the structure. Inoue postulated that the coarsening process of the co-continuous structure generated at early stage of spinodal decomposition yielded the dispersed spherical domains in a matrix (Figure 6-9). He also suggested from studies using polyethersulfone that a phase inverted morphology could be produced via a connected globule structure which had formed from the spinodal decomposition mechanism. Even if his schematic representation of phase separation is possible with some uncertainty about the transition from Figure 6-9 (c) to (d), the possibility of spinodal decomposition is dependent on molecular weight of toughener relative to epoxy, initial composition of rubber, and temperature of cure. The following section continues this discussion.

6.4.6. Anomalous Morphologies

In the framework of modeling, it has been assumed that the dispersed particle phases generated at a certain conversion grow mixing homogeneously with newly

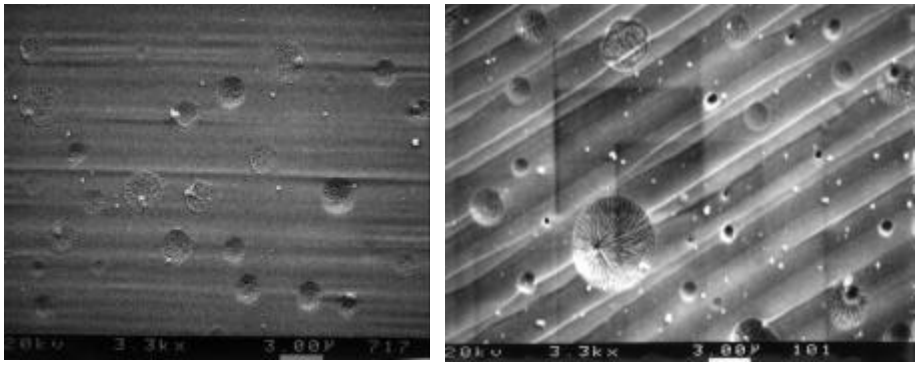

(a) REN110 (b) SES130

Figure 6-10. Spinodal decomposition in dispersed particle phases generated by nucleation and growth mechanism. (a) Sample REN110 were cured at 110 °C and (b) SES130 was cured at 130 °C

generated composition. However, as shown in Figure 6-1, the average composition of the dispersed particles falls in meta-stable region or it may be even in unstable state. Some of the dispersed particles may have actual composition in the meta-stable or unstable regions. Those particles should perform another phase separation process due to their instability if the viscosity is low enough to facilitate it. We have observed the phase separation inside a phase. Co-continuous structure in several dispersed spherical phases was obtained when the DGEBA/DDS/ETBN was cured below 130 °C. This kind of feature did not appear in all of the dispersed particles but it can be reproduced and found in other samples.

When a polymer of high molecular weight is used as a toughener for a thermoset, the phase diagram is skewed toward the low composition of polymer and the critical conversion occurs at a lower conversion than a small molecular weight toughener. Figure 6-11 represents the phase diagram which was computed with molecular weight of 15,000 g/mol. The critical point is located at 0.12. The left binodal region appears to be much narrower than that for the low molecular weight rubber whereas the other binodal region is much wider. Therefore, even when 10 vol % of the toughener is added to a thermoset resin, the system can readily fall into the unstable region.

Let us assume that a polymer with 15k of molecular weight is initially mixed with the epoxy resin to make a homogeneous solution **A**. As the reaction proceeds, phase separation occurs through spinodal decomposition to form a co-continuous structure composed of an epoxy rich phase **A'** and a polymer rich phase **B**. The spinodal decomposition is a fast process, and we may assume the composition of each phase is located on the points **A'** and **B** shown in phase diagram of Figure 6-9. The volume of epoxy rich phase **A'** will have BO/A'O times than the volume of polymer rich phase **B**. Since BO is greater than A'O, the matrix phase is epoxy rich phase **A'** (white area in the structure I) and the minor phase is polymer rich phase B (dark area in structure I). These two compositions are in a stable state at p_1. If there is no further reaction, the system will keep the compositions of both phases as **A'** and **B** and the worm-like structure will coarsen to make a fairly regular structure which minimizes the surface free energy.

However, if reaction proceeds, epoxy rich phase **A'** and polymer rich phase **B** fall in metastable state or unstable state depending on the rate of polymerization. Let us consider a case that both phases **A'** and **B** are phase separated in the metastable region. In Figure 6-11, it is demonstrated that phase **A'** separates further at higher conversion than phase **B** does. It was drawn for visual clarity, but it is not necessary that phase separation take place simultaneously and at the same conversion in both phases.

First, consider phase separation in phase **B**. If the separation occurs at p_2 and a new phase has the equilibrium compositions, the spherical particles will be generated in phase **B** which becomes phase **B'** with a new composition corresponding to point B'. The spherical phase **A"** has a composition corresponding to **A"**. The volume of all spherical particles in phase **B'** (white particles in the dark area in structure II) will be $B'O_2/A"O_2$ times of the volume of phase **B'**.

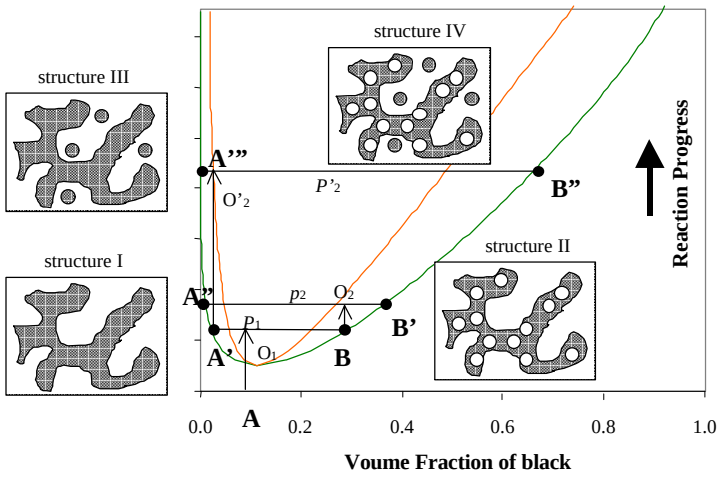

Figure 6-11. Schematic representation of phase separation in both co-continuous phases.

Now consider the phase separation in phase **A'** that occurs at p'_2. Since phase **A'** is in metastable state at p'_2, nucleation and growth controls the phase separation process and new phases will be spherical particles with a polymer rich composition (dark particles in white area in structure III). After phase separation, the epoxy rich phase will have a composition of **A'"** and the polymer rich spherical phase will have a composition of **B"**. The volume of phase **A'"** will have $B"O'_2/A'"O'_2$ times of the volume of phase **B"**.

Comparing the magnitude of $A'"O'_2/B"O'_2$ to $B'O_2/A"O_2$, it can be readily seen that the polymer rich particles in epoxy rich phase, dark particles in white area, should be less populated than the epoxy rich particles in polymer rich phase, white area in dark area is. Consequently, the final morphology of this type of phase separation results in structure IV shown in Figure 6-11. Morphologies like structure IV often appears in thermoplastic toughened thermoset materials. An example is presented in Figure 6-12.

6.5. CONCLUSIONS

A model that can describe the phase separation process during polymerization reaction has been employed to analyze the morphology development for DGEBA/DDS/ETBN system. The morphological changes of this reaction system as a function of conversion were analyzed on the basis of thermodynamics of a binary mixture combined with nucleation and growth rates. The predicted morphologies showed good agreement with the experimental measurements. Influence of cure temperature and molecular weight of the toughener on the final morphology was investigated.

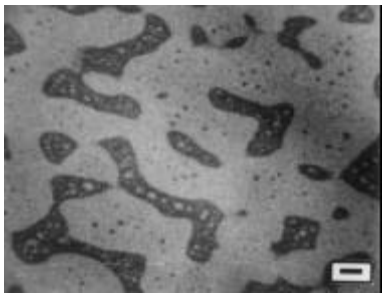

Figure 6-12. TEM image of RuO_4 stained thin sections of 25 wt % 15 K poly(arylene ether sulfone) modified cyanate ester network.[19]

An increase in temperature of cure increases the number of particles per unit volume and decreases the particle size for DGEBA/DDS/ETBN system. The reason for this is that the activation energy for viscosity was less than that for the polymerization. However, if the activation energy for viscosity is too small compared to that of polymerization reaction, the number average particle size increases with an increase in cure temperature to a certain temperature and then decreases. This is attributed to the presence of a bimodal particle size distribution.

This model was restricted by the initial rubber composition so that phase separation could occur only in a metastable region. It is possible that the initial rubber composition is close to the critical composition and the cure temperature is sufficiently high to speed up the polymerization reaction. When the molecular weight of the toughener is sufficiently high to tilt the phase diagram toward a lower composition of rubber, phase separation may occur through spinodal decomposition in the early stage and through a nucleation and growth mechanism in the late stage. Also, spinodal decomposition, generating a co-continuous structure in particles dispersed in a matrix that was generated by nucleation and growth mechanism, may occur. Combining the spinodal decomposition theory with the nucleation and growth mechanism may extend the applicability of this model to a high initial rubber composition or high molecular weight thermoplastic polymer.

6.6. REFERENCES

1. K. Yamanaka, Y. Takagi, T. Inoue, *Polymer*, **60**, 1839 (1989).
2. R. J. J. Williams, J. Borrajo, H. E. Adabbo, A. J. Rojas, In ***Rubber-Modified Thermoset Resins***; Riew, C. K.; Gillham, J. K., Eds.; Advances in Chemistry 208; American Chemical Society: Washington D.C., 1984; pp. 195-213.
3. P. J. Flory, "**Principles of Polymer Chemistry**", Cornell University Press, Ithaca, N.Y., 1953.
4. C. W. Macosco, D. R. Miller, *Macromolecules*, **9**, 199 (1976).
5. W. H. Stockmayer, *J. Chem. Phys.* **11**, 45 (1943).
6. D. Verchere, H. Sautereau, J. P. Pascault, S. M. Moschiar,C. C. Riccardi, R. J. J. Williams, *polymer*, **30**, 1156 (1989).
7. T. K. Sherwood, R. L. Pigford, C. R. Wilke, "**Mass Transfer**", McGraw-Hill, New York, **1975**, p. 215.
8. S. C. Kim, M. B. Ko, W. H. Jo, *Polymer*, **36**, 2189 (1995).
9. S. D. Lipshitz, C. W. Macosko, *Polym. Eng. Sci.*, **16**, 803 (1976).
10. A. Vazquez, A. J. Rojas, H. E. Adabbo, J. Borrajo, R. J. J. Williams, *polymer*, **28**, 1156 (1987).
11. J. Chen, Y. Lee, *Polymer*, **36**, 55 (1995).
12. D. Verchere, J. P. Pascault, H. Sautereau, S. M. Moschiar, C. C. Ricaardi, R. J. J. Williams, *Appl. Polym. Sci.* **43**, 293 (1991).
13. E. R. Weibel, Stereological Methods, vols. 1 and 2, Academic Press, New York, 1979.
14. L. M. Cruz-Orive, *J. Microscopy*, **112**, 153 (1978).
15. O. Kwon, T. C. Ward, *J. Comp. Theor. Polym. Sci.*, (1998), in press.
16. J. W. Cahn, *J. Chem. Phys.*, **42** (1), 93 (1965).
17. K. Yamanaka, T. Inoue, *Polymer*, **30**, 662 (1989).
18. K. Yamanaka, T. Inoue, *J. Mat. Sci.*, **25**, 241 (1990).
19. S. A. Srinivasan, Ph.D. Dissertation, Virginia Polytechnic Institute and State Unversity (1994).

Chapter 7: MORPHOLOGY AND FRACTURE TOUGHNESS

7.1. EXPERIMENTAL

7.1.1. Sample Preparation

The formulation was adjusted to provide 10 wt % rubber (ETBN) in the whole system (DGEBA/DDS/KELPOXY) and to keep a stoichiometric proportion of DDS with respect to the sum of epoxides coming from DER-331 and KELPOXY. The epoxy formulations are given in Table 7-1. A bulk mixture of KELPOXY and DER-331 was made by mechanical stirring in an oil bath at 90 °C with a nitrogen purge. A homogeneous solution was achieved in about 5 min and degassed to remove trapped air. DDS was added to the mixture and mechanically stirred at 130°C under vacuum until DDS dissolved completely. As explained in Chapter 6, the mixing time is crucial to obtaining the desired morphology. However, DDS did not dissolve so well in the DGEBA/ETBN mixture. In order to control morphology, the amount of DDS was reduced. The formulation is denoted as RENxxx where xxx denotes a temperature of precure.

For the fracture testing specimens, it took about 30 min for stoichiometric mixture with DDS to get a visibly clear solution of about 30g. The solution was poured into a preheated silicone rubber mold at 130 °C and degassed in a vacuum oven at this temperature at 29 in Hg until no air bubbles escaped. This process was repeated many times in order to obtain good test specimens for SES samples that were mixed in stoichiometric ratio and to obtain a homogeneous solution. Since REN samples contains less DDS than stoichiometric ratio, they did not take as long to mix homogeneously. The fractured samples were microtomed for SEM analysis.

Table 7-1. Epoxy formulations used in this investigation

System ID	DER-331 (g)	DDS (g)	KELPOXY (g)
NT-xxx	75.08	24.92	0
SESxxx	52.88	22.12	25.00
RENxxx*	56.67	18.33	25.00

* REN-xxx: DDS/EPOXY ratio was 0.8 in weight, the other two systems were mixed in stoichiometric ratio.

As soon as mixing and degassing were completed, samples were cured in a regulated convection oven at various temperatures until they passed the gel point. Some of the neat epoxy and SES samples were post-cured at 200 °C for 1 hour. The REN samples were postcured at 220 °C for 1 hr to get the maximum conversion of the epoxy-diamine matrix.

7.1.2. Fracture Toughness Measurements

The critical stress intensity factor (K_{IC}) and the critical strain energy release rate (G_{IC}), an indication of a material's ability to resist fracture, were measured for the rubber modified epoxy thermosets according to a procedure described by the American Society for Testing and Materials Specification (ASTM D 5045-91)[1]. Specimen samples were prepared by casting the degassed hot-melt resin into silicone rubber molds possessing dimensions of 3.25 mm x 6.5 mm x 38 mm. These samples were prepared for fracture toughness testing by notching samples (about 0.5 mm in depth) with a reciprocating saw. The geometry of this sample is given in Figure 7-1. The ASTM standard required that infinitesimally sharp cracks are needed for testing purposes, (the more blunt a crack is then the tougher the materials appears to be, hence leading to false toughness data). Sharp cracks were initiated within the specimen by first cooling a razor blade in liquid nitrogen, and tapping the sharp blade within the notch using an aluminum bar. Care was taken to ensure the crack had propagated evenly through the specimen thickness by holding the sample to the light and examining both edges.

7.1.3. Data Reduction for fracture toughness

Freshly cracked specimens were placed into the three point bend apparatus as shown in Figure which was attached to an Instron testing machine (Model 5035). The samples were tested at crosshead speed of 0.5 mm/min, 1 mm/min, 2 mm/min. Plane strain conditions must be attained, a specific requirement for testing materials with the specified dimensions using the ASTM D5045-91 standard. Upon failure, the various

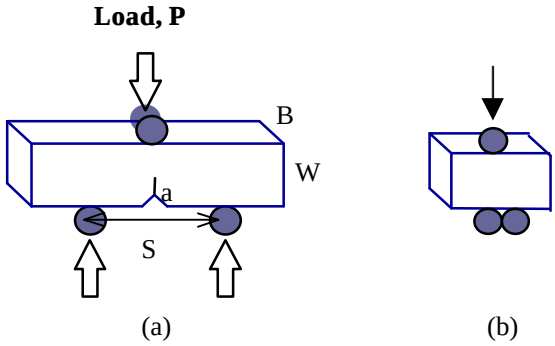

Figure 7-1. Schematic of (a) the three-point single-edge notched bending test and (b) correction of indentation.

specimen geometries such as crack length, width and thickness were measured using digital calipers. The critical stress intensity to cause catastrophic failure in mode I crack opening calculated using equation.

$$K_{IC} = \frac{PS}{BW^{\frac{3}{2}}} f(x) \qquad (7\text{-}1)$$

where $f(x) = \frac{3x^{\frac{1}{2}}\left[1.99 - x(1-x)(2.15 - 3.93x + 2.7x^2)\right]}{2(1+2x)(1-x)^{\frac{3}{2}}}$ and

P = Load at failure in N

B = Specimen thickness in mm

S = Span length between supports in mm

W = Specimen depth (width) in mm

X = a/W, where a is pre-crack length in mm

All calculated results were in MPa.m$^{1/2}$ and were reported with their standard deviations. Any data that contained crack length to width ratio, X, outside the 0.4 to 0.6 limits were not used in the data reduction procedure.

7.2. RESULTS AND DISCUSSION

7.2.1. Mixture Samples - Stoichiometric

The fracture toughness was measured using three-point single-edge notched bending specimens for neat epoxy and rubber modified epoxy thermosets cured under different conditions. These samples were all stoichiometric mixtures of amine to epoxy. The difficulties in dissolving DDS in the mixture of DGEBA/ETBN resulted in delay of their being at the designed cure so that the morphology could not be controlled. The curing temperatures and times employed were 130°C for 11 hours, 160 °C for 4 hours, and 200 °C for 1 hour. The morphological parameters are shown in Table 7-2. The results of the fracture toughness of those samples are presented in Figure 7-2.

Table 7-2. Morphological parameters for slow transferred samples SES

Transfer	Temp (°C)	R_N (μm)	R_V (μm)	V_f	S_V (μm)	λ (μm)	$N_V(10^6$ mm$^{-3})$
Slow	130	1.15	1.47	0.15	0.23	15.03	11.07
Slow	160	1.72	2.01	0.14	0.18	19.77	4.00
Slow	200	1.51	1.65	0.14	0.23	14.95	7.00

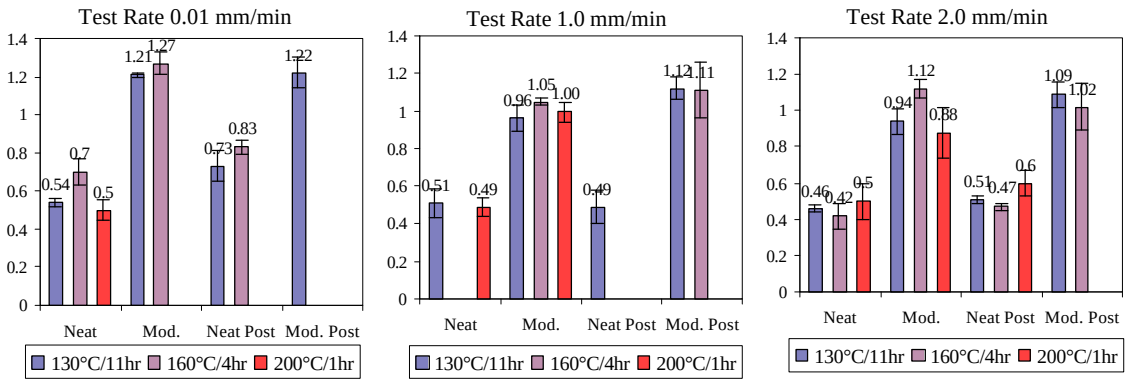

Figure 7-2. The critical stress intensity factors for neat and rubber modified epoxy cured at different conditions.

It is apparent that the rubber modified epoxies has about two fold higher critical stress intensity factor than the neat epoxy no matter what the cure conditions are. Postcure does not significantly change the fracture toughness. The cross-linking effects on the fracture toughness of DGEBA type epoxy monomer cured with DDS have been shown by Pearson and Lee[2]. They varied the molecular weight of the initial epoxy resin to change the cross-link density and found that the toughness of neat epoxy was independent of the cross link density. Therefore, it is not surprisng that postcure did not decrease the toughness of our samples significantly.

The rubber modified epoxy sample cured at 160 °C has the largest particles but the smallest number density and shows the highest toughness value. However, because all of the rubber modified epoxy samples have toughness values close to each other, it is not so easy to render a conclusion.

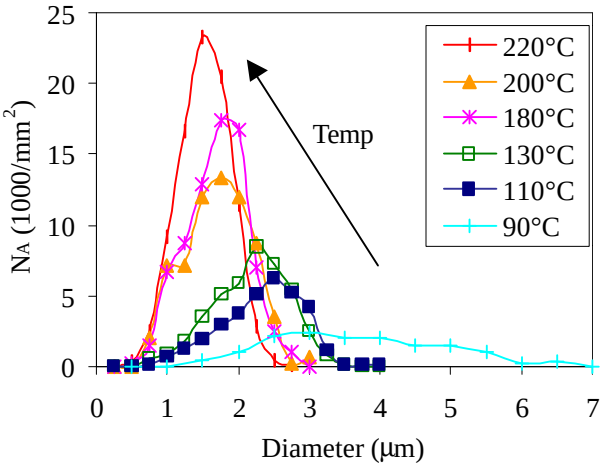

Figure 7-3. Two dimensional particle size distributions of REN samples.

7.2.2. Mixture Samples - Non-Stoichiometric

In an attempt to make more controlled morphology, the samples containing fewer amounts of DDS were prepared. Those samples were tested for the fracture toughness values. The results are presented in Figure 7-5. The morphology for those samples follows the behaviors as predicted in Chapter 6. The two-dimensional particle size distributions shown in Figure 7-3 is consistent with the predictions that were made in Chapter 6. The distributions are gradually narrower and the total number density of particles increases as temperature increases. The peak of distribution shifts to small radius as radius increases.

The influence of temperature on the morphological parameters is shown in Figure 7-5. The volume fraction of spheres remains constant independently of the temperature variation. Because of the constant volume fraction of spheres, the interspacing is inversely proportional to the surface fraction that was defined by the total surface area of all particles per unit volume of sample. The weight and number average radii decrease with an increase in the cure temperature while the number density increases. These same trends are predicted in Chapter 6. The maximum toughness was found to be at 200°C cure material in the temperature range employed as shown in Figure 7-5. In the temperature range, the values of toughness show definite improvement for rubber modified epoxy materials relative to the neat epoxy.

Although the temperature variation can change the morphology of rubber toughened thermosets, the toughness does not seem to be significantly varied by the cure temperatures employed. This is because one morphological parameter changes in the direction of improving the fracture toughness while the other parameter changes in the opposite direction. Since the average radius and the number density are independent variables and others parameters such as volume fraction, surface area fraction, and

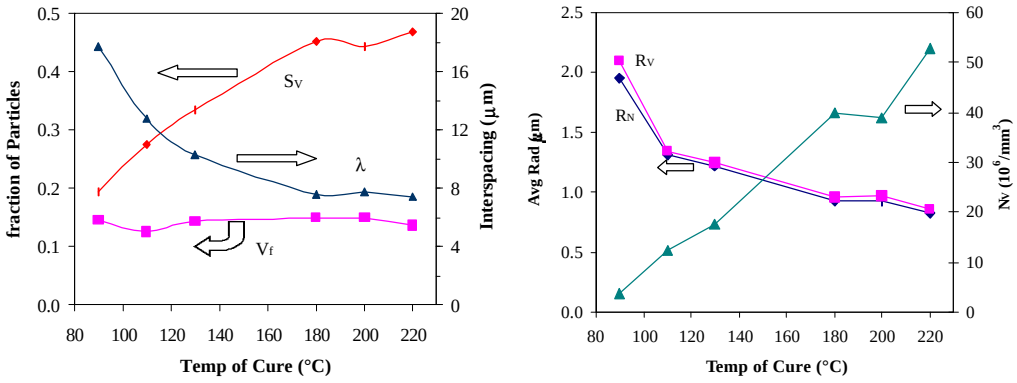

Figure 7-4. The influence of cure temperature on morphological parameters for REN samples.

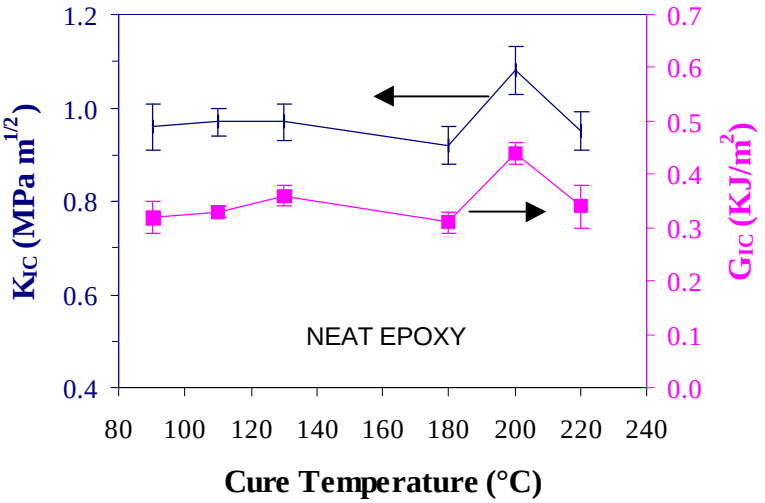

Figure 7-5. The effect of cure temperature on fracture toughness. Test rate was 1.0 mm/min.

interspacing distance are dependent variables, the toughness values were normalized with radius and number density, respectively.

A plot of the value normalized with respect to radius as a function of the number density will show the effects of number density on the fracture toughness per unit size of particle. This is shown in Figure 7-6 (a). Similarly, the toughness normalized with respect to the number density will show the influence of the particle size on the fracture toughness per unit number of particles. As shown in Figure 7-6, the fracture toughness per unit size is proportional to the number density, and is dependent on the radius of particles to the third power.

7.3. CONCLUSIONS

The effects of morphology on fracture toughness have been investigated. The fracture toughness values in terms of K_{IC} and G_{IC} were measured for rubber toughened epoxy thermosets material. The initial volume fraction rubber was kept constant for all of the test specimens, and the cure temperature was varied to induce a resulting morphology. This constant initial rubber composition excludes a variable to affect the fracture toughness of the material. The morphology generated by variations of cure temperature would affect the fracture toughness. However, our study did not show apparent improvement of fracture toughness by temperature variation even if a different morphology is generated.

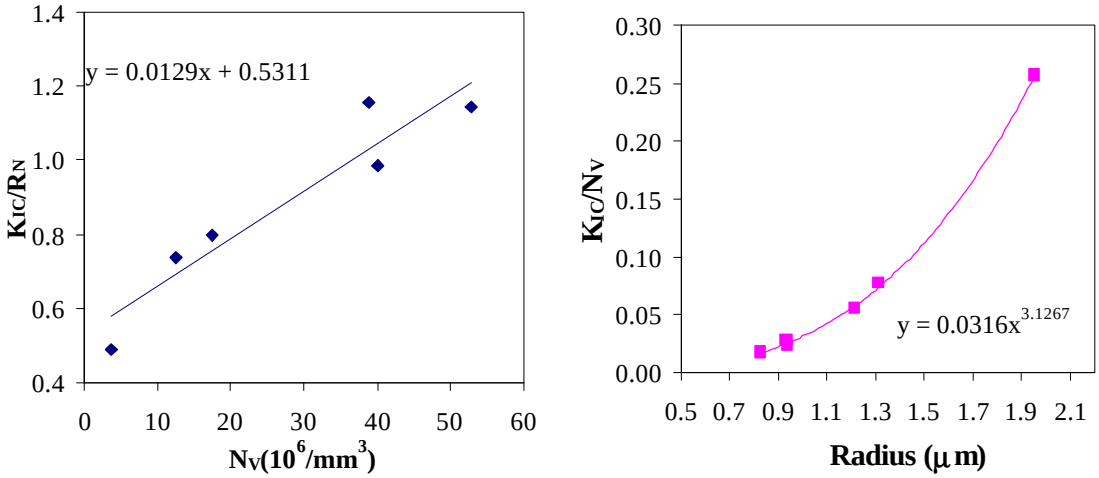

Figure 7-6. Normalized fracture toughness with respect to radius shows linear dependence on number density (a) and normalized fracture toughness with respect to number density shows third power dependence on the radius.

There are two or more parameters, of which one may act in reducing the fracture toughness and the other may act in improving the fracture toughness. Those effects were analyzed in terms of size and number density of particles.

7.4. REFERENCES

1. *Annual Book of ASTM Standards*, D5045-91, (1991).
2. R. A. Pearson, A. F. Yee, *J. Mat. Sci.*, **24**, 2571 (1989).

Chapter 8: CONCLUSIONS

Phase separation process induced by the polymerization has been investigated to obtain better knowledge to control the morphology of binary polymeric material and to establish the relationship between the morphology and fracture toughness. The material selected to perform these missions were epoxy thermosets modified with rubber. Epoxy thermosets exhibit outstanding mechanical and thermal properties except for their brittleness. Incorporation of rubber into the epoxy matrix has provided great enhancement of the fracture toughness of thermosetting materials. However, although many postulations have been suggested for explaining how the toughening occurs, no theory has been confirmed. The reasons for this are not only the limited understanding of the phase separation process that occurs during polymerization, but improper experimental methods that are used to investigate the toughening mechanism.

In Chapter 2, we developed a quantitative technique to construct a three dimensional particle size distribution from a two dimensional distribution that is usually observed in microscopy. Testing conversion methods with known polydisperse sphere systems revealed that the use of a circle size distribution as an approximation or substitute for the sphere size distribution might sometimes cause unacceptable errors. The method established by Scheil was found to be incorrect for a recursive formula in a coefficient matrix.

A model which can describe phase separation process during polymerization reaction has been developed on the basis of thermodynamics of a binary mixture combined with nucleation and growth rates. This model was applied to a rubber modified epoxy thermoset. The morphological changes of this reaction system as a function of conversion were analyzed in the framework of the modified model. It was shown that the model accurately describes the final morphologies of rubber particles dispersed in epoxy matrix when phase separation takes place in a binodal region. For a system that falls into a spinodal region, the computation technique can be modified by adopting Chan and Hilliard treatments.

Therefore, this model was restricted by the initial rubber composition so that phase separation could occur only in a metastable region. We often encounter that the initial rubber composition is close to the critical composition and the cure temperature is sufficiently high to speed up the polymerization reaction. In this case, the phase separation may occur through spinodal decomposition. It is demonstrated for a system to phase separate by nucleation and growth in an early stage followed by the spinodal decomposition in a later stage or vice versa. Those cases were explained qualitatively. Combining the spinodal decomposition theory with the nucleation and growth mechanism may extend the applicability of this model to a high initial rubber composition close to the critical composition.

This model also neglected the possibility of the coalescence. A statistical treatment can be used for setting the positions of nuclei in a three dimensional space. It can be assumed that when particles collide to form a new larger particle, the new particle is located in the center of the colliding particles. The radius of the new particle can be calculated from the total volume of the colliding particles. Therefore, the assumption of neglecting the coalescence process can be avoided. Another idea is to redistribute in a given space all of the polydisperse particles generated during the separation process. In the redistribution process, one might count number of particles which collide, subtract the number of collision from the original number of particles and increase the size of particles.

The cure reaction was analyzed based upon the autocatalytic reaction kinetic expression. When epoxy resins are cured with diamine curing agents, the hydroxyl groups produced by epoxide ring opening reaction catalyze the other ring opening reaction. Using the kinetic parameters determined from the residual heat measurements, the TTT diagrams were constructed based on the Macosko equation for vitrification and the Flory-Stockmayer equation for gelation. This diagram covers broad range of time that cannot, in practice, be obtained from normal experiments. The gel points and vitrification points measured with DMTA verify the validity of the constructed TTT diagram.

In the last chapter, the measured fracture toughness value was analyzed in terms of morphology that were generated by the variation of cure temperature. However, our study did not show apparent improvement of fracture toughness by temperature variation even if different morphology is generated. There are two or more parameters, of which one may act to reduce the fracture toughness and the other may act to improve the fracture toughness. Those effects were analyzed in terms of size and number density of particles.

This work can be applied to thermoplastic modified thermoset systems. If we adopt an equation of state theory for creating the surface of the free energy, it can be further extended to cover a system that shows the LCST behavior or both LCST and UCST behaviors.

Vita

Ojin Kwon was born June 23, 1963 in Seoul, Korea. He graduated from Seoul National University with a bachelor degree of chemical technology in Engineering School in February 1986. He entered University of Texas at Arlington in the fall of the same year where he received a Master of Science studying quantum chemistry in chemistry in 1991. After he spent two years in Korea, he joined Dr. Ward research group in chemistry department at Virginia Tech in 1993.